Università degli Studi dell'Insubria

Dipartimento di Scienza e Alta Tecnologia - Como

MUonE: A HIGH-ENERGY SCATTERING EXPERIMENT TO STUDY THE MUON $g - 2$

MASTER DEGREE IN PHYSICS

Tutor

Prof. Michela Prest
Università degli Studi dell'Insubria

Author

Mattia Soldani

Cotutors

Dr. Erik Vallazza
INFN Sezione di Milano-Bicocca

Prof. Clara Matteuzzi
INFN Sezione di Milano-Bicocca

Como, March 2019

It's super effective!

To my 134 parts per million...

Contents

Riassunto

All'inizio del XXI secolo, la fisica delle particelle sembra trovarsi sull'orlo di un profondo mutamento: l'incongruenza tra alcuni risultati sperimentali e le rispettive predizioni teoriche potrebbe indicare che il Modello Standard, la teoria che descrive con maggiore dettaglio le componenti fondamentali della Natura e le loro interazioni, è incompleto. In particolare, il Modello Standard sembra essere inadeguato alla caratterizzazione delle cosiddette anomalie magnetiche, o $g-2$, le costanti di proporzionalità tra il momento magnetico e lo spin delle particelle fondamentali.
Grazie all'alta sensibilità alle interazioni elettromagnetica, forte e debole e all'ottima precisione con cui può essere misurata (oggi inferiore alla parte per milione), l'anomalia del muone costituisce un potente strumento di indagine per studiare i limiti dei modelli teorici. In particolare, il $g-2$ del muone potrebbe celare un indizio dell'esistenza di Nuova Fisica oltre il Modello Standard: il risultato ottenuto dall'esperimento E821 (Brookhaven National Lab, 1999-2001), ad oggi la più recente e precisa misura dell'anomalia, dista 3.6σ dall'attuale previsione teorica.
Tra i numerosi processi che contribuiscono all'interazione tra il muone e il campo elettromagnetico e, di conseguenza, che definiscono il valore totale dell'anomalia, la polarizzazione del vuoto a singolo loop (leading-order) adronico costituisce la principale fonte di incertezza sul valore teorico di $g-2$. Poiché nella cromodinamica quantistica, la teoria delle interazioni adroniche, l'approccio perturbativo è impraticabile nel regime di bassa energia, lo studio di questo contributo deve essere condotto a partire dai risultati sperimentali – tipicamente dalle misure della sezione d'urto dell'annichilazione e^+e^- negli stati adronici. Un approccio innovativo consiste nello sfruttare il running della costante di struttura fine, che può essere estratto dalla sezione d'urto dello scattering elastico di muoni ad alta energia su elettroni atomici; poiché quest'ultima è liscia e priva di risonanze, tale approccio consente una riduzione consistente dell'incertezza associata al risultato ottenuto nel modo tradizionale.
La collaborazione MUonE propone di studiare lo scattering elastico $\mu^\pm e^-$ con un esperimento a bersaglio fisso sulla linea di fascio di muoni ad alta energia ($\gtrsim 150$ GeV) e alta intensità M2 del CERN in una sessione di 1 o 2 anni durante il Run 3 (2021-2024). L'obiettivo dell'esperimento è la misura del contributo leading-order adronico con una incertezza di circa 0.3%. I risultati di MUonE,

insieme a quelli delle misure dirette dell'anomalia che verranno condotte con altissima precisione (0.1 ppm) dagli esperimenti E989 (Fermilab) e E34 (J-PARC), potrebbero confermare la presenza della discrepanza tra la previsione del Modello Standard e i valori sperimentali con una significatività statistica superiore a 5σ.

Nel 2018 è stato condotto un test di fattibilità di 8 mesi per studiare le potenzialità e i limiti del concept di MUonE. Il cuore del setup è costituito da 16 sensori a microstrip di silicio a singola faccia, con un'area attiva di circa 10×10 cm^2 e una risoluzione intrinseca di circa 35 µm, organizzati in tre stazioni, lunghe circa 50 cm, per il tracciamento in ingresso e in uscita da due targhette di grafite spesse 8 mm. Dopo 3 mesi di presa dati, la seconda targhetta è stata rimossa per studiare la variazione della risposta del sistema all'incremento del braccio di leva di uscita, portato a circa 1.2 m. Un sensore stereo (con le strip orientate a 45° rispetto agli assi trasversali di riferimento) è stato installato in ognuna delle stazioni per la risoluzione delle tracce multiple. Un calorimetro a cristalli scintillanti (di $PbWO_4$ nella prima fase della presa dati, di BGO in seguito) con una sezione trasversale di circa 10×10 cm^2 consente di misurare l'energia dell'elettrone emesso.

Per sfruttare appieno l'alta risoluzione spaziale dei rivelatori a microstrip, considerevolmente inferiore rispetto alla precisione con cui questi sono stati posizionati nell'area sperimentale, è stato sviluppato un algoritmo iterativo di allineamento offline, che corregge gli shift e i tilt relativi dei piani traccianti. Inoltre, tale algoritmo è uno strumento versatile e potente per l'identificazione di malfunzionamenti locali dei rivelatori.

Nel corso del test di fattibilità è stata raccolta una statistica di più di 550 milioni di eventi di singola traccia in ingresso. Una selezione basata sulla topologia di uscita dell'evento, sull'identificazione $\mu - e$ (effettuata sfruttando la differenza nel momento di uscita e, di conseguenza, nel contributo dello Scattering Multiplo Coulombiano), sulla qualità delle tracce e su una prima fase di eliminazione del background (costituito principalmente da coppie e^+e^- e da raggi δ) ha permesso l'identificazione di 74153 eventi candidati allo scattering elastico (134 ppm) e la caratterizzazione dello spazio delle fasi definito dagli angoli di scattering θ_e e θ_μ e dall'energia finale dell'elettrone E_e^{f}; in particolare, sono state osservate le curve cinematiche $\theta_\mu(\theta_e)$ e $E_e^{\mathrm{f}}(\theta_e)$ previste dalla relatività speciale.

I risultati del run del 2018 indicano che il setup sperimentale utilizzato è adatto allo studio dello scattering elastico $\mu^\pm e^-$. Ciononondimeno, il test di fattibilità ha portato alla luce la necessità di alcuni miglioramenti. Particolare attenzione deve essere posta nella struttura longitudinale del sistema di tracciamento: la distanza tra la targhetta e il primo piano di silicio a valle della targhetta stessa deve essere abbastanza grande da garantire una buona accettanza a piccoli angoli di scattering; d'altra parte, le dimensioni limitate dell'area sperimentale rendono necessario un trade-off tra la compattezza del setup e il potere di risoluzione di doppia traccia.

I sensori stereo si sono rivelati superflui: sebbene utili per la risoluzione di mul-

tiple tracce, la loro orientazione limita l'accettanza complessiva del sistema di tracciamento, con conseguente perdita di statistica. Inoltre la risoluzione di doppia traccia può essere effettuata dall'algoritmo di tracciamento in uscita.
Il calorimetro è risultato fondamentale per l'eliminazione del background: gli eventi non elastici a basso θ_μ, principale fonte di rumore nella regione elastica dello spazio delle fasi, possono essere esclusi tramite una selezione sull'energia dell'elettrone in uscita. Tale selezione può essere effettuata soltanto sul sottoinsieme degli eventi che si trovano entro l'accettanza del calorimetro, perciò è necessario utilizzare un calorimetro dalla sezione trasversa sufficientemente estesa.
Il perfezionamento delle condizioni di selezione dei candidati allo scattering elastico e degli algoritmi di eliminazione del background costituisce il prossimo obiettivo dell'analisi dei dati raccolti durante il run del 2018. Queste migliorie procedono di pari passo con lo sviluppo dei metodi teorici e analitici indispensabili per la determinazione della sezione d'urto dello scattering elastico $\mu^\pm e^-$ dai dati che saranno raccolti a partire dal 2021. Nel frattempo, i dati del 2018 potrebbero fornire una valutazione preliminare del contributo del leading-order adronico al $g-2$.

Introduction

Nowadays, particle physics might be on the verge of a revolution: recent experiments claim the inconsistency between their observations and the predictions of the Standard Model, the most exhaustive theory of the Nature fundamental components and of the way they interact. In particular, the Standard Model might be inadequate in describing the so-called magnetic anomaly, or $g-2$, of the fundamental particles, that is, the proportionality constant that relates their spin and magnetic moment.
Being highly sensitive to the electromagnetic, strong and weak interactions and experimentally measurable with high precision (nowadays below the part per million), the muon anomaly has proven to be an excellent test bench in many occasions. Its importance in solving the particle physics puzzles dates back to its early investigations at CERN (1958-1976), whose focus was on the muon itself and on the riddle of its large mass, which made it appear more similar to the hadrons than to the electron, and of its long lifetime, which could not be explained by means of the strong interaction.

> *"Who ordered that?"*
>
> Isidor Isaac Rabi on the discovery of the muon, 1936

Since then, the muon anomaly has played an important role in studying all the particles within the realm of the Standard Model. Nowadays it might forge the path to New Physics: indeed, a 3.6σ discrepancy between the E821 measurement (Brookhaven National Labs, 1999-2001) and the theoretical prediction has been reported.
Among the several processes that participate in the electromagnetic interaction of the muon and hence contribute to the overall muon anomaly value, the hadronic single-loop vacuum polarization (Hadronic Leading-Order) represents the main source of uncertainty on the theoretical prediction of the $g-2$. Given the fact that in quantum chromodynamics, the theory of the hadronic interactions, the perturbative approach in the low-energy range is infeasible, the evaluation of this contribution can only be performed by turning to experimental results: the traditional method is based on the measurement of the cross section for e^+e^- annihilation into hadrons, while a novel approach exploits the running of the fine-structure constant, which can be extracted from the cross section of the elastic scattering of high-energy muons on atomic electrons.

The MUonE collaboration proposes to study the kinematics of such a scattering process with a fixed-target experiment, whose core is a silicon-based tracking system, exploiting the high-energy, high-intensity muons of the CERN M2 beamline; its 1- or 2-year long run is expected to take place during the CERN Run 3 (2021-2024). An uncertainty of $\sim 0.3\%$ on the resulting HLO contribution has been estimated. Such a result, together with the direct measurements of the muon anomaly that will be performed with unprecedented precision by the E989 (Fermilab) and E34 (J-PARC) experiments, might push the overall value of the discrepancy above the 5σ level.
Such a wind of renewal drives this thesis work. In the first chapter, the theoretical and experimental frameworks of the muon anomaly are summarized and their results are compared, thus showing their inconsistency. This chapter presents the current status of the investigation and gives an outlook on the future experiments.
In 2018, a ~ 7.5 month long feasibility test was performed, exploiting the detectors of the INSULAb group, in order to investigate the potential and the limitations of the MUonE concept in studying the $\mu^{\pm}e^{-}$ elastic scattering; the experimental conditions and the setup of this test are presented in the second chapter.
The third chapter summarizes the collected statistics and describes the data conditioning steps that are needed to reconstruct the scattering kinematics and to keep the accuracy on the physical observables under control. In particular, a software for the offline, high-precision relative alignment of the tracking detectors has been developed: its features and performance are discussed in this chapter.
The input beam characterization and the elastic scattering kinematics analysis are presented in the fourth chapter, with particular attention on the elastic candidate selection criteria, the resulting dataset statistics, the comparison between the measured kinematics and the theoretical predictions, the background rejection methods and the acceptance limits they introduce.

CHAPTER 1

The muon magnetic anomaly

From the very beginning of particle physics, the magnetic anomaly of the subatomic particles has proven to be a convenient probe for investigations. The inadequacy of the classical description of matter, the quantum nature of the fundamental forces and the inner structures of the hadronic states could be verified by means of their effect on the value of the anomaly. Such a value has been predicted by more and more exhaustive theories and, at the same time, has been measured by more and more precise experiments.
Nowadays, both the Standard Model predictions and the experimental results have reached astonishingly low uncertainties: this makes the magnetic anomaly useful for theory verification. In particular, the electron anomaly provides a test of the Quantum ElectroDynamics (QED) on the scale below 1 ppb [1]. On the other hand, the muon anomaly might prove to be a gate to New Physics: indeed a $\sim 3.6\sigma$ discrepancy between the SM prediction and the measurements [2] has been found and is currently under study. This chapter provides a summary of the main steps in the muon anomaly history and an overview of the present status of the investigation.

1.1 The anomaly in the Dirac model

The orbit of an electrically charged body in motion in a magnetic field $\overline{B}$ experiences a torque

$$\overline{\tau} = \overline{\mu} \times \overline{B} \tag{1.1}$$

where $\overline{\mu}$ is called magnetic moment and contains information on all the features of the body and of the orbit [3]. If the motion has an angular momentum

$\overline{L} = \overline{r} \times \overline{p}$, $\overline{r}$ and $\overline{p}$ being the position and the momentum respectively, then the magnetic moment is

$$\overline{\mu}_L = \frac{e}{2mc}\overline{L} \tag{1.2}$$

where e is the body total charge and m is its total mass [4]. Besides the orbital motion, such a body can be spinning; this rotation can be described by means of an intrinsic angular momentum $\overline{S}$ and generates a magnetic moment

$$\overline{\mu}_S = g\frac{e}{2mc}\overline{S} \tag{1.3}$$

which shows a dimensionless factor g, the so-called gyromagnetic factor or g-factor, absent in the orbital component described by equation 1.2 [4].
For a classical spinning system, in which the charge and mass are governed by the same spatial distribution functions, $g = 1$ [5]. Nevertheless, the subatomic world cannot be exhaustively described without turning to quantum mechanics; the evaluation of the g-factor of the subatomic particles is then a way to quantify the deviation of their interaction with a magnetic field from the one suggested by classical reasoning [5].
Dirac's theory describes a relativistic spin-½ charged particle with a bispinor ψ and its motion in an electromagnetic field with the minimally-coupled Dirac equation

$$\left[\gamma^\mu \left(p_\mu - eA_\mu\right)\right]\psi = 0 \tag{1.4}$$

where p_μ is the particle 4-momentum, A_μ is the electromagnetic 4-potential and γ^μ are the four gamma matrices [6]. Taking the low-energy limit of equation 1.4 leads to

$$i\hbar\frac{\partial\varphi}{\partial t} = \left[\frac{p^2}{2m} - \frac{e}{2mc}\left(\overline{L} + 2\overline{S}\right)\cdot\overline{B}\right]\varphi \tag{1.5}$$

for the Pauli spinor φ which models a nonrelativistic spin-½ charged particle [5, 6]. Indeed this is the equation that Pauli formulated in 1927 with phenomenological reasoning for spin-½ particles, but it has been obtained with a merely theoretical approach; details on this derivation can be found in [5, 6].
The second term on the right side of equation 1.5 shows that for Dirac particles $g = 2$ [6]. Although this result has been obtained starting from Dirac's equation, it is not a prerogative of special relativity: it can be shown that equation 1.5 can be derived theoretically by linearizing the Schrödinger equation; therefore $g = 2$ is not a relativistic effect, but instead a property of the waves, and thus of the particle wave functions [7].
The Dirac particle is point-like, i.e. Dirac's theory does not take into account the possibility for the particle to have an internal structure, and only couples with the electromagnetic field [6, 8]. This means that if the particle participates in any other interaction which gives it an internal structure then such a departure from the Dirac description might be reflected in the g-factor value; for example, this is the case of the proton, for which $g \sim 5.586 \neq 2$ [8].

However, early measurements performed in the field of atomic physics showed that $g \sim 2.002 \neq 2$ for the electron as well [9]. This is symptomatic of the fact that, even in absence of an internal structure, the quantum nature of the electromagnetic interaction itself affects the value of the g-factor [8].

1.2 Self-interaction and the QED predictions

In QED the g-factor typically enters the calculations in the form $(g-2)/2$; it is therefore common practice to refer to the so-called magnetic anomaly

$$a = \frac{g-2}{2} \tag{1.6}$$

instead of referring to g directly [5]. For Dirac particles $a = 0$, which follows trivially from the results of section 1.1.
QED treats $a \neq 0$ by correcting it for self-interaction processes, i.e. quantum fluctuations associated with the emission and absorption of virtual photons in the particle-field interaction region and the polarization of the vacuum by these photons into virtual particle-antiparticle pairs [5, 8].
Figure 1.1 shows the Feynman diagrams representing such self-interaction processes down to the second lowest-order [5]. The process depicted in figure 1.1a represents the largest contribution of the QED to the Dirac prediction of the anomaly; early calculations performed in 1948 on this process resulted in

$$a^{\mathrm{QED}} = \frac{\alpha_0}{2\pi} = 0.001162 \tag{1.7}$$

where $\alpha_0 = e^2/\hbar c$ is the fine structure (or Sommerfeld's) constant [8, 9]. This corresponds to $g = 2.002324$, which is in good agreement with the experimental results available at the time of the calculation for the electron [9].
QED calculations down to the fourth lowest-order performed in the Seventies using $\alpha_0^{-1} = 137.035987(29)$ led to the results

$$a_e^{\mathrm{QED}} = 115965240(40) \times 10^{-11} \tag{1.8}$$

and

$$a_\mu^{\mathrm{QED}} = 116585170(230) \times 10^{-11} \tag{1.9}$$

for the electron and the muon respectively [5]. In order to understand why these two values differ so heavily, some considerations on the nature of the self-interaction processes have to be made.
Nowadays the existence of the τ, i.e. a third, heavier and shorter-living lepton, is well known. Investigations on its magnetic anomaly are being performed as well, despite the severe limitations that are pointed out in subsection 1.4.1.

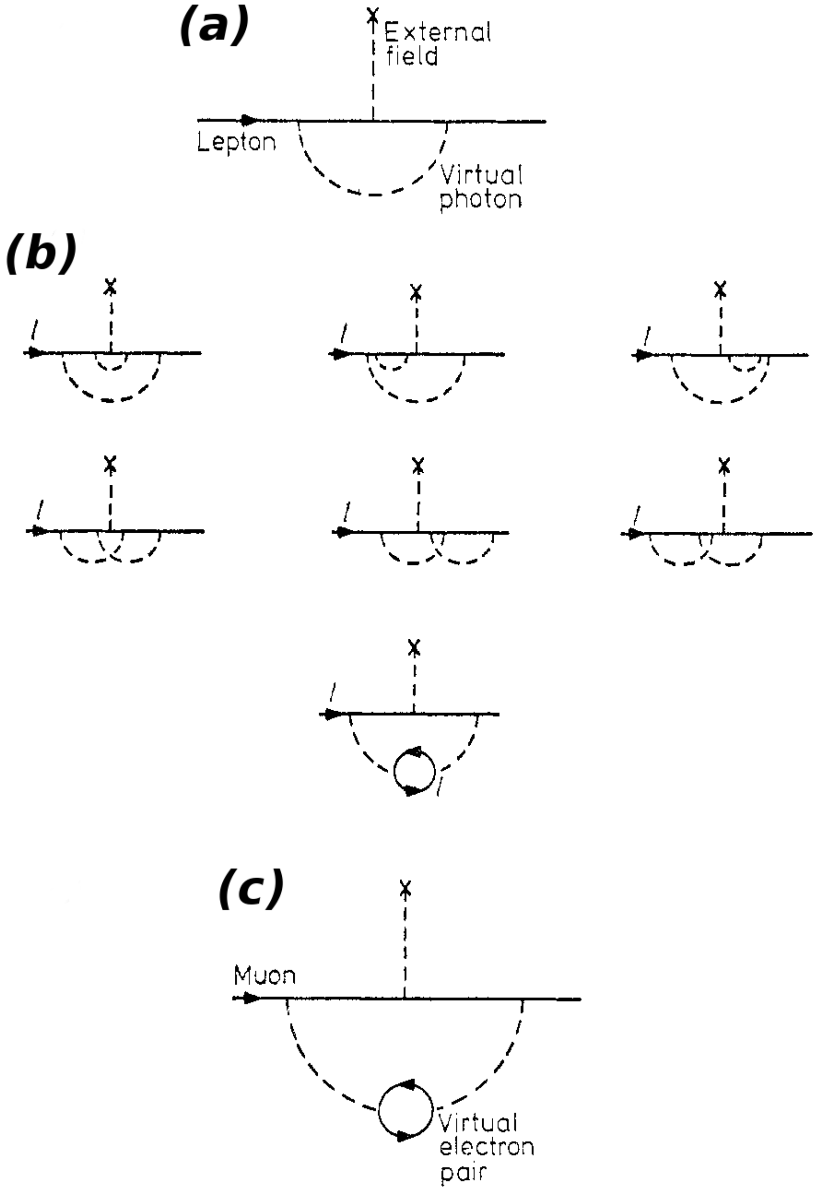

FIGURE 1.1. QED self-interaction processes down to the second lowest-order [5]: *(a)* the lowest-order process, related to A_1 (equation 1.10); *(b)* the second lowest-order processes without multiple lepton flavours, related to A_2; *(c)* example of second lowest-order process with multiple lepton flavours, related to B_2.

	mass [MeV/c^2]	lifetime [s]
electron	0.5109989461(31)	stable
muon	105.6583745(24)	$2.1969811(22) \times 10^{-6}$
$\boldsymbol{\tau}$	1776.86(12)	$290.3(5) \times 10^{-15}$

Table 1.1. Lepton masses and lifetimes [2].

1.2.1 Electrons and muons

Table 1.1 shows the mass and lifetime values for the three leptons. Important differences between the electron and the muon emerge: the latter has ~ 207 times the mass of the former. This affects the weights the higher-order self-interaction processes have in the corrections to the different lepton cases [5].
Processes of the n-th order contribute to a with terms that are proportional to $(\alpha_0/\pi)^n$ [5]. It is convenient to write down the resulting power series as [5]

$$a^{\mathrm{QED}} = \sum_{n=1}^{\infty} A_n \left(\frac{\alpha_0}{\pi}\right)^n + \sum_{n=2}^{\infty} B_n \left(\frac{\alpha_0}{\pi}\right)^n \tag{1.10}$$

in which:

- the first sum includes contributions from all the diagrams in which there are only photons or in which vacuum polarization involves the same lepton flavour as that of the particle which undergoes the interaction – see for example figures 1.1a and 1.1b;
- the second sum, starting with $n = 2$, includes contributions from all the vacuum polarization processes in which the leptons of the loops differ from the primary one – see for example figure 1.1c.

As already pointed out in equation 1.7, A_1 has been calculated analytically with the result $A_1 = 1/2$. All the A_n are independent of the lepton mass and so are the same for both the electron and the muon [5]. On the other hand, the B_n differ between the different leptons due to their dependence on the particle mass: with its ~ 106 MeV/c^2 mass the muon quite readily causes vacuum polarization into electron-positron pairs while the effect that polarization into muons-antimuons has on the electron anomaly is negligible [5].
Obviously, this classification of the self-interaction processes, which has the merit of highlighting the reason why the results for a_e^{QED} and a_μ^{QED} differ, is arbitrary: finer choices that split contributions from all the three different leptons can be

found in [10–12]. For the muon anomaly, the status of the calculations is

$$\begin{aligned} a_\mu^{\text{QED}} = 0.5 \left(\frac{\alpha_0}{\pi}\right) + \\ + 0.765857425(17) \left(\frac{\alpha_0}{\pi}\right)^2 + \\ + 24.05050996(32) \left(\frac{\alpha_0}{\pi}\right)^3 + \\ + 130.8796(63) \left(\frac{\alpha_0}{\pi}\right)^4 + \\ + 753.3(1.0) \left(\frac{\alpha_0}{\pi}\right)^5 \end{aligned} \tag{1.11}$$

for the five lowest-order terms; the resulting total value for the QED contributions is

$$a_\mu^{\text{QED}} = 116584718.95(0.08) \times 10^{-11} \tag{1.12}$$

in which $\alpha_0^{-1} = 137.035999049(90)$ has been used and whose small error results mainly from the uncertainty on α_0 [2].

1.3 The anomaly in the Standard Model

The Standard Model predicts that leptons interact not only by means of the electromagnetic force, but also by means of the strong and weak forces [10]. The electron anomaly is rather insensitive to strong and weak interactions, so it represents a useful tool for QED precision testing [10]. On the other hand, the muon anomaly allows to test the entire SM, since all its three sectors contribute in a significant way to the total theoretical prediction of a_μ^{SM} [10].

1.3.1 a_e^{SM} and the glory of the QED

Thanks to the excellent precision achieved on the experimental determination of the electron anomaly, i.e. 0.22 ppb [2], its theoretical predictions can be exploited for one of the most precise determinations of the fine-structure constant α_0 [12]. Typical SM calculations of a_e^{SM} include the predominant QED term, evaluated up to the fifth lowest-order in α_0/π, and the very small corrections for the electroweak and hadronic interactions, independent on α_0 [12].
Forcing the equation $a_e^{\text{SM}}(\alpha_0) = a_e^{\text{exp}}$ it is possible to solve for α_0; this leads to the remarkable result $\alpha_0^{-1} = 137.035999084(51)$ which essentially represents a test for QED on the scale of 0.37 ppb [1]. A recent study in the field of atomic physics performed an independent α_0 measurement with 0.20 ppb precision: albeit even more precise, its result is fully compatible to the latest one obtained from the electron anomaly [13]. Such a large set of precise results, from both the experimental and the theoretical front, can possibly pave the way for future studies on any possible electron internal structure [12].

1.3.2 a_μ^{SM} as the SM test bench

In general, departures from a merely electromagnetic scattering theory affect the magnetic anomalies with the contribution

$$\frac{\Delta a_l}{a_l} \propto \pm \left(\frac{m_l}{m_{\mathrm{scale}}} \right)^2 \tag{1.13}$$

where $l = e,\ \mu,\ \tau$ is the lepton flavour and m_l its mass; equation 1.13 shows that the muon anomaly is much more sensitive than the electron one to departures from pure QED [8].
Indeed, as already stated, electroweak and hadronic contributions to a_μ^{SM} are non-negligible [10]. The SM prediction is

$$a_\mu^{\mathrm{SM}} = 116591803(49) \times 10^{-11} \tag{1.14}$$

where the error is the combination in quadrature of the QED, electroweak, hadronic leading-order and higher-order hadronic components [2].
Since the QED description of the vacuum polarization processes is very accurate, their contribution to the total error is only 0.08×10^{-11}, as already shown in equation 1.12. In order to understand why the other SM components contribute in such a predominant way to the total error, the electroweak and hadronic processes involved in the corrections to a_μ^{SM} must be examined. It is convenient to write

$$a_\mu^{\mathrm{SM}} = a_\mu^{\mathrm{QED}} + a_\mu^{\mathrm{EW}} + a_\mu^{\mathrm{HLO}} + a_\mu^{\mathrm{HNLO}} \tag{1.15}$$

where the first term corresponds to the one already shown in equation 1.12.

1.3.2.1 The electroweak term

The term a_μ^{EW} of equation 1.15 groups all the loop contributions that involve $W^\pm$, Z, Higgs bosons and neutrinos. These processes are suppressed by at least a factor $(\alpha_0 m_\mu/\pi M_W)^2 \sim 4 \times 10^{-9}$ with respect to the QED effects [2].

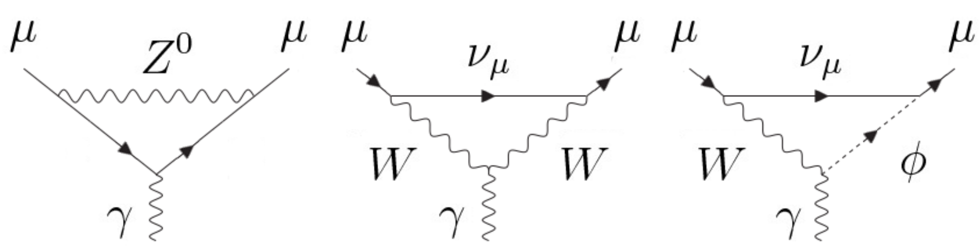

FIGURE 1.2. Main electroweak lowest-order self-interaction processes; here ϕ represents a Goldstone boson. Edited from [10].

The lowest-order processes are depicted in figure 1.2. Their contribution is

$$a_\mu^{\mathrm{EW}}[\text{1-loop}] = 194.8 \times 10^{-11} \tag{1.16}$$

which has been calculated analytically; details on this calculation can be found in [2].
The correction given by two-loop processes is relatively large and has opposite sign with respect to a_μ^{EW}[1-loop]; it is

$$a_\mu^{\mathrm{EW}}[\text{2-loop}] = -41.2(1.0) \times 10^{-11} \tag{1.17}$$

and its error, which is mainly given by hadronic loops like the ones depicted in figure 1.3, represents the electroweak contribution to the total error of equation 1.14 [2]. Three-loop corrections, whose contributions are extremely small, are under study [2, 10].
Adding equations 1.16 and 1.17 results in

$$a_\mu^{\mathrm{EW}} = 153.6(1.0) \times 10^{-11} \tag{1.18}$$

for the second term of equation 1.15 [2].

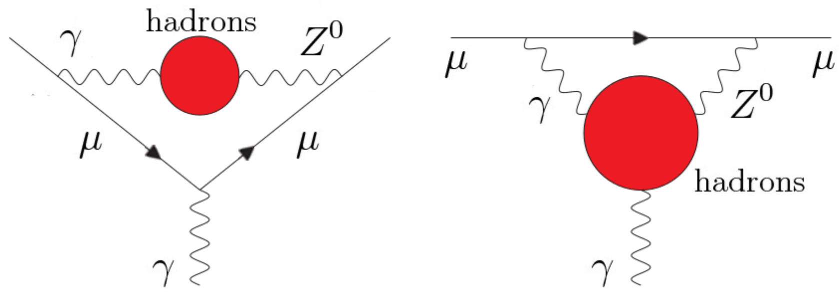

FIGURE 1.3. Hadronic loops in electroweak two-loop self-interaction processes: (left) hadronic photon-Z mixing; (right) quark triangle loops. Edited from [10].

1.3.2.2 The HLO term

Equation 1.14 shows that most of the a_μ^{SM} uncertainty comes from self-interaction processes with hadronic loops, since the contributions of these effects cannot be computed from first principles [2, 14]. In particular, the predominant correction comes from the hadronic leading-order contribution, i.e. the lowest-order hadronic loop vacuum polarization process, whose diagram is shown in figure 1.4. The evaluation of this term using the present theory is problematic since it involves long-distance interactions for which perturbative Quantum Chromo-Dynamics (QCD) cannot be employed [10, 12]. This contribution can also be computed via the dispersive integral

$$a_\mu^{\mathrm{HLO}} = \frac{\alpha_0^2}{3\pi^2} \int_{4m_\pi^2 c^4}^{\infty} ds K(s) \sigma^{(0)}(s) \tag{1.19}$$

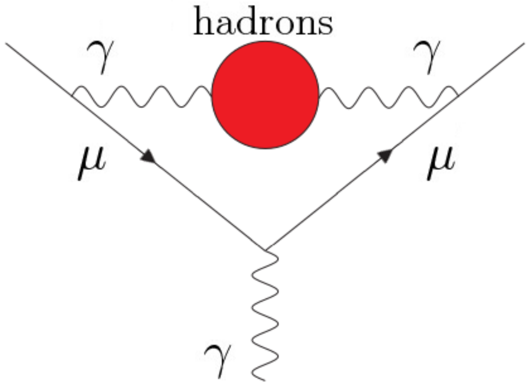

FIGURE 1.4. Hadronic leading-order self-interaction process – edited from [10].

where m_π is the pion mass, $K(s)$ is the kernel function

$$K(s) = \int_0^1 dx \frac{x^2(1-x)}{x^2 + (1-x)s/m_\mu^2 c^4} \sim \frac{1}{s} \tag{1.20}$$

and $\sigma^{(0)}(s)$ is the total cross section for e^+e^- annihilation into hadrons (figure 1.5a), determined experimentally, subtracted from initial-state radiative (figure 1.5b) and vacuum polarization corrections and supplemented by perturbative QCD at high energy scale [2, 10, 12, 15].

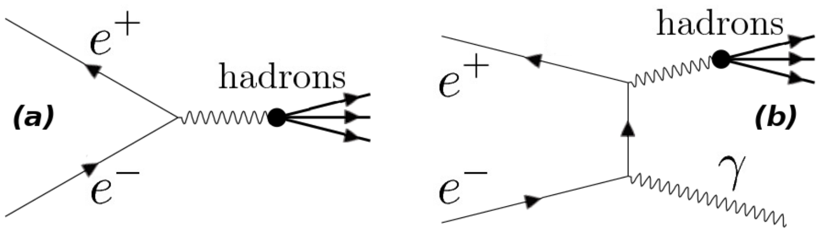

FIGURE 1.5. e^+e^- annihilation into hadrons, without *(a)* and with *(b)* Initial State Radiation (ISR) emission – edited from [16].

The behaviour of $K(s)$ highlighted in equation 1.20 gives a strong weight to the low-energy part of the integral in equation 1.19: about 91% of the total result of a_μ^{HLO} comes from center-of-mass energies $\sqrt{s} < 1.8$ GeV and 73% of it comes from the two-pion final state which is dominated by the $\rho(770)$ resonance [10].
The evaluation of the dispersive integral in equation 1.19 can be improved by integrating the e^+e^- data with the spectra of the hadronic τ decays (figure 1.6). Indeed, with proper isospin-breaking corrections, the isovector part of the cross section for e^+e^- annihilation into hadrons can be calculated from τ decay data [10]. Details on the general outline of this procedure and on many different analyses can be found in [10, 17–19].

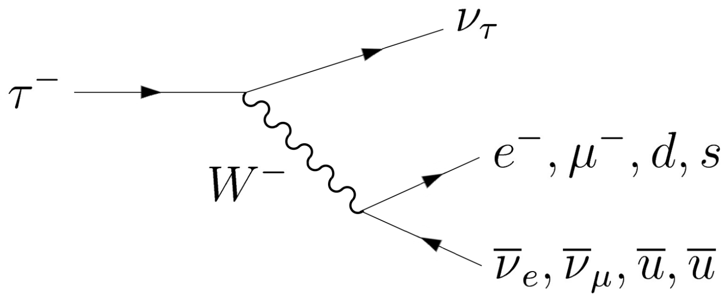

FIGURE 1.6. Main τ decay channels; due to its large mass the τ is the only lepton that undergoes decays into hadronic states – here $\nu_\tau d\overline{u}$ and $\nu_\tau s\overline{u}$. Edited from [20].

The resulting contributions are

$$a_\mu^{\mathrm{HLO}}[e^+e^-] = 6923(42)(3) \times 10^{-11} \tag{1.21}$$

where errors come from the experimental cross section and from the perturbative QCD respectively, and

$$a_\mu^{\mathrm{HLO}}[\tau] = 7015(42)(19)(3) \times 10^{-11} \tag{1.22}$$

where errors come from the experimental spectrum, from the the isospin-breaking corrections and from perturbative QCD respectively [2, 21]. Although these two values differ by 1.8σ, very recent studies claim the full consistency between the two datasets [2, 22].
Alternatively, a_μ^{HLO} can be evaluated via lattice QCD calculations: albeit promising, the results of this method are not as precise as the ones of the dispersive approach [23, 24]. In general, all the approaches to the determination of a_μ^{HLO} share the important limitation of being heavily model-dependent; since the e^+e^- data are more directly related to the calculation of a_μ^{HLO} than the τ ones, all the recent analyses do not include the latter [22].

1.3.2.3 Experimental data

In order to get $\sigma^{(0)}(s)$ which appears in equation 1.19, experimental data on the total observed cross section $\sigma(s)$ are required [10]. The exclusive low-energy cross sections have been measured by many experiments [10, 12, 17]. Since at energies above $2.5 - 3.1$ GeV the output hadron multiplicity is much higher, exclusive measurements of each hadronic final state are infeasible; consequently, results on $R(s)$, the ratio between $\sigma^{(0)}(s)$ (already corrected for initial-state radiation and vacuum polarization) and the high-energy limit of the Born cross section for e^+e^- into $\mu^+\mu^-$, from various inclusive measurements performed at high-energy colliders are used [10, 12, 17].

In particular, the CMD-2 and SND data for e^+e^- into $\pi^+\pi^-$ with center-of-mass energy in the $(0.37, 1.39)$ GeV range played a major role among the exclusive results [10, 12]; these data were collected with the traditional energy scan method, i.e. varying the center-of-mass energy over a wide range [12, 25, 26].
On the other hand, most of the modern e^+e^- colliders, being designed for a fixed center-of-mass energy, exploit the so-called radiative return method: since input particles can emit electromagnetic radiation before colliding (ISR – figure 1.5b) the effective center-of-mass energy of the collision can take any value in the $(m_{\text{thr}}, 2E)$ range, where m_{thr} is the hadronic production threshold and E is the beam energy; details on this method can be found in [16]. The KLOE experiment (figure 1.7) at DAΦNE measured the cross section for e^+e^- into $\pi^+\pi^-$ in the $(0.59, 0.97)$ GeV range [12, 27, 28] and later in the $(0.32, 0.97)$ GeV range [29–31] with the radiative return method at the $\phi(1020)$ resonance. The highest-precision contribution in the region up to 2.2 GeV comes from the BABAR (figure 1.8) results (figure 1.9), which also cover the previously unexplored $(2.2, 4.5)$ GeV range [12, 32–34]. Recent measurements performed by the CMD-3 [35] and BES-III [36–38] experiments are consistent with these results.

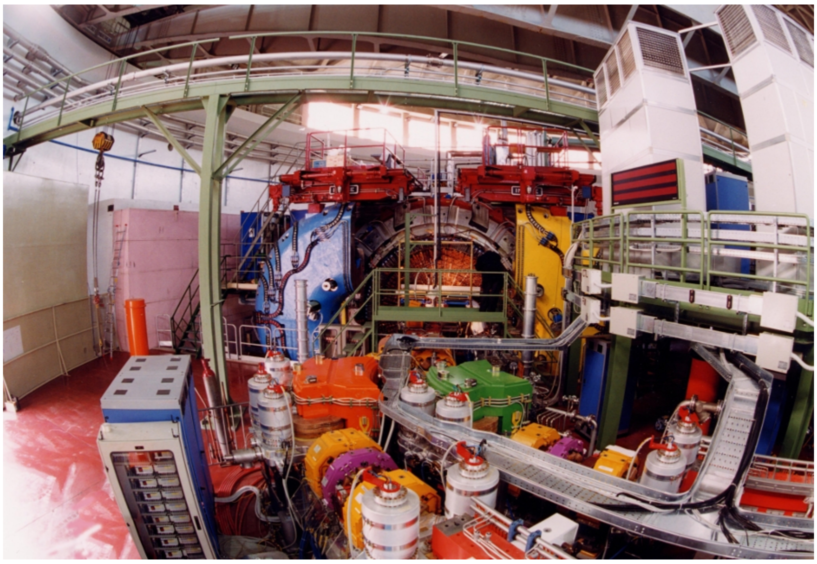

Figure 1.7. The KLOE detector [39].

Results on the τ hadronic decay spectra mainly come from ALEPH measurements [17, 41, 42]; many studies also rely on data from the BELLE, CLEO and OPAL experiments [10, 12, 19]. Some discrepancies between the different datasets emerge, probably due to the different experimental conditions and analysis methods; many studies are being performed on this topic [19, 43].

FIGURE 1.8. The BABAR detector [40].

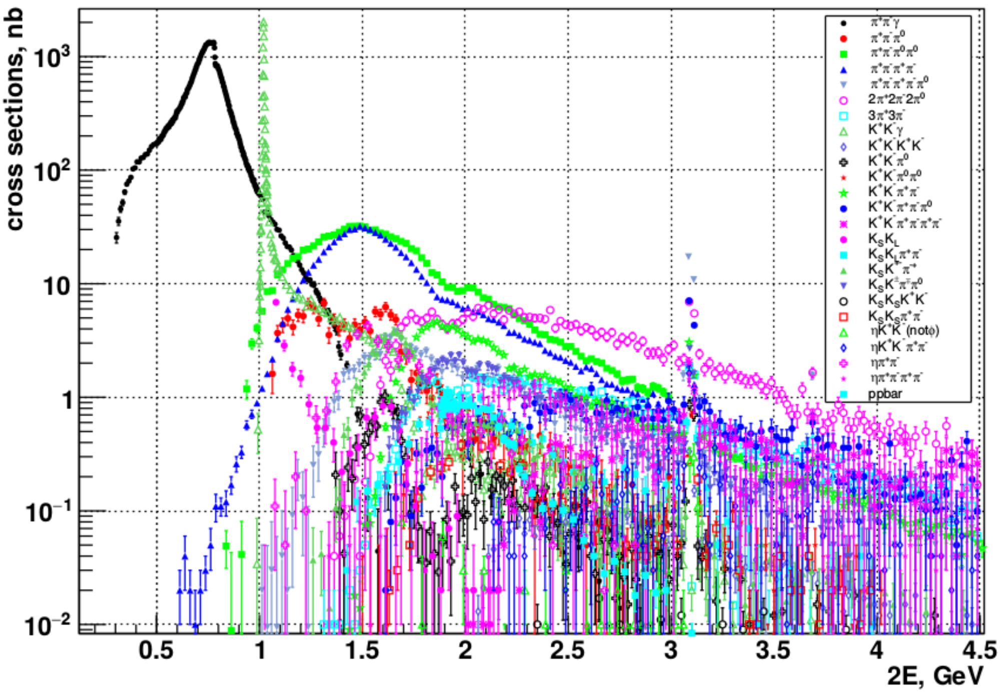

FIGURE 1.9. Summary of the BABAR measurements of the cross sections for e^+e^- into hadronic states [33].

1.3.2.4 HHO terms

Unlike the electromagnetic and electroweak cases, hadronic self-interaction processes with 7 interaction vertices (next-to-leading-order) can play an important role in the composition of a_μ^{SM}; indeed, equation 1.14 shows that an important part of the total uncertainty comes from the higher-order hadronic term. The latter can be split into two parts, i.e.

$$a_\mu^{\mathrm{HNLO}} = a_\mu^{\mathrm{HNLO}}[\mathrm{VP}] + a_\mu^{\mathrm{HNLO}}[\mathrm{LBL}] \tag{1.23}$$

where the first term on the right side of the equation is related to hadronic vacuum polarization processes (figure 1.10a and 1.10b), similar to the electromagnetic and electroweak ones described in the previous sections, while the second term is related to hadronic light-by-light scattering (figure 1.10c) [10].

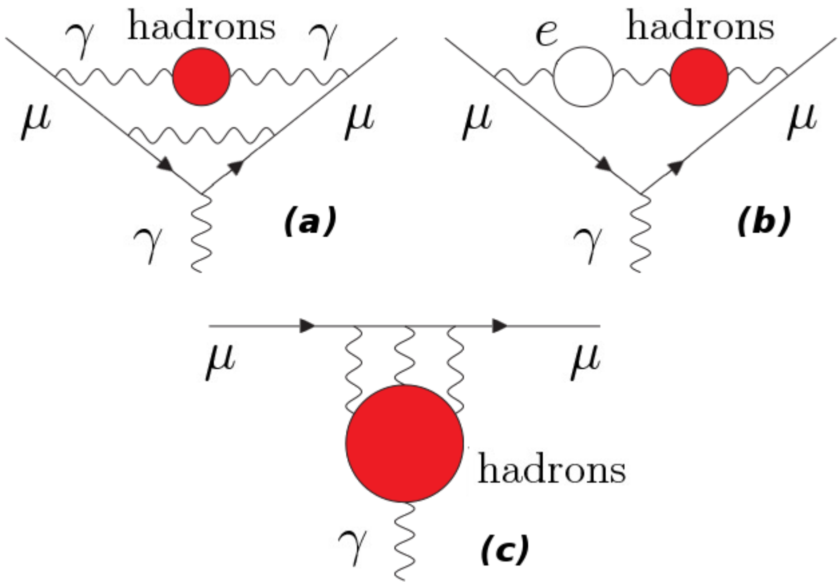

FIGURE 1.10. Some hadronic next-to-leading-order self-interaction processes: *(a-b)* hadronic vacuum polarization; *(c)* hadronic light-by-light scattering. Edited from [10].

Like in the hadronic leading-order case, the $a_\mu^{\mathrm{HNLO}}[\mathrm{VP}]$ evaluation relies either on the experimental cross section for e^+e^- annihilation into hadrons or on the τ hadronic decay spectra [10, 44]. On the other hand, $a_\mu^{\mathrm{HNLO}}[\mathrm{LBL}]$ cannot be expressed in terms of experimental observables and its determination therefore relies on merely theoretical procedures [10, 45]. Currently the contribution of processes with 9 interaction vertices (next-to-next-to-leading-order – some examples in figure 1.11) is under study; the result $a_\mu^{\mathrm{HNNLO}} = 12.4(0.1) \times 10^{-11}$ is reported in [44, 46].

The total prediction for equation 1.23 is

$$a_\mu^{\mathrm{HNLO}} = 7(26) \times 10^{-11} \tag{1.24}$$

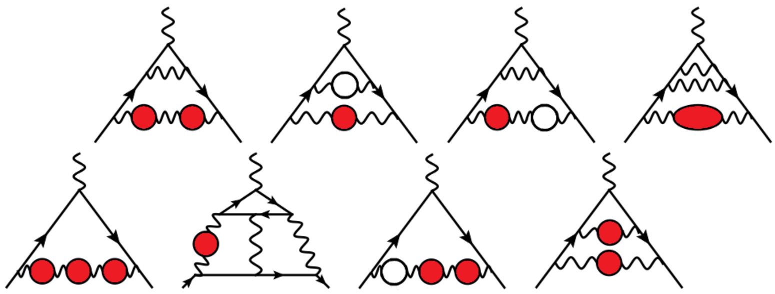

FIGURE 1.11. Some hadronic next-to-next-to-leading-order self-interaction processes – edited from [44].

where the error is dominated by hadronic light-by-light uncertainties [2].

1.4 The a_μ discrepancy: a hint of New Physics?

Adding equations 1.12, 1.18, 1.21 and 1.24 and combining all the errors in quadrature result in equation 1.14, which is the overall SM prediction of the muon magnetic anomaly. This has to be compared with the present experimental value

$$a_\mu^{\text{exp}} = 116592091(54)(33) \times 10^{-11} \tag{1.25}$$

where the first error is statistical and the second systematic [2]. Taking the difference between equations 1.25 and 1.14 and adding all the errors in quadrature leads to

$$\Delta a_\mu = a_\mu^{\text{exp}} - a_\mu^{\text{SM}} = 288(80) \times 10^{-11} \tag{1.26}$$

which represents a 3.6σ discrepancy between the SM and the measurements. Although, as already discussed, many contributions to the SM prediction are model- and dataset-dependent, most of the independent calculations lead to discrepancies at the $(2,4)\sigma$ level [2, 10, 11, 22, 24, 47]. Figure 1.12 shows the values of $-\Delta a_\mu$ for many recent results on a_μ^{SM}.
Assuming that the various experimental results are correct due to their consistency, such a discrepancy can be explained in several ways:

- an error in the determination of the hadronic light-by-light term can contribute; however, if this were the only cause for the discrepancy, then a_μ^{HNLO}[LBL] would have to move up by at least 8σ to fix it: this solution seems unlikely, at least as the predominant one [22].

- There can be errors in the determination of the hadronic leading-order term; indeed, the present theory lacks a description of the hadronic interaction based on first principles [22].

- New Physics processes can contribute to the muon magnetic anomaly; this would imply that the SM is incomplete and therefore provides insufficient information for the anomaly prediction [22].

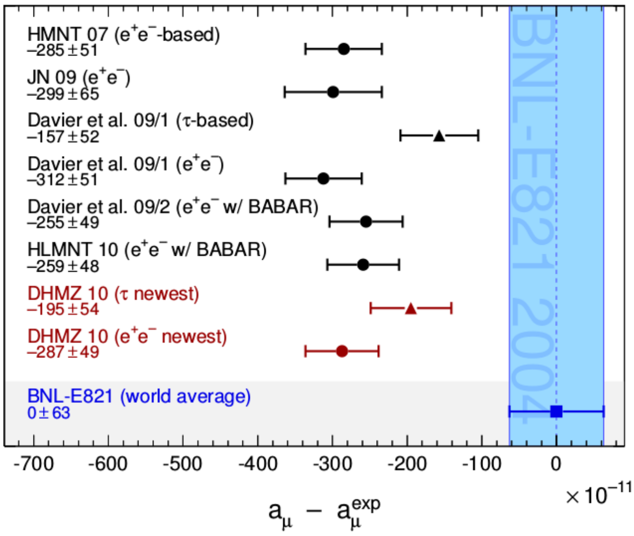

FIGURE 1.12. Recent results on $a_\mu^{\mathrm{SM}} - a_\mu^{\mathrm{exp}}$ from various independent calculations; the last row concerns the present experimental value and the shaded vertical band indicates its error [48].

Currently extensive studies are being performed on the last two items; a description of the several under development experiments will be given in section 1.6.

1.4.1 What about a_τ?

The τ mass and lifetime values are reported in table 1.1. Since $m_\tau \sim 17 m_\mu$, equation 1.13 shows that the τ anomaly might be better than the muon one as a probe for SM testing and for searching New Physics. Nevertheless its ~ 0.3 ps lifetime makes any precise direct measurement unachievable with the present technology [10, 50].
Nowadays, the τ magnetic anomaly can only be determined indirectly via the characterization of the τ decay products, using the several channels that are open for this lepton [50]. The most precise measurement was performed by DELPHI with the result [2]

$$-0.052 < a_\tau^{\mathrm{exp}} < 0.013 \tag{1.27}$$

where the 95% CL (Confidence Level) boundaries have been considered; therefore, even the sign of the anomaly is currently unknown [50]. Nevertheless the potential of the next-generation B-factory BELLE-II (figure 1.13) in terms of the high τ pairs production intensity represents a great opportunity to improve this result [50].

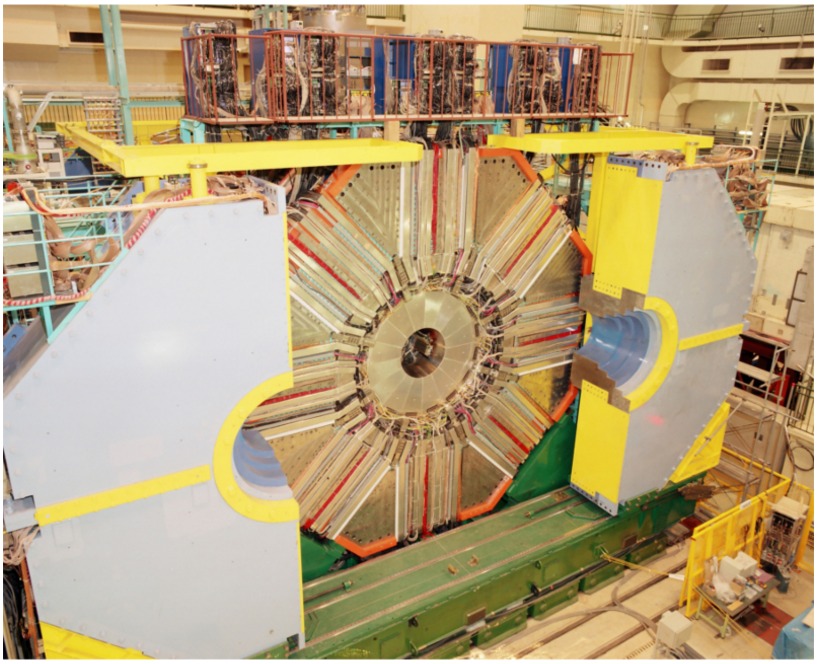

FIGURE 1.13. The BELLE-II detector [49].

1.5 The precession experiments

The first measurements of the muon magnetic anomaly were performed in the Fifties with ~ 100 MeV cyclotrons and the magnetic resonance technique; the precision achieved on $g_\mu^{\rm exp}$ was $\sim 0.09\%$, i.e. $\sim 35\%$ for $a_\mu^{\rm exp}$ [51]. These early experiments goal was not the discovery of exotic interactions of the muon but rather the characterization of the muon itself and of its place in the classification of the fundamental particles [51].
All the modern measurements of $a_\mu^{\rm exp}$ have been performed with the precession technique [8]. In such a configuration, the spinning charged particle under study experiences a uniform static magnetic field $\overline{B}$ and therefore moves on a circular orbit in a plane perpendicular to it [8]. If the particle moves at $v \ll c$ then its angular frequency vector is

$$\overline{\omega}_{\rm C} = \frac{e}{mc}\overline{B} \tag{1.28}$$

while its spin precession frequency vector is

$$\overline{\omega}_{\rm S} = (1+a)\frac{e}{mc}\overline{B} \tag{1.29}$$

which depends on the magnetic anomaly [8]. The difference between equations 1.28 and 1.29 is

$$\overline{\omega}_a = \overline{\omega}_{\rm S} - \overline{\omega}_{\rm C} = a\frac{e}{mc}\overline{B} \tag{1.30}$$

which is nonzero if $a \neq 0$; in this case there is a precession between the momentum and spin vectors [8].

Since $a_e \sim a_\mu \sim 10^{-3}$, it takes about a thousand turns for the spin vector of a lepton to perform a 2π rotation about $\overline{B}$ and therefore many thousands turns are needed for any precise measurement of a [8]. For the electron measurements this does not represent an issue, since electrons are stable; on the other hand muons decay in ~ 2 µs, so any prolonged measurement is problematic [8]. Fortunately, relativistic time dilation makes fast muons live longer: it is therefore convenient to perform precession experiments with high-energy muons [8]. In this case equations 1.28 and 1.29 must be rewritten: the relativistic equations are

$$\overline{\omega}_{\mathrm{C}} = \frac{e}{mc}\left[\frac{\overline{B}}{\gamma} - \left(\frac{\gamma}{\gamma^2-1}\right)\overline{\beta}\times\overline{E}\right] \tag{1.31}$$

and

$$\overline{\omega}_{\mathrm{S}} = \frac{e}{mc}\left[\left(a+\frac{1}{\gamma}\right)\overline{B} + \left(\frac{1-\gamma}{\gamma^2-1} - a\right)\overline{\beta}\times\overline{E}\right] \tag{1.32}$$

respectively; here $\overline{\beta} = \overline{v}/c$ is the particle velocity normalized to the speed of light, $\gamma = 1/\sqrt{1-\beta^2}$ is the relativistic Lorentz factor and $\overline{E}$ is the confining electric field [8]. Equation 1.30 becomes

$$\overline{\omega}_a = \frac{e}{mc}\left[a\overline{B} + \left(\frac{1}{\gamma^2-1} - a\right)\overline{\beta}\times\overline{E}\right] \tag{1.33}$$

in which a appears twice [8]. Nevertheless, the second term on the right side of equation 1.33 vanishes with the so-called magic γ, i.e. for $\gamma = \sqrt{1+1/a} \sim 29.3$ with the value reported in equation 1.14: this makes $p = m\sqrt{\gamma^2-1} \sim 3.09$ GeV/c a convenient choice for the input muon momentum since it makes the measurement independent on the confining electric field [11].
It has to be noted that equations 1.31 and 1.32 have been derived under the hypotheses of zero transverse fields, i.e. $\overline{\beta}\cdot\overline{B} = \overline{\beta}\cdot\overline{E} = 0$, and of zero electric dipole moment for the muon[1] [8].
In practice, precession experiments on the muon magnetic anomaly consist in confining high energy muons in a uniform static magnetic field, making them complete as many 2π turns as possible and measuring their polarization vectors [8]. A precise map of the field is needed in order to achieve highly precise a_μ^{exp} results. Field measurements are often based on proton NMR, so their results are expressed in terms of the proton Larmor frequency $\overline{\omega}_p = 2\overline{\mu}_p B/\hbar$ where $\overline{\mu}_p$ is the total proton magnetic moment; moreover [8]

$$a_\mu = \frac{\omega_a/\omega_p}{\lambda - \omega_a/\omega_p} \tag{1.34}$$

where λ is the muon-to-proton magnetic ratio, currently known with 26 ppb precision from muonium spectroscopy [2, 55].

[1]Indeed the EDM of the fundamental particles might play another important role in the quest for New Physics effects; in particular, the muon EDM has been and will be studied in most of the magnetic anomaly experiments [8, 47, 52–54]. The current value is $|d_\mu| = -0.1(0.9)\ e\cdot\mathrm{cm}$, fully compatible with zero [2].

1.5.1 Polarization

In principle, polarizing the input muons and performing polarization measurements could represent a major challenge [8]. The initial issues with the feasibility of these experimental conditions were solved when parity violation was discovered: the main decay channel of the spin-0 positive (negative) pion is

$$\pi^+ \to \mu^+ \nu_\mu \qquad \left(\pi^- \to \mu^- \overline{\nu}_\mu\right) \tag{1.35}$$

which, thanks to the short range of the weak force, has zero final orbital angular momentum; parity violation implies that the neutrino (antineutrino) helicity is -1 $(+1)$ in the pion rest frame and the total angular momentum must be conserved, so the muon must have helicity -1 $(+1)$, i.e. it is born longitudinally polarized in the pion rest frame [8, 11, 56, 57]. This process, which is depicted in figure 1.14, makes the practical realization of highly-polarized muon beams feasible [8, 11, 56, 57].

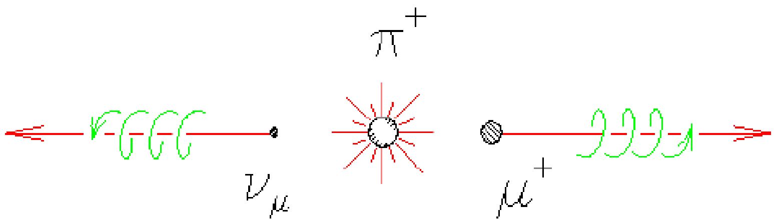

FIGURE 1.14. Positive pion parity-violating decay [58].

Furthermore, the angular distribution of the electrons emitted in

$$\mu^+ \to \overline{\nu}_\mu e^+ \nu_e \qquad \left(\mu^- \to \nu_\mu e^- \overline{\nu}_e\right) \tag{1.36}$$

is asymmetrical, thus allowing to trace the longitudinal polarization of the muon sample as a function of time [8, 11, 56].

1.5.2 At the CERN synchro-cyclotron

The first measurement of the muon magnetic anomaly at CERN (1958-1962) exploited ~ 150 MeV/c positive muons resulting from the pion in-flight decays inside the synchro-cyclotron (figure 1.15) [8]. The muon beam hit a beryllium absorber placed at one end of a 6 m long bending magnet (scheme in figure 1.16): this reduced the momentum to ~ 90 MeV/c, thus making the muons describe smaller circular orbits that could be fully contained within the ~ 1.6 T magnetic field region [8]. A transverse field gradient made the orbits drift along the whole length of the magnet, away from the input absorber and towards the ejection point. Such a gradient was a function of the longitudinal position inside the magnet: particles drifted faster at the magnet ends, in order to ease the injection and the ejection, and slower in the central storage region, thus completing as many turns as possible; storage times in the $(2, 8)$ µs range, corresponding to ~ 1000 complete turns, were achieved [8].

FIGURE 1.15. The CERN synchro-cyclotron [59].

After the ejection, the muons were stopped in a polarization analyzer, consisting of a non-depolarizing bulk situated far from the magnetic field and surrounded by scintillating multiplicity counters, and underwent the decay shown in equation 1.36 [8]. The polarization was measured by means of the asymmetry

$$A(t) = \frac{n^+(t) - n^-(t)}{n^+(t) + n^-(t)} \tag{1.37}$$

where t is the storage time (measured with counters placed at the magnet input and output) and $n^+(t)$ ($n^-(t)$) is the count rate in the forward (backward) direction with respect to the ejected muon momentum [8].
Figure 1.17 shows the measurements of $A(t)$, whose sinusoidal modulation is evident; from

$$A(t) = A_0 \sin(\omega_a t + \phi) \tag{1.38}$$

the module of equation 1.33 (with no electric field component), and therefore the value of the magnetic anomaly, were extracted [8]. The final result was

$$a_\mu^{\text{exp}} = 116200000(500000) \times 10^{-11} \tag{1.39}$$

which agreed very well with the theoretical predictions available at the time [8].

1.5.3 At the CERN MSRs

At the beginning of the Sixties the importance of the $g-2$ experiments for QED precision testing and for the study of the difference between the electron and the

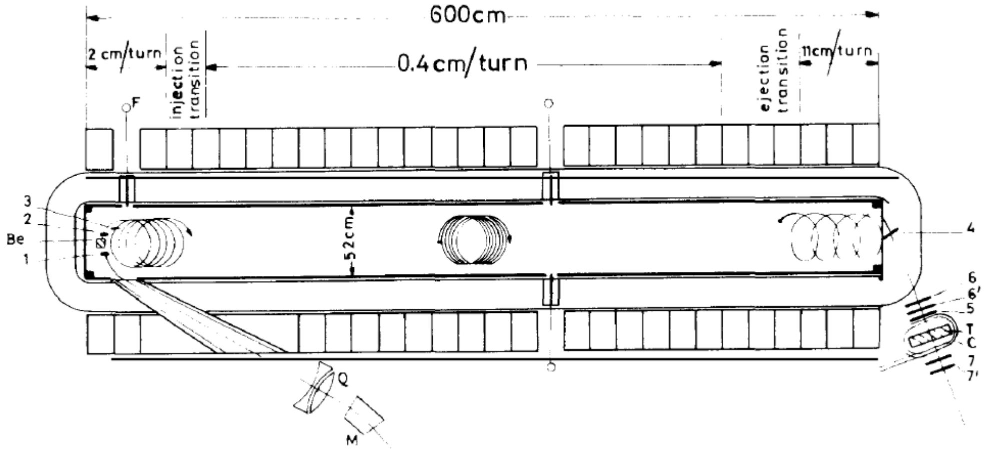

FIGURE 1.16. Scheme of the horizontal section of the bending magnet of the first a_μ experiment at CERN [8]: the injection (ejection) point is at the left (right) side of the figure; the polarization analyzer is at the lower right corner.

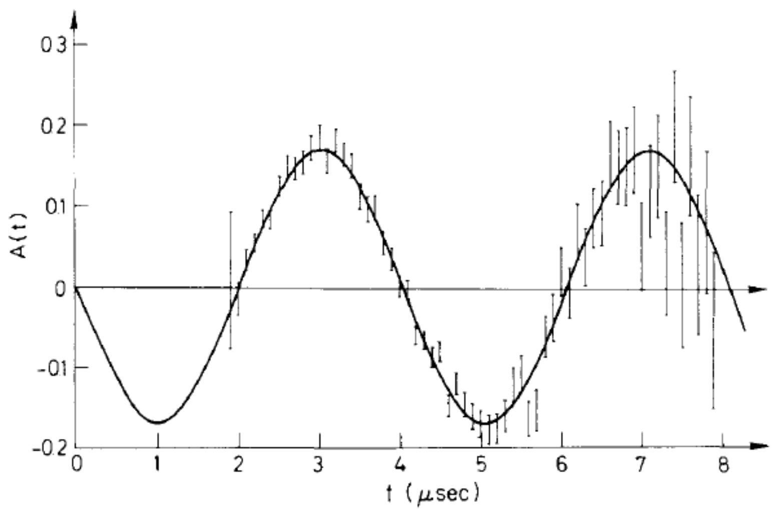

FIGURE 1.17. Sinusoidal modulation of the forward-backward asymmetry $A(t)$ [8].

muon was well-established; this led to the development of a dedicated storage ring [8]. Many changes in the experimental layout were made:

- the high-energy protons of the Proton Synchrotron (PS) made higher-energy pions, and in turn higher-energy muons with longer lifetime, available [8].
- The electrons under study were created by the muon in-flight decays and emerged inward, so the detectors were placed in the inner part of the ring [8].
- Energy sensitive detectors were used: this allowed the selection of the highest-energy electrons, i.e. of the electrons that are emitted forward in the muon rest frame [8].

1.5.3.1 The first MSR (1962-1968)

The first storage ring exploited a 5 m diameter magnet with a properly-shaped ~ 1.7 T field and the 10.5 GeV proton pulses extracted from the PS; the momentum of the muons in the stable orbits was 1.27 GeV/c [8]. The proton bunches hit a target located inside the ring, in order to minimize the pion loss and hence maximize the final beam intensity; nevertheless, this configuration introduced massive background radiation, so the detectors had to be properly shielded [8]. Vertical focusing was obtained with a radial field gradient [8]. A scheme of the first MSR is shown in figure 1.18.

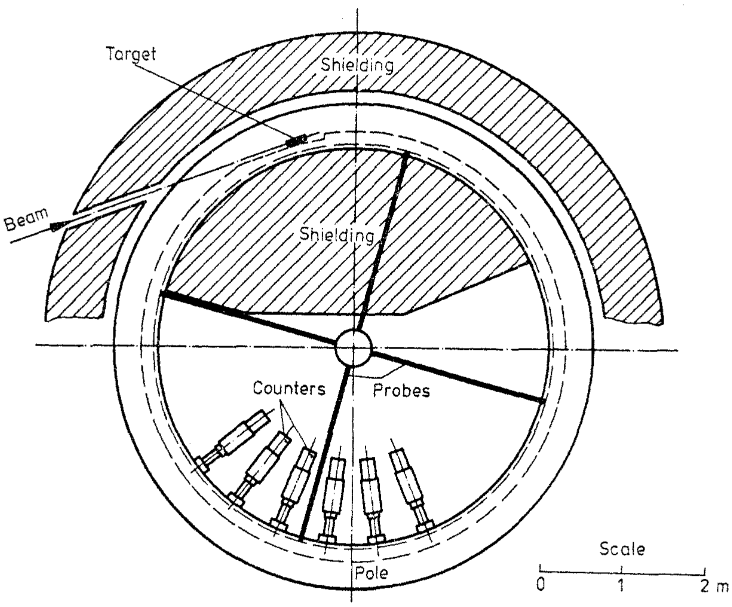

FIGURE 1.18. Scheme of the CERN first MSR [5].

The highest-energy electron count rate was modeled as

$$N(t) = N_0 e^{-t/\tau_\mu}[1 - A\cos(\omega_a t + \phi)] \tag{1.40}$$

in which the exponential factor represents the muon decay and the sinusoidal factor represents the anomaly-dependent modulation; A is an asymmetry factor which includes the polarization of the muon sample [5, 8]. As can be seen in figure 1.19, $30 - 40$ full modulations per bunch could be achieved thanks to the muon dilated lifetime of ~ 27 μs [5, 8].

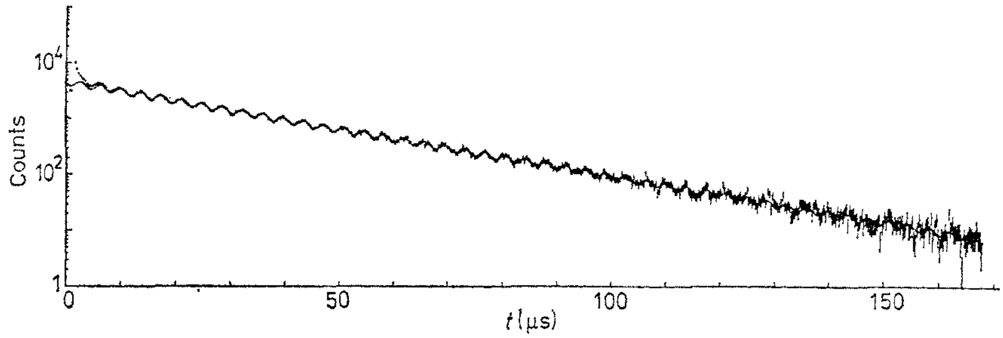

FIGURE 1.19. Modulation of the highest-energy electron count rate $N(t)$ in the first MSR experiment [5].

The final result

$$a_\mu^{\rm exp} = 116616000(31000) \times 10^{-11} \tag{1.41}$$

represented an improvement in the precision of the muon anomaly measurement by a factor ~ 16 and was consistent with the QED predictions available at the time, e.g. the result presented in equation 1.9 in section 1.2 [8]. It has to be noted that the data collected in this experiment (as well as in the following ones) allowed the measurement of the relativistic time dilation, and hence a precision test of the special relativity at the level of 1% accuracy [8].

1.5.3.2 The second MSR (1969-1976)

Proposed in 1969, the second MSR (photo in figure 1.20 and scheme in figure 1.21) featured many major upgrades:

- the vertical focusing was performed via electric quadrupoles rather than via a radial magnetic gradient: this made the measurements less sensitive to the orbit radius, which was the main source of uncertainty in the first experiment [8].
- The electric focusing did not affect the measurement of $a_\mu^{\rm exp}$ because of the magic γ: indeed, the ring was designed for 3.09 GeV/c muons; this choice also increased the dilated lifetime to ~ 64 μs and hence the number of precession turns to more than 100 [8].

- The pion production was performed outside the storage volume and the momentum selected pion beam was injected into the storage ring by means of a pulsed inflector: this reduced the background, improved the input momentum matching to the acceptance of the storage ring and increased the initial polarization of the muon sample [8].

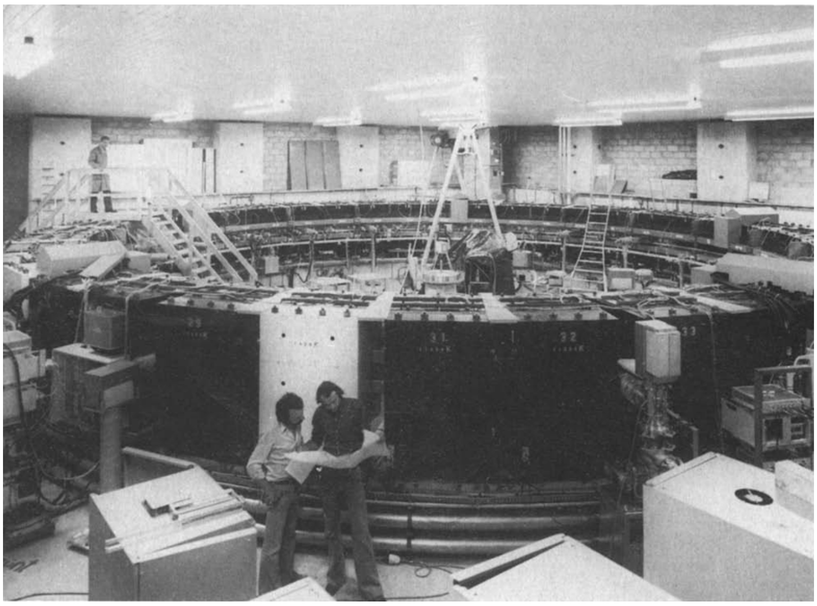

FIGURE 1.20. The CERN second MSR [60].

The ring had a diameter of 14 m. The uniform 1.47 T magnetic field was provided by 40 C-shaped bending magnets, open on the inside to allow the decay electrons to leave the ring and hit the 22 energy sensitive detectors displaced all along the inner circumference; the field was controlled to a 1 ppm precision [8].
Figure 1.22 shows the $N(t)$ distribution with a total record of 1.4×10^8 counts; the resulting value for the muon anomaly was

$$a_\mu^{\text{exp}} = 116592400(850) \times 10^{-11} \tag{1.42}$$

which was consistent with the theoretical predictions once the hadronic vacuum polarization contribution was considered [8]. At the time of the publication of these final results (1976) the muon anomaly discrepancy had not been discovered yet: it would have taken another twenty years and many technological upgrades for this effect to be unveiled.

1.5.4 E821 at BNL

The E821 experiment was commissioned in 1997 [53]. It exploited the 24 GeV protons of the AGS: bunches of 7×10^{12} protons [62] were extracted in a dedicated beamline, which featured a target for pion production and a 80 m long pion

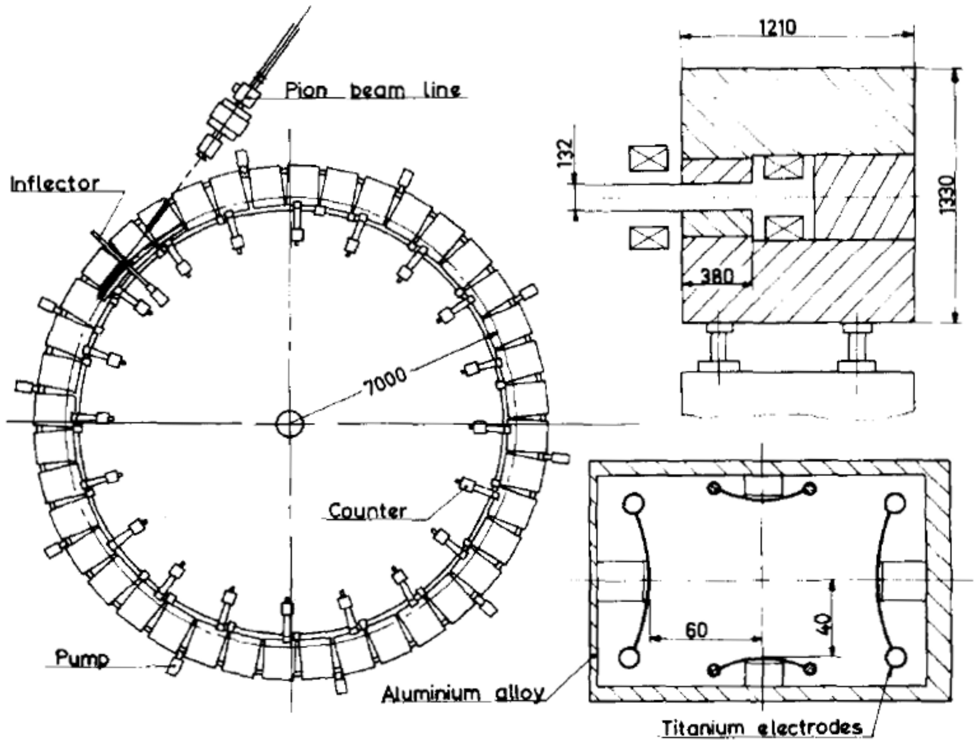

FIGURE 1.21. Scheme of the CERN second MSR [8]. Cross-sections of a C-shaped bending magnet *(top-right)* and of a focusing quadrupole *(bottom-right)* are also shown.

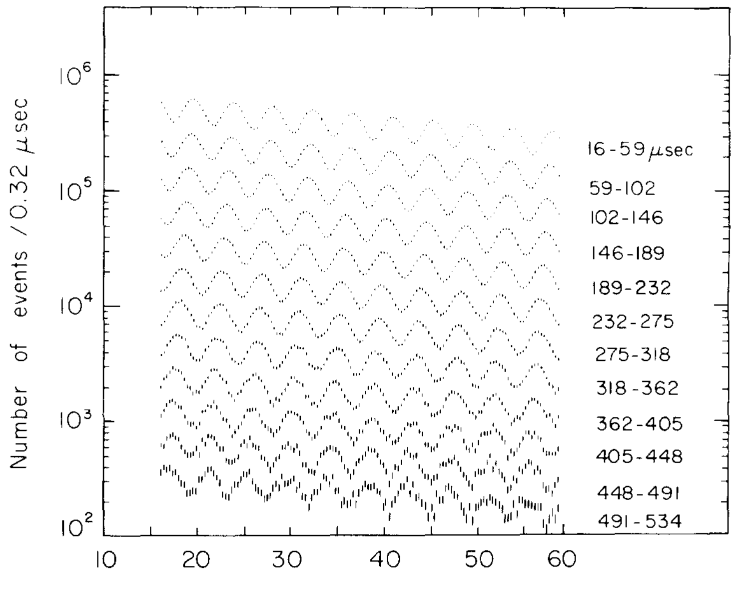

FIGURE 1.22. Modulation of the highest-energy electron count rate $N(t)$ in the second MSR experiment [8]. The total time range has been split in many lines and the time range for each line is shown on the right.

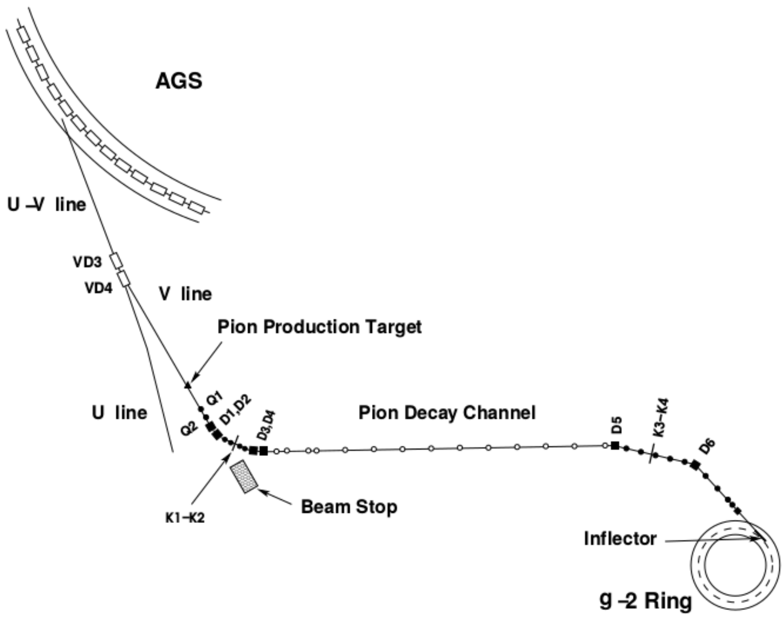

FIGURE 1.23. Beamline to the E821 storage ring [53]: the protons extracted from the AGS hit a target and produced pions, which in turn decayed in flight generating the muon beam.

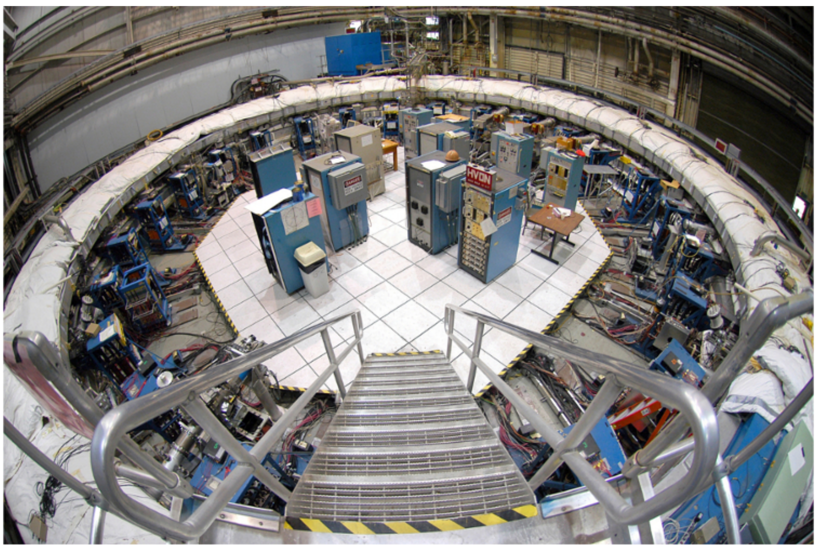

FIGURE 1.24. The E821 experiment [61].

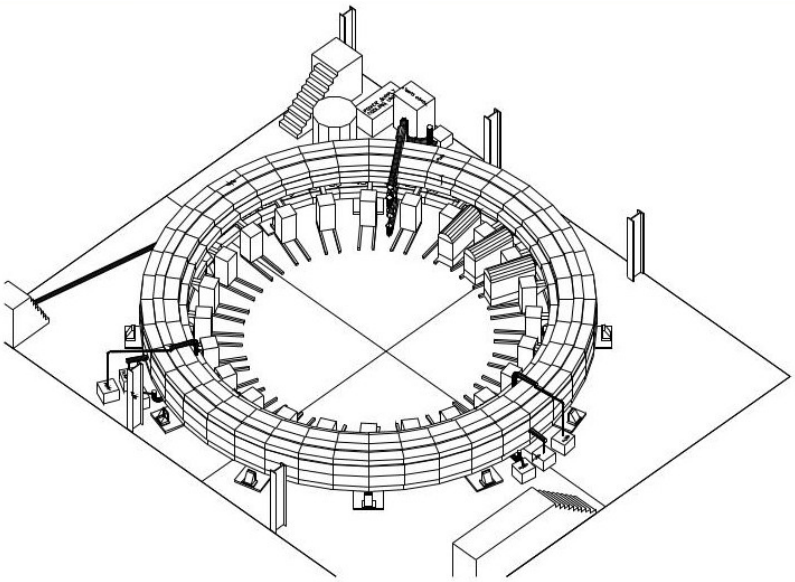

FIGURE 1.25. 3D rendering of the E821 experiment; the 24 regularly spaced boxes on rails in the inner part of the ring contain the electron detectors [53].

decay channel (figure 1.23) [53]. Despite sharing the same concept of the CERN second MSR (subsection 1.5.3), the E821 storage ring (photo in figure 1.24 and 3D rendering in figure 1.25) presented major improvements:

- as already mentioned, muons were produced outside the storage volume; this made a detailed characterization of the input muon beam possible, increased the storage efficiency and reduced the hadron-induced background [53].
- Before entering the ring, the 3.09 GeV/c muons could be selected via a spectrometer [53].
- The injection into the storage ring was performed via a superconducting 1.7 m long DC inflector with a vertical 1.5 T field; the features of the inflector allowed the filling of the ring at 33 ms intervals, i.e. at each bunch extraction from the AGS [53].
- A pulsed kicker was used to place the muons entering the ring onto stable orbits [53].
- The transverse aperture of the storage region was circular rather than rectangular, which improved the field condition [53].
- A 14.224 m continuous superconducting steel-NbTi/Cu electromagnet with a highly uniform 1.4513 T field was exploited (figure 1.26) [53].

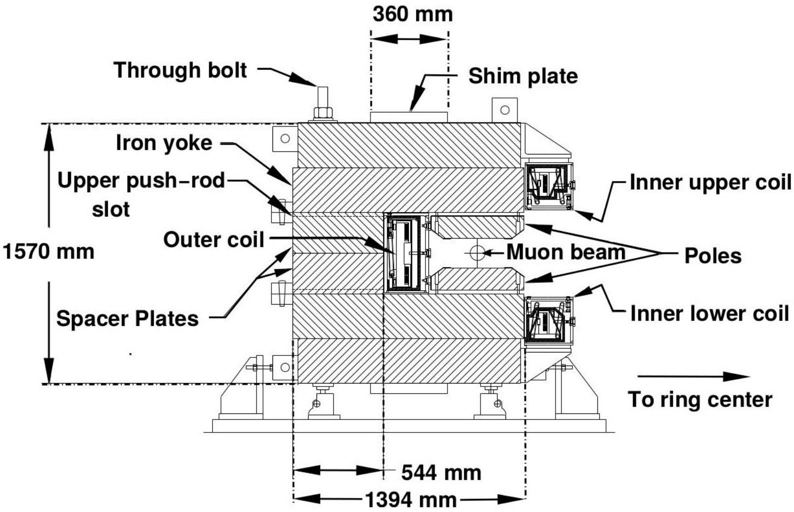

FIGURE 1.26. Transverse section of the E821 electromagnet [53]. Like in the CERN MSR cases, the inner part (on the right) is open, thus allowing the exit of the output electrons from the ring.

- The electrostatic quadrupoles allowed the operation at about twice the field gradient of the CERN second MSR experiment [53].
- The magnetic field was mapped via a trolley with 17 NMR probes that could be pulled through the vacuum chamber in addition to 378 fixed probes displaced all around the ring [53]; this configuration, along with specific calibration and analysis procedures (details in [53, 63]), allowed the measurement of the field with 0.17 ppm precision [63, 64] and its control via feedback systems with several ppm precision [53].
- Scintillating-fiber beam monitors, which could rotate into the storage region under vacuum, were used to observe directly the beam during special systematic study runs [53].
- A scintillating bar hodoscope was placed in front of each of the 24 sampling lead-plastic calorimeters distributed symmetrically in the inner part of the ring for the measurement of the muon loss rate, for the electron profiling and for timing cross-check; all the scintillating media were coupled to PMTs and read out by waveform digitizers, which were also used for the magnet voltage control [53].

This high-precision setup allowed the measurement of ω_a with a 0.21 ppm asymptotic systematic uncertainty (table 1.2) [63]. Such a high precision was combined with the 0.17 ppm asymptotic precision of the magnetic field characterization; the results of many measurements, performed over several years, are shown in table 1.3. Published in 2006, the final result (i.e. the value obtained prior to the latest re-analysis with the updated value of the muon-to-proton magnetic ratio λ needed for the magnetic field evaluation), compared with the theoretical predictions available at the time, showed the first evidence of the muon magnetic anomaly discrepancy in the $(2.2, 2.7)\sigma$ range [53].

source of errors	**size [ppm]**
coherent betatron oscillations	0.07
pileup	0.08
gain changes	0.12
lost muons	0.09
others	0.11
total	0.21

TABLE 1.2. Systematic uncertainties in the ω_a analysis [63].

experiment	**years**	$a_\mu^{exp}[\times 10^{-11}]$	**precision [ppm]**
CERN I (+)	1958-1962	116200000(500000)	4302.93
CERN II (±)	1962-1968	116616000(31000)	265.83
CERN III (±)	1969-1976	116592400(850)	7.29
E821 (+)	1997	116592510(1500)	12.86
E821 (+)	1998	116591910(590)	5.06
E821 (+)	1999	116592020(150)	1.29
E821 (+)	2000	116592040(90)	0.77
E821 (−)	2001	116592140(90)	0.77
E821 final (±)	1999-2001	116592080(63)	0.54
E821 updated (±)	1999-2001	116592091(63)	0.54

TABLE 1.3. Summary of the E821 a_μ^{exp} results [53] compared to the CERN experiments results [8]. The beam polarity is shown in brackets. The E821 final value is equal to the one presented in equation 1.25 (E821 updated) once the updated value of the muon-to-proton magnetic ratio λ is used [2, 65].

1.6 Future experiments

As already mentioned, a more precise determination of both the experimental muon magnetic anomaly (section 1.5) and the experiment-based hadronic contributions to a_μ^{SM} (subsection 1.3.2) is needed to push the value of Δa_μ above the 5σ level.

Many theoretical studies on new generation experiments have been performed – see for example [66, 67]. Currently two experiments are under development; despite the different approaches they share the aim of reaching a ~ 0.1 ppm precision on a_μ^{exp} [47, 54].

1.6.1 E989 at Fermilab

Proposed in 2009, the E989 experiment exploits the traditional method of the storage of 3.09 GeV/c muons in a uniform magnetic field, pioneered at CERN (subsection 1.5.3) and improved by the E821 collaboration (subsection 1.5.4) [68].

Indeed, the new experiment re-uses the E821 storage ring [47, 55]. Although most parts, like vacuum chambers, could be moved with standard logistics, the relocation of the electromagnet was a major issue due to its weight (~ 15 T), volume (~ 14 m diameter) and rigidity (the superconducting coils could not flex more than ~ 3 mm) [47]. Between June 22$^{\text{nd}}$ and July 26$^{\text{th}}$ 2013, the so-called Big Move took place: the electromagnet was moved from BNL in Upton, New York to Fermilab in Batavia, Illinois, with a special truck and a barge; figure 1.27 shows two stages of such a complicated operation [61]. The cooling-down of the superconducting coils and the powering-up of the main magnet were achieved in 2015 [55].

The new experiment aims at a reduction of the uncertainty to 0.14 ppm, i.e. by a factor 4 with respect to the E821 final results (last row in table 1.3) [47, 55, 61]. This would give a 5σ deviation from the SM calculations, assuming that the central values remain the same; furthermore, if the SM uncertainty improves in addition to the experimental uncertainty, the deviation could be around 8σ under the same central value assumptions [47].

The E989 beam generation exploits the Fermilab Muon Campus (figure 1.28), which consists of many repurposed and upgraded Tevatron facilities [47]. The first component of the input chain is the Booster, which accelerates protons up to 8 GeV; protons are then separated into bunches in the Recycler Ring and delivered to the target station, where positive ~ 3.1 GeV/c pions are produced and selected [69]. Most of the pions decay in flight in dedicated beamlines; the 505 m circumference Delivery Ring allows then the remaining pions to decay, as can be seen in figure 1.29, and the positive muons to be separated in time from the heavier protons; the resulting 97% polarized muon beam is then delivered to the $g-2$ storage ring for the 700 µs measurement periods [69].

Many upgrades were implemented in order to improve the experimental conditions with respect to the BNL setup:

- as already mentioned, the input stage is optimized for muon intensity maximization and hadron-induced background minimization; the expected muon yield is in the $(5, 10) \times 10^4$/fill range [55, 68].
- The kicker magnets system has been upgraded [68].

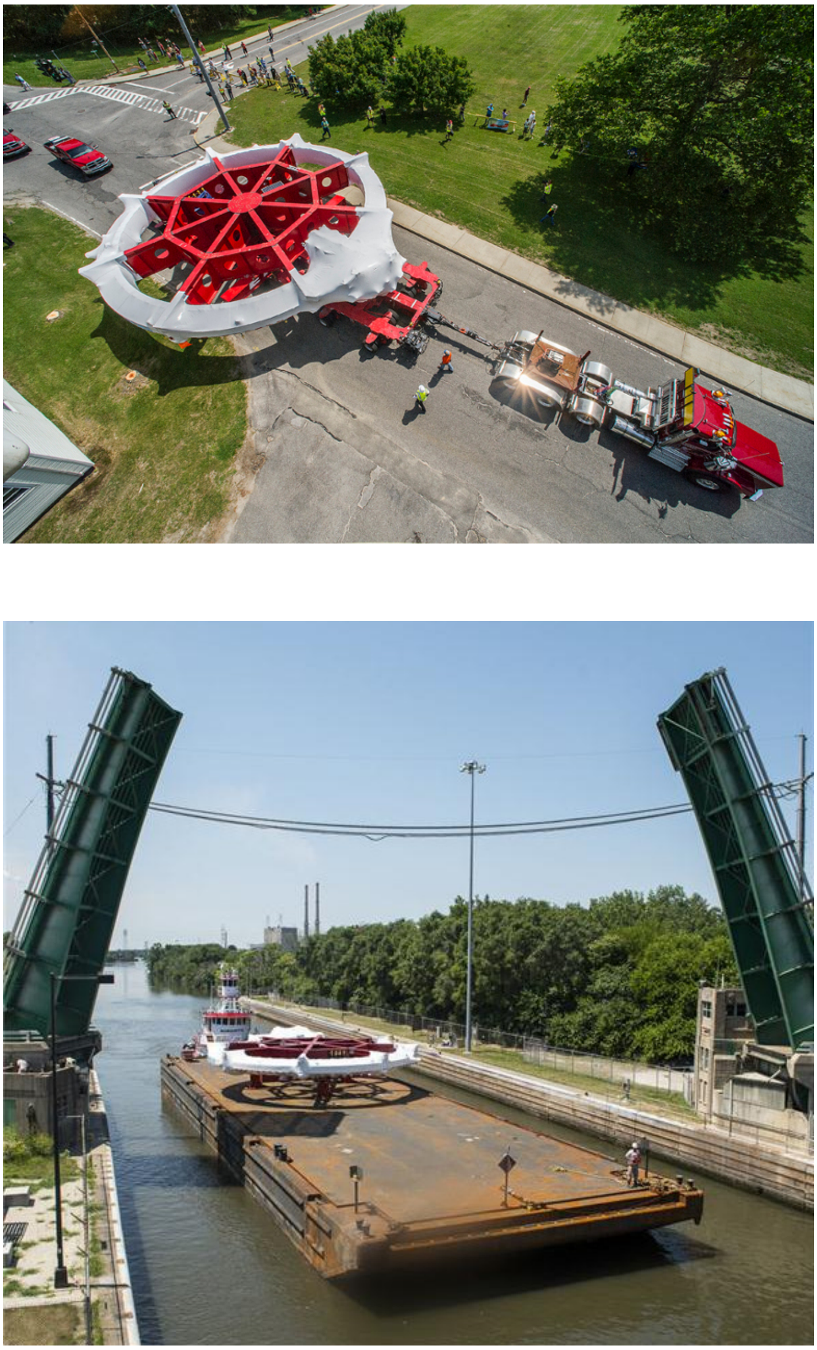

FIGURE 1.27. Two stages of the Big Move [61]: *(top)* passage out of the BNL site on June 22$^{\text{nd}}$; *(bottom)* passage on the Illinois river on July 20$^{\text{th}}$.

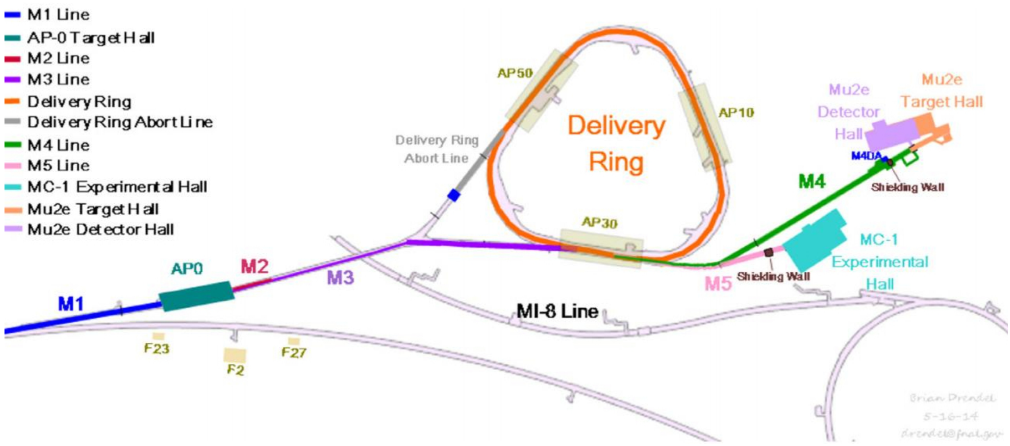

FIGURE 1.28. Beamlines of the Fermilab Muon Campus [69]: AP0 is the target station; the first section of the pion decay tunnel consists of the M2 and M3 beamlines; the M5 beamline delivers the muon beam from the Delivery Ring (DR) to the MC-1 building, which hosts the $g-2$ storage ring.

- The magnetic field uniformity has been improved during the 2015-2016 shimming program (figure 1.30): the procedure led to a ± 50 ppm field uniformity, about 4 times better than E821; the final goal on the overall field systematic uncertainty is 0.07 ppm [55, 68]. The E821 NMR probes, either fixed or mounted on the movable trolley, have been replaced [68].
- Plastic Cherenkov counters and scintillating fiber arrays are used to provide timing and profiling of the input beam [55, 68].
- 24 new generation electron calorimeters are used: each one consists of a 6×9 segmented array of $2.5 \times 2.5 \times 14$ cm^3 PbF_2 Cherenkov crystals coupled to SiPMs; the readout chain comprises custom charge-sensitive amplifiers, custom 12-bit, 800 MS/s waveform digitizers and a 20 GB/s, 100 TFLOPS (FLoating-point Operations Per Second) readout and real-time processing system [55, 68]. The fast electronics and the granular readout allow the pileup reduction [47, 68].
- The calorimeters stability over time is monitored via a laser calibration system [68].
- Straw tube planes are implemented within the vacuum pipe for positron tracking [47, 55, 68]. In particular, they have proven to be useful for the calorimeters characterization and for the muon EDM measurements [68].
- A major increase in the collected statistics will be achieved by increasing the fills per second (12 Hz) and the muons per fill ($(5, 10) \times 10^4$/fill) and by extending the overall running time; a twenty-fold increase with respect to the E821 data by summer 2020 is foreseen [55].

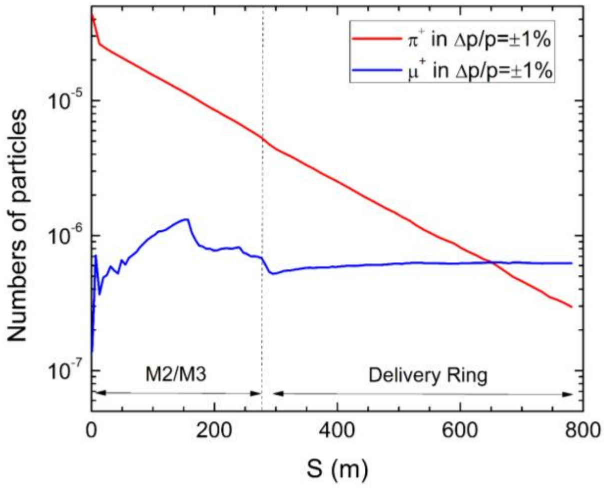

FIGURE 1.29. Simulated pion and muon loss along the pion decay section, i.e. the M2, M3 and DR beamlines; the vertical axis is scaled to the proton intensity on target; only one turn in the DR is assumed [69].

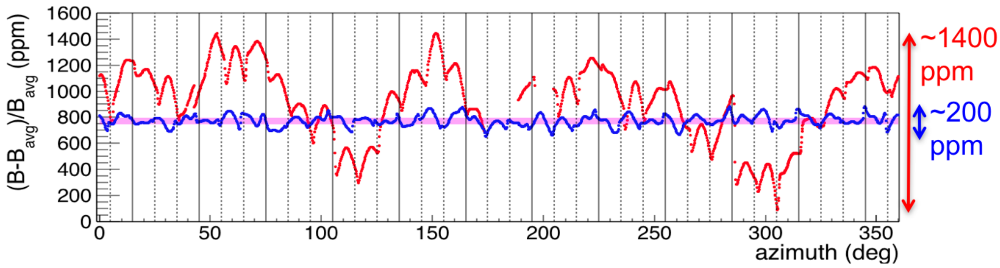

FIGURE 1.30. Magnetic field variation along the E989 storage ring: first survey (red) showed a peak-to-peak variation of ~ 1400 ppm, then reduced to ~ 200 ppm as shown in the June 2016 survey (blue); the shimming program achieved a final uniformity of ~ 100 ppm (pink band) [55].

1.6.2 E34 at J-PARC

The E34 collaboration aims at an asymptotic 0.1 ppm precision on the measurement of a_μ^{exp} [54] by pioneering a unique experimental technique based on ultra-slow positive muons [68]. The layout is depicted in figure 1.31. A 3 GeV proton beam from the MLF at J-PARC hits a graphite target [54]. Resulting 29 MeV/c surface muons, i.e. muons born from pions at rest inside the target, stop in a silica aerogel target with micro-channels, thus generating thermal muonium μ^+e^- atoms [54, 68]. Two lasers hit the muonium sample, knocking out the electrons and leaving a population of 50% polarized 3 keV/c muons [54, 68]. A new generation linac then accelerates the muons up to 300 MeV/c [54, 68]. This innovative technique allows the production of an extremely low-size and low-divergence polarized muon beam; albeit out of the magic γ condition, the electric term in equation 1.33 vanishes since the electric focusing is not necessary anymore [54].

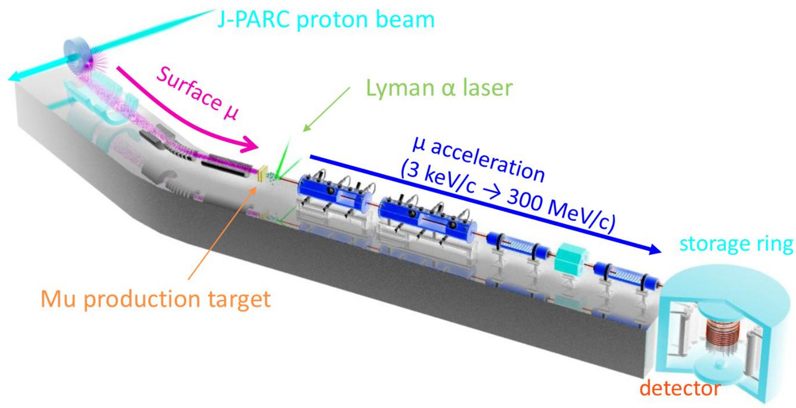

FIGURE 1.31. Concept of the E34 experiment – edited from [54].

Such a low momentum beam, ~ 10 times lower than in the CERN, BNL and Fermilab experiments, implies the need for a much smaller storage ring: indeed the proposed magnet (figure 1.32) has a 66 cm diameter and a 3 T field [68, 70]. The field has a 1 ppm local uniformity [54].
The detector consists of many silicon microstrip layers placed inside the storage field, along the whole electron circular track [54, 68]. Given the fact that the mean hit rate per silicon strip is very high due to the high intensity of the input beam, a high speed electronic chain is needed [54]. Several studies on both the sensors and the electronics are being performed [54, 68] – the updated information can be found in [70]. Despite the complicated input stage, the lower polarization degree that affects A in equation 1.40 and the 10 times shorter lifetime, this configuration presents several interesting features:

- the magnet characterization is easier [68].
- A good total electron acceptance is achieved with a compact detector [68].

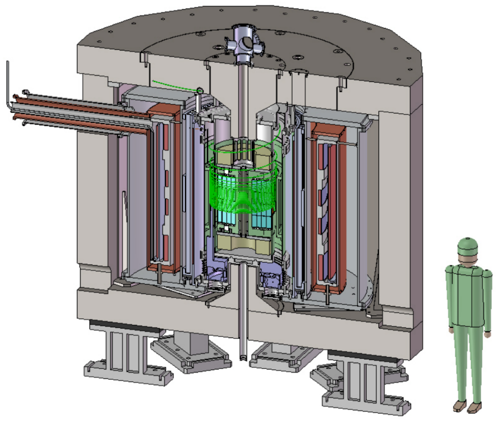

FIGURE 1.32. The compact storage ring for the E34 experiment: the green curve represents the muon beam orbit; the light blue surfaces at the center of the structure represent the silicon microstrip layers [54].

- With the proper electronic chain, the detector is relatively free of pileup and does not suffer any major gain change [68].

1.6.3 The hadronic terms: a novel experimental approach

When the results from the new generation $g-2$ experiments at Fermilab and J-PARC will reach their asymptotic precision, the uncertainty of the hadronic contributions to a_μ^{SM} will become the main limitation to the investigation on the muon anomaly mistery [71]. As already shown in section 1.3, the hadronic leading-order contribution can be evaluated via a dispersion integral that mainly relies on the experimental e^+e^- hadronic cross sections; in the low-energy range experimental results heavily fluctuate due to hadronic resonances and particle production threshold effects [71].
A novel method exploits time-like (or s-channel) processes like the ones in figure 1.5 or in figure 1.33b [71]. Indeed alternative determinations of a_μ^{HLO} can be obtained from scattering data [24, 71]. In particular

$$a_\mu^{\mathrm{HLO}} = \frac{\alpha_0}{\pi}\int_0^1 dx(1-x)\Delta\alpha_{\mathrm{had}}[t(x)] \tag{1.43}$$

where $t(x) = q^2(x) = x^2 m_\mu^2 c^4/(x-1)$ is the squared 4-momentum transfer and $\Delta\alpha_{\mathrm{had}}(t)$ is the hadronic contribution to the running of $\alpha(t)$ (figure 1.34 left), i.e. the effective value the fine-structure constant assumes in interactions with high momentum transfer[2]; here space-like (or t-channel) processes are considered, so $x \in (0,1)$ and $t(x) < 0$ [24, 71].

[2]It follows from QED that in high-energy electromagnetic processes the coupling constant, i.e. the fine-structure constant, depends on (or runs with) the squared momentum transfer q^2 – details can be found in [73, 74]

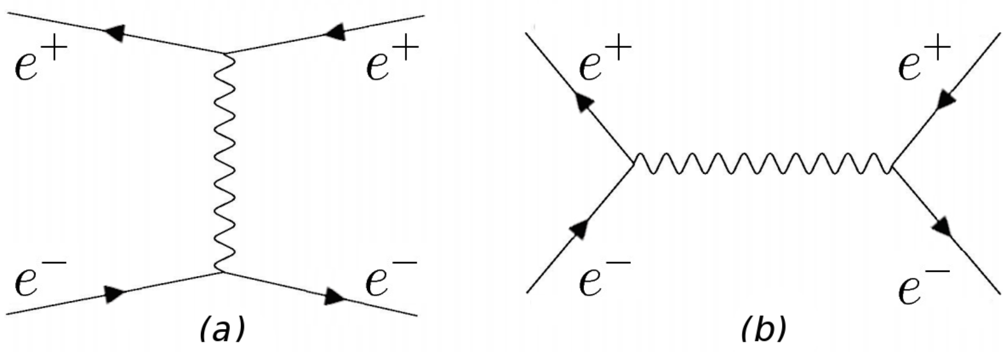

FIGURE 1.33. Lowest-order contributions to the Bhabha scattering: *(a)* t-channel; *(b)* s-channel. Edited from [72].

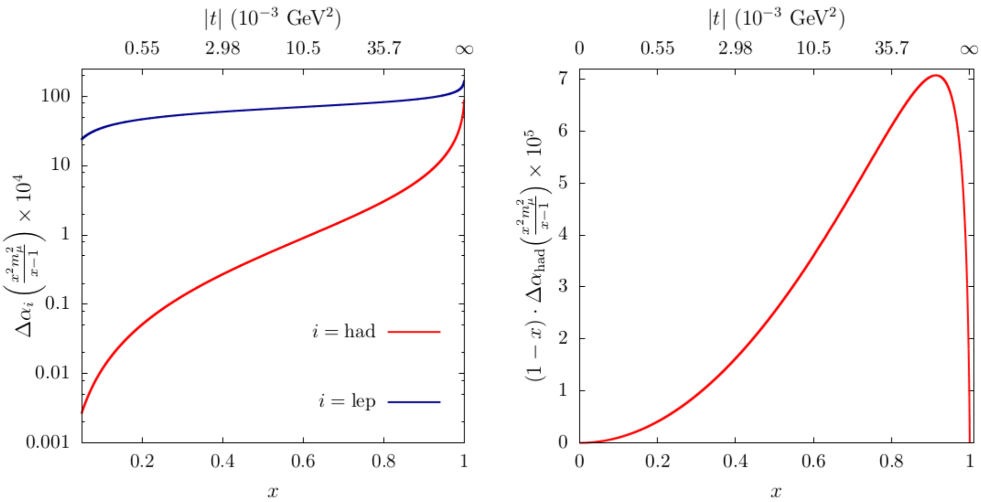

FIGURE 1.34. *(left)* Hadronic and leptonic contribution to $\alpha[t(x)]$ as a function of x and $t(x)$. *(right)* Integrand of equation 1.43 as a function of x and $t(x)$ [24].

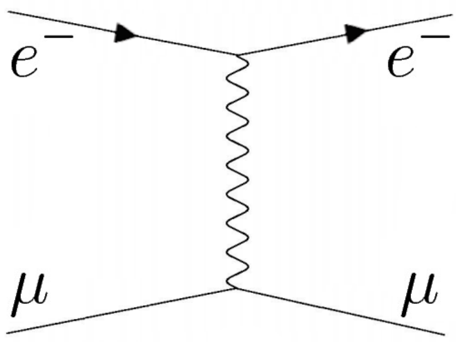

FIGURE 1.35. Lowest-order contribution to the $\mu^\pm e^-$ elastic scattering.

The running of the fine-structure constant can be expressed as

$$\alpha(t) = \frac{\alpha_0}{1 - (\Delta\alpha_{\text{lep}}(t) + \Delta\alpha_{\text{had}}(t))} \tag{1.44}$$

where α_0 is the low-energy limit defined in section 1.2 and $\Delta\alpha_{\text{lep}}(t)$ is the leptonic contribution, which is well known from perturbative calculations (figure 1.34 left) [24, 71, 74]. Therefore the evaluation of a_μ^{HLO} by means of equation 1.43 reduces itself to the experimental determination of $\alpha(t)$, from which $\Delta\alpha_{\text{had}}(t)$ can be obtained by means of equation 1.44 [24, 71]. Although both equations 1.19 and 1.43 rely on experimental data, the integrand of the latter is smooth and free of resonances (figure 1.34 right) [24].
As already mentioned, experimental data on t-channel processes are needed: both the space-like contribution to Bhabha scattering (figure 1.33a) [71] and the fully space-like $\mu^\pm e^-$ scattering (figure 1.35) [24] seem promising; details on the latter can be found in chapter 2.

CHAPTER 2

The MUonE feasibility test

As the research and development on present and future colliders pushes the frontier of particle physics to a new, unexplored energy and intensity range, several efforts are being performed worldwide on many different experimental methods that target outstanding topics within the boundaries of the Standard Model. This is the case of the $g-2$ experiments at Fermilab and J-PARC, as well as of the wide variety of projects under development within the Physics Beyond Colliders study at CERN.
Among the PBC projects, MUonE proposes a novel approach to determine the hadronic leading-order contribution to the muon magnetic anomaly via the $\mu^{\pm}e^{-}$ elastic scattering; in 2018 a feasibility test has been performed. The details of the proposal, such as the experimental concept and the beamline features, and of the feasibility test apparatus will be extensively discussed in this chapter.

2.1 Physics Beyond Colliders and the COMPASS site

Started in 2016, Physics Beyond Colliders is an exploratory study of experimental projects which target outstanding fundamental physics topics and are complementary to the operations of the LHC and the CERN future colliders; it is expected to provide new ideas and development until about 2040 [75–79].
Many PBC projects would like to exploit the CERN M2 beamline already in 2021, right after the Long Shutdown 2; a careful layout and schedule planning is therefore needed [80, 81].
The M2 beamline (scheme in figure 2.1) can deliver a high-energy, high-intensity muon beam [82, 83]. The 400 GeV/c high-intensity proton beam extracted from the Super Proton Synchrotron (SPS) hits a target, whose thickness can be chosen

to control the output flux [84]. The pions and kaons emerging from the target enter a magnetic spectrometer for high-resolution momentum selection; the output beam angular acceptance is set via collimators [82, 84]. Particles travel along two decay channels instrumented with FODO quadrupoles for beam transportation over long distances and dipoles and coils for finer momentum separation [82, 84]. The total length of the line is 1.13 km [83].

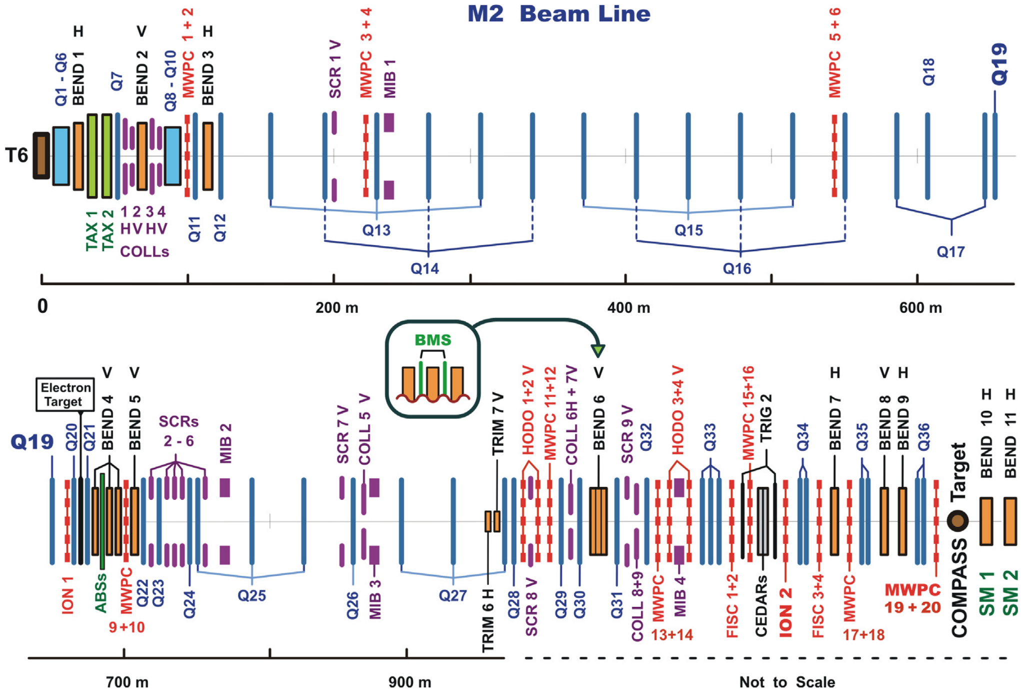

FIGURE 2.1. Scheme of the M2 beamline: T6 is the hadron production target; the ABSs are the movable beryllium modules; the 2 FODO channels are within the Q12-Q18 and Q22-Q30 ranges respectively; the beam is bent upwards by the BEND 4 and BEND 5 dipoles and is bent back horizontally by the BEND 6 dipole; the electron beam target is located right upstream with respect to BEND 4; the BMS is located at BEND 6 [82].

Nine 1.1 m thick beryllium modules are located at the end of the decay channel for the absorption of the residual hadronic component of the beam [82–84]. On the other hand, the extraction of the beryllium modules, which can be moved via remote control, makes a high-intensity hadron beam available [82, 84].
During data taking sessions with muons, a Beam Momentum Station allows the measurement of the momentum via a magnetic spectrometer surrounded by several scintillating hodoscopes with sensitivity in the momentum-spanned coordinate only [82, 84]. Furthermore, the whole beamline is instrumented with many

counters and hodoscopes for the input beam characterization while CEDARs[1] in the last section allow the input particle identification (PID) [82–84].
The muon beam momentum lies in the $(60, 190)$ GeV/c range [83] and has a momentum spread of $\pm(3,5)\%$ RMS [84]; typically 2×10^8 positive muons per extraction (with an extraction time of 4.8 s [84]) are obtained from 1.2×10^{13} protons hitting the upstream target [84]. Negative muon beams can be obtained but are less intense [84]. Muons are longitudinally polarized [83, 84].
On the other hand, the hadron beam momentum lies in the $(40, 280)$ GeV/c range [83] and can be tuned with high precision [82, 84]. Momenta above 225 GeV/c require some modifications to the beamline optics, which result in a $\sim 40\%$ smaller angular acceptance [82]. An intensity up to 10^8 hadrons per extraction can be achieved [82–84]. The main components of the positive and negative hadronic beams are shown in table 2.1. A low-energy electron beam can be delivered on demand [84].

momentum [GeV/c]	**positive beam**			**negative beam**		
	π^+	K^+	p	π^-	K^-	$\overline{p}$
100	0.618	0.015	0.367	0.958	0.018	0.024
160	0.360	0.017	0.623	0.966	0.023	0.011
190	0.240	0.014	0.746	0.968	0.024	0.008
200	0.205	0.012	0.783	0.969	0.024	0.007

Table 2.1. Main components of the M2 hadronic beams at different momenta; electron contamination is present at 100 GeV/c but rapidly drops at higher momenta due to synchrotron radiation; the relative uncertainties on these values are 1% for $\pi^\pm$ and p and in the $(2,3)\%$ range for $K^\pm$ and $\overline{p}$ [82].

Currently the M2 beamline serves the COMPASS experiment. Active since 2001, COMPASS studies the structure and the spectrum of hadronic states by scattering high-energy hadrons and polarized muons off many different fixed targets [82, 84–86]. A scheme of the COMPASS experimental layout is given in figure 2.2 while a detailed description of each component can be found in [82, 84, 85].

2.1.1 Hadron absorption and the downstream muon beam

The COMPASS setup features many stages of hadron absorption:

- scattered hadrons are stopped by the two Muon Walls, i.e. absorber layers (60 cm of iron for the Large Angle Spectrometer wall and 2.4 m of concrete for the Small Angle Spectrometer wall respectively – for the latter, see

[1] The ChErenkov Differential counters with Achromatic Ring focus perform the particle identification exploiting the angle difference of the Cherenkov photons emitted by particles with the same momentum but different masses [82].

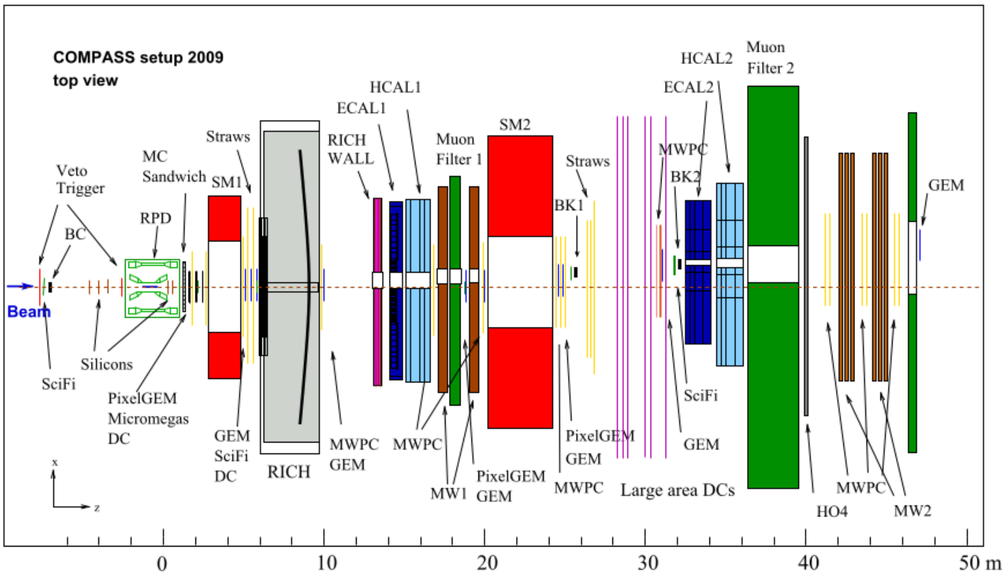

FIGURE 2.2. Scheme of the COMPASS experiment; the target is located inside the RPD station; the input beam characterization stage is located upstream with respect to the target and is not shown here [82].

figure 2.3 left) instrumented with several planes of drift tubes and holed in the center [84].

- Recently, an absorber for the target large output flux [87, 88] and for the non-interacting input beam [88] has been installed upstream with respect to SM1.
- Another iron layer is located at the downstream end of the COMPASS setup – figure 2.3 right.

FIGURE 2.3. *(left)* The second Muon Wall. *(right)* The downstream iron layer.

Only the muons, either from the input muon beam or from the pion decay within the input hadron beam, cross all these absorber layers and are delivered to the experimental areas at the downstream end of the COMPASS site. Since COMPASS exploits the M2 high intensity beams, a high muon yield is achieved. Photos of the downstream experimental areas are shown in figure 2.4. Two areas are available; during the 2018 run the first area has been used by the COMPASS++ experiment, while the second area hosted the MUonE feasibility test.

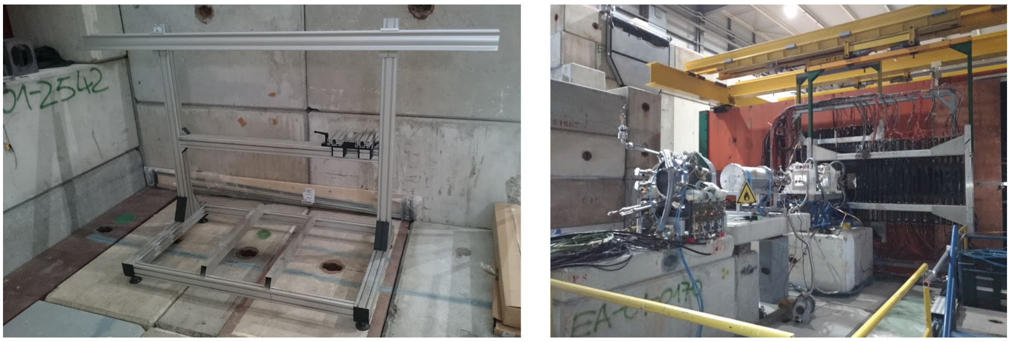

FIGURE 2.4. Experimental areas at the downstream end of the COMPASS site: *(left)* the second area, exploited by the MUonE experiment in 2018; *(right)* the first area, exploited by the COMPASS++ experiment in 2018.

2.2 The MUonE proposal

The MUonE collaboration proposes a novel approach to determine the running of the fine-structure constant $\alpha(t)$ via t-channel data: it exploits the elastic scattering of high-energy muons on the atomic electrons in a low-Z target [24, 80]. As already mentioned in subsection 1.6.3, from the value of $\alpha(t)$ its hadronic contribution $\Delta\alpha_{\text{had}}(t)$ can be extracted and, in turn, a_μ^{HLO} can be evaluated via the sum rule in equation 1.43 [24, 80].
The running of the fine-structure constant can be extracted from the differential cross section for the $\mu^\pm e^-$ elastic scattering (depicted in figure 1.35), which can be written as

$$\frac{d\sigma}{dt} = \frac{d\sigma_0}{dt}\left|\frac{\alpha(t)}{\alpha(0)}\right|^2 \tag{2.1}$$

where $d\sigma_0/dt$ is the effective Born cross section, including virtual and soft photons, which is well known in the SM [24]. The $|\alpha(t)/\alpha(0)|^2$ factor comes from the inclusion of the vacuum polarization effect in the leading photon exchange, i.e. the next-to-leading-order contribution to the scattering process; in order to achieve a higher precision, higher-order radiative corrections (examples of contributing processes in figure 2.5) must be included as well [24] – some details can be found in [89].
Figure 2.6 shows the $\mu^\pm e^-$ elastic scattering in the laboratory frame. The input muon hits an atomic electron within the target transferring part of its energy;

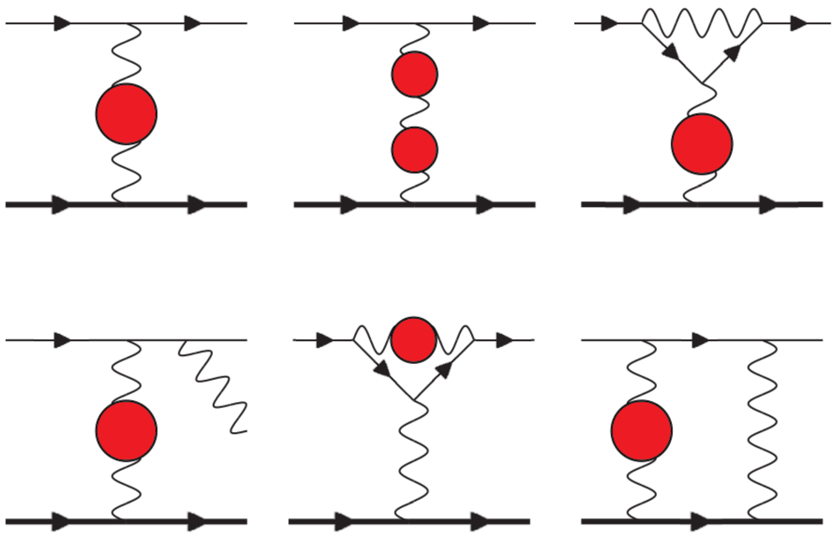

FIGURE 2.5. Examples of higher-order hadronic contributions to the $\mu^{\pm}e^{-}$ scattering; the thin (thick) lines indicate the electrons (muons). Edited from [89].

therefore, the output state features both the scattered muon and the freed electron. The three trajectories are coplanar, i.e. they lie on the same plane.
Special relativity can be used to derive analytic relations between all the kinematical variables in the laboratory frame [24]. Starting from the Mandelstam variables

$$\begin{cases} s = m_e^2c^4 + m_\mu^2c^4 + 2m_ec^2E_\mu^{\mathrm{i}} & \text{(squared center-of-mass energy)} \\ t = 2m_ec^2(E_\mu^{\mathrm{f}} - E_\mu^{\mathrm{i}}) & \text{(squared momentum transfer)} \end{cases} \tag{2.2}$$

and from the Källén (or triangle) function

$$\lambda(s, m_e^2c^4, m_\mu^2c^4) = 4m_e^2c^4\left[(E_\mu^{\mathrm{i}})^2 - m_\mu^2c^4\right] \tag{2.3}$$

and defining

$$r = \frac{\sqrt{(E_\mu^{\mathrm{i}})^2 - m_\mu^2c^4}}{E_\mu^{\mathrm{i}} + m_ec^2} \tag{2.4}$$

the kinematical curves

$$E_e^{\mathrm{f}}(\theta_e) = m_ec^2\frac{1 + r^2\cos^2\theta_e}{1 - r^2\cos^2\theta_e} \tag{2.5}$$

and

$$\theta_\mu(\theta_e) = \arcsin\left\{\frac{\sin\theta_e\sqrt{\left[E_e^{\mathrm{f}}(\theta_e)\right]^2 - m_e^2c^4}}{\sqrt{\left[E_\mu^{\mathrm{i}} + m_ec^2 - E_e^{\mathrm{f}}(\theta_e)\right]^2 - m_\mu^2c^4}}\right\} \tag{2.6}$$

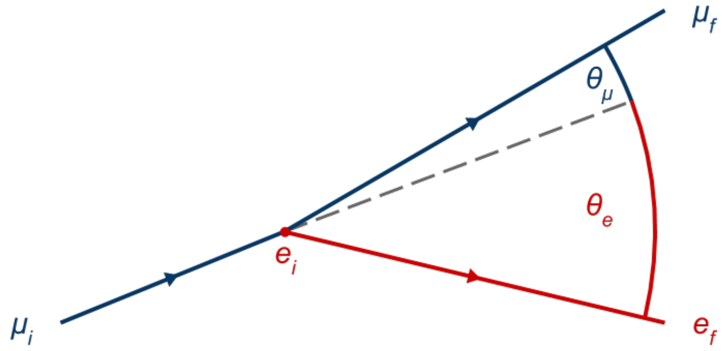

FIGURE 2.6. $\mu^{\pm}e^{-}$ elastic scattering in the laboratory frame.

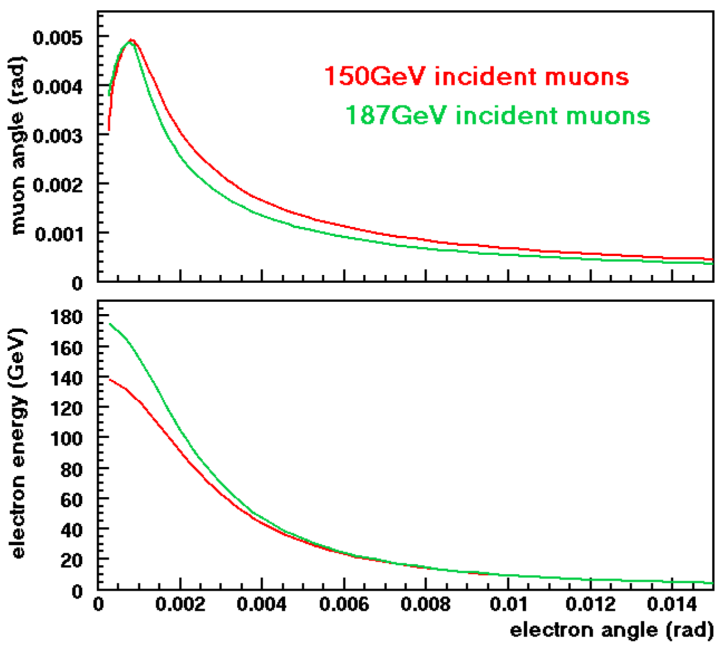

FIGURE 2.7. $\mu^{\pm}e^{-}$ elastic scattering kinematic curves: *(top)* $\theta_\mu(\theta_e)$; *(bottom)* $E_e^{\mathrm{f}}(\theta_e)$.

can be calculated; equations 2.5 and 2.6 relate the electron output energy and the muon scattering angle with the electron scattering angle [90].
Figure 2.7 shows the two kinematic curves $\theta_\mu(\theta_e)$ and $E_e^{\mathrm{f}}(\theta_e)$. The lepton mass values reported in table 1.1 have been used, along with input muon energy values of 150 GeV and 187 GeV; the first value was used in early simulations [24, 91] and corresponds to the final experimental condition [80] while the second value was used in the 2018 feasibility test. The $\theta_\mu(\theta_e)$ plot (figure 2.7 top) shows that increasing the input muon energy moves the curve towards lower muon angle values: this represents an issue, since the region $\theta_\mu \lesssim 0.5$ mrad should be contaminated by background events [91].
The background events with small muon angle and practically random electron angle emerge from several processes that result from the interaction between the input high-energy muons and the matter along the line and can compete with the elastic events [91]:

- δ-ray emission (see subsection 2.3.1);
- electron-positron pair production, after which one of the three output particles escapes from the detector acceptance;
- Bremsstrahlung, in which the output photon is mistaken for an electron or produces a electron-positron pair.

Along with these effects, another contribution to this kind of background is given by the electron Multiple Coulomb Scattering (MCS) in the low E_e^{f} region, which breaks the $\mu^\pm e^-$ two-body angular correlation [24, 91]. Inelastic collisions with the target nuclei are also possible [91].
It can be shown via these kinematic relations that, for $E_\mu^{\mathrm{i}} = 150$ GeV and E_e^{f} $\in (1, 139.8)$ GeV (in which the lower boundary is arbitrary and the upper boundary corresponds to the zero θ_e case), $t(x) \in (-0.143, 0)$ GeV^2, i.e. $x \in (0, 0.93)$; therefore, this process allows to evaluate equation 1.43 around the integrand peak, which is at $x = 0.914$ (as can be seen in figure 1.34 right) [24].
Furthermore, equations 2.5 and 2.6 show that the $\mu^\pm e^-$ elastic scattering experiences the relativistic boost along the input muon trajectory: this makes the full coverage of the process acceptance achievable with a detector with small transverse dimensions [24].

2.2.1 Experimental layout and possible locations

Figure 2.8 shows the concept of the MUonE setup. It is a modular system: each module consists of a thick, low-Z target and two double-vista tracking modules [24]. Preliminary simulations performed on an apparatus with 20 modules at a relative distance of ~ 1 m from each other and spaced by air gave promising results: in particular, they pointed out that a single detector element would be able to measure both the electron and muon scattering angles [24].

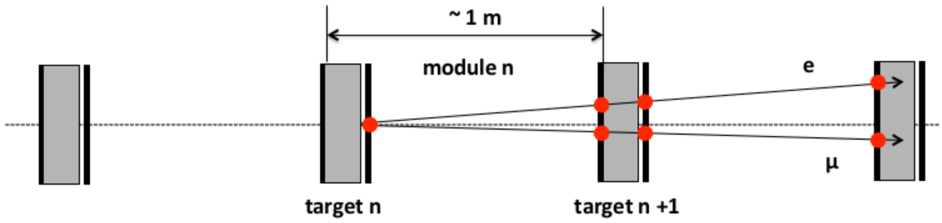

FIGURE 2.8. Concept of the MUonE final setup; the input beam enters the detector from the left; the thick black lines represent the tracking modules [24].

As already mentioned, the target has to be made of a low-Z material in order to minimize the MCS and the pair production and Bremsstrahlung contributions to the background; furthermore, the target has to be thick enough in order to collect sufficient statistics [24]. 3 cm thick beryllium or graphite targets would meet the experiment needs [24].
Silicon microstrip sensors would be an excellent choice for the tracking planes in the configuration depicted in figure 2.8: early simulations pointed out that such a tracking system would need an angular resolution of ~ 0.02 mrad to achieve a sufficiently high signal-to-noise discrimination power in the (θ_e, θ_μ) phase-space [24]. As already stated, the limited transverse coverage of the silicon sensors does not represent an issue: thanks to the relativistic boost, $\sim 10 \times 10$ cm^2 tracking planes would allow to cover most of the process acceptance.
For $\theta_e \in (2, 3)$ mrad the output electron and muon have approximately the same scattering angle [24]. Such an ambiguity makes the two particles indistinguishable via tracking thus requiring a particle identification system; the use of electromagnetic calorimeters and muon filters is currently under study [24]. A system of dipoles between each pair of successive modules for the momentum measurement has been proposed as well [92].
Both the MUonE experiment and the COMPASS++ experiment[2] would like to exploit the M2 beamline within the COMPASS site from the beginning of Run 3 in 2021; the compatibility between the two experiments requirements has been and is being carefully studied – details can be found in [80].
Two position options are currently under study: the first consists of installing the MUonE setup downstream with respect to the COMPASS spectrometer while the second consists of exploiting a possible available space within the last part of the M2 beamline tunnel [80]. The second option (shown in figure 2.9) seems promising, since it would guarantee the possibility of installing MUonE and COMPASS++ together without any space interference [80].

[2] COMPASS++ addresses many outstanding topics such as the proton radius puzzle, the quark structure of the light mesons, the kaon polarizabilities and the kaon spectroscopy [80]. The proton radius measurement is based on the study of the muon-proton elastic scattering with a TPC [80].

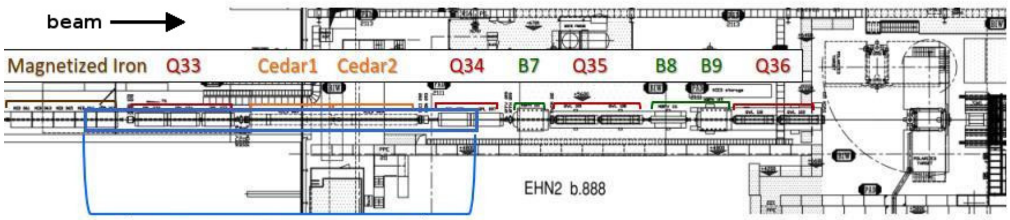

FIGURE 2.9. Possible MUonE setup final location within the last part of the M2 beamline tunnel; the COMPASS target is located at the right end; the available space is highlighted in blue [80].

2.2.2 Accuracy goal and statistics collection

The final goal of MUonE is the determination of the differential cross section in equation 2.1 with ~ 10 ppm systematic uncertainty at the peak of the integrand of equation 1.43, which corresponds to an uncertainty of $\sim 0.3\%$ on $a_\mu^{\rm HLO}$ [24, 93]. Such a good accuracy can be achieved only with a fine control on the measurement efficiency in both

- the signal region, i.e. the region of the kinematical phase-space with small electron angles (and thus high electron energy) [24];
- the normalization region, i.e. the region in which $E_e^{\rm f} \sim 1$ GeV (corresponding to larger electron angles) [24].

The regions boundaries are defined keeping the setup acceptance limits into account; once the relative efficiencies are known, the elastic scattering cross section can be studied starting from the ratio between the elastic event counts in the two regions, which makes many systematic errors, such as the one that is related to the beam luminosity, cancel out [24].

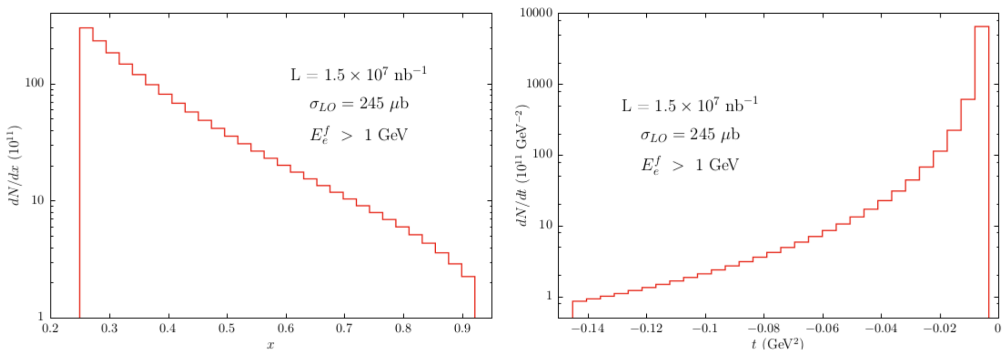

FIGURE 2.10. Distribution of the $\mu^\pm e^-$ scattering events as a function of x *(left)* and t *(right)* [24]; the normalization is described in the text.

The distributions of the scattering events as a function of x and t are shown in figure 2.10. These plots have been obtained with the likely assumptions that

$E^{\mathrm{i}}_{\mu} = 150$ GeV, that the average input intensity is 1.3×10^7 Hz and that the setup described in subsection 2.2.1 takes data for 2 years with a running time of 2×10^7 s/yr, which result in an integrated luminosity of 1.5×10^7 nb^{-1}, and with the leading-order elastic cross section for $E^{\mathrm{f}}_{e} > 1$ GeV, $\sigma^{\mathrm{elastic}}_{\mathrm{LO}} = 245$ μb [24, 93].
From the theoretical point of view, the control of the systematic uncertainties down to ~ 10 ppm requires the evaluation of higher-order radiative corrections, partially still unexplored in the $\mu^{\pm}e^{-}$ scattering case, and the development of high-precision simulations which take the former into account [24].

2.3 The 2018 feasibility test

Preliminary tests with one or two detector modules are crucial to identify the best hardware configuration and to understand how the features of each component affect the system performance in terms of sensitivity and accuracy. During the CERN 2018 run, the MUonE experiment performed a feasibility test in the COMPASS site, downstream with respect to the COMPASS apparatus; the test lasted from April 1$^{\mathrm{st}}$ to November 12$^{\mathrm{th}}$.
The setup is depicted in figure 2.11 and a photo is shown in figure 2.12. It features 16 silicon microstrip layers, 2 carbon targets and an electromagnetic calorimeter. A detailed description of each detector component will be given in the following subsections.
Figure 2.13 shows the timeline of the test; several modifications and upgrades on the tracking system, the calorimeter and the targets have been performed during the ~ 7.5 month long run – details will be given in subsection 2.3.8. Between May 23$^{\mathrm{rd}}$ and June 8$^{\mathrm{th}}$ the system ran without the electromagnetic calorimeter. Two major shutdown sessions took place, between July 12$^{\mathrm{th}}$ and August 21$^{\mathrm{st}}$ and between September 18$^{\mathrm{th}}$ and 26$^{\mathrm{th}}$, because many components of the tracking system, including detectors and elements of the readout chain, were temporarily unavailable.

2.3.1 The silicon microstrip sensors

The tracking modules were developed by the INSULAb group. Each module features 2 silicon microstrip layers with different strip direction. The chosen reference system is shown in figure 2.14. The x (y) axis is parallel (orthogonal) to the floor plane. Three 45° stereo layers have been implemented in order to have a sensitivity in the u and v directions and perform double hit disambiguation (subsection 2.3.3).
The tracking system active elements are the AGILE silicon sensors. The AGILE sensors are $9.5 \times 9.5 \times 0.041$ cm^3 single-sided silicon microstrip tiles manufactured by Hamamatsu on high resistivity substrates [94–96]. Such a large size, obtained using 6″ silicon wafers [96], meets the needs of the MUonE tracking

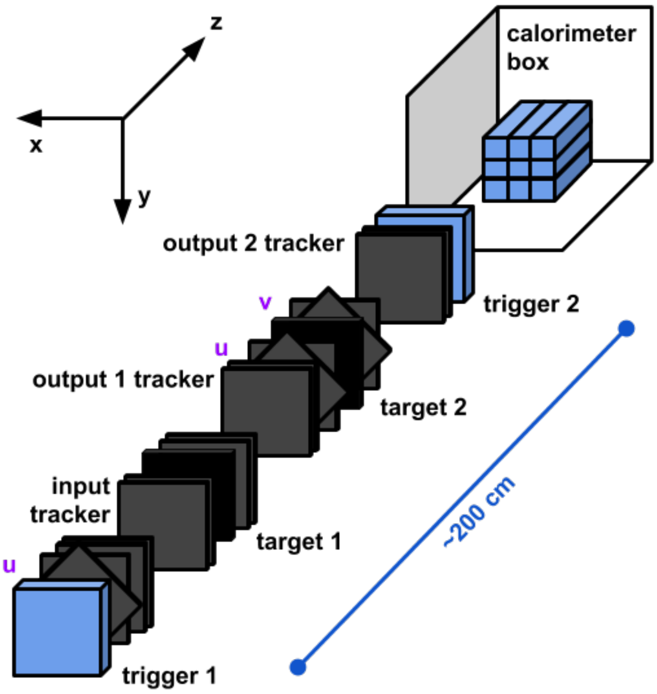

FIGURE 2.11. Scheme of the first configuration of the MUonE 2018 feasibility test setup.

FIGURE 2.12. The MUonE feasibility test setup.

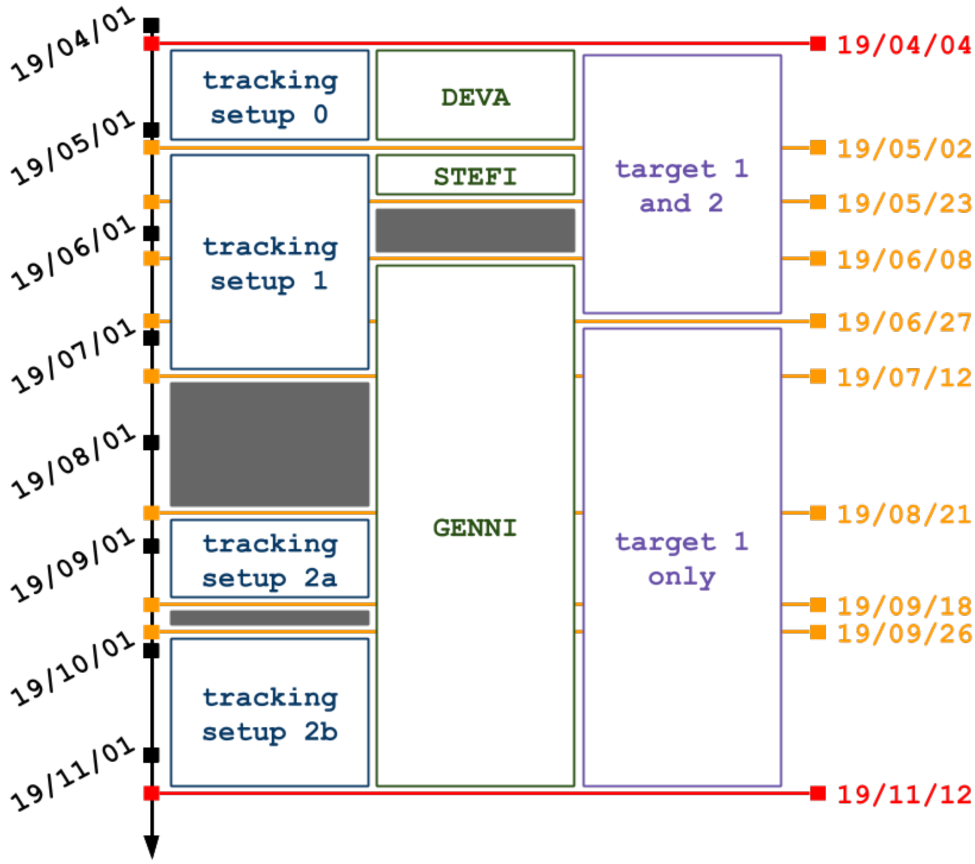

FIGURE 2.13. Timeline of the MUonE feasibility test; different stages of the tracking system, of the calorimeter and of the targets are shown in the first, second and third column respectively; gray boxes indicate inactivity periods.

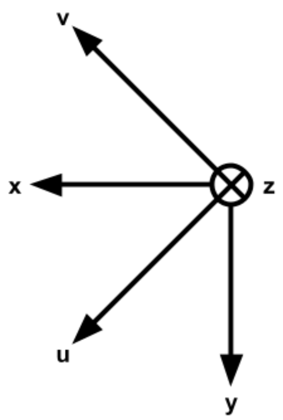

FIGURE 2.14. Tracking planes reference system; the beam enters the page; the x axis points towards Northwest.

system already discussed in subsection 2.2.1. Details on the charge production and collection in these sensors can be found in [96].
The strips have a 121 μm physical pitch [94–96]. The floating strip scheme is used for the readout, i.e. only one strip every two is read out: since the interstrip capacitance, implemented by properly tuning the dimensions of both the aluminum layer and the implant in the sensor design phase [97], allows the charge to be shared between adjacent strips, this configuration guarantees the same spatial resolution as if all the strips were read out while halving the number of readout channels and thus reducing the power consumption and the data size [94–96]. The readout pitch is therefore 242 μm and the active area is 9.2928×9.2928 cm^2 with 384 channels [94–96]. Furthermore, the analog readout allows to reconstruct the hit position on the sensor by means of the Center Of Gravity[3] [96].
The spatial resolution of the AGILE sensors has been extensively studied [94, 96, 98]. As already mentioned, the floating strip scheme improves the resolution, which can be evaluated as [99]

$$\sigma_{\text{res}} \sim \frac{w_{\text{phys}}}{\sqrt{12}} \sim 35 \ \mu\text{m} \tag{2.7}$$

where $w_{\text{phys}} = 121$ μm is the physical pitch.
The 410 μm thickness, which corresponds to $\sim 0.004376 X_0$, contributes non-negligibly to the MCS: for an incoming particle with velocity β and momentum p this contribution can be evaluated as [2, 96]

$$\Delta\theta = \frac{13.6 \text{ MeV}}{\beta pc} z \sqrt{\frac{d}{X_0}} \left[1 + 0.038 \cdot \ln\left(\frac{d}{X_0}\right)\right] \tag{2.8}$$

where z is the particle charge normalized to the electron charge; it has to be noted that $\Delta\theta$ is independent on the particle mass and that for ultrarelativistic particles $\beta \sim 1$ and $pc \sim E$ where E is the incoming particle energy. For the AGILE sensors equation 2.8 leads to $\Delta\theta = 0.71397 \text{ MeV}/\beta pc$.
If an incoming particle transfers a huge amount of kinetic energy to a single electron in the silicon, the latter can be emitted as a so-called δ-ray [96]. The probability of this effect decreases as the kinetic energy increases, but high-energy δ-rays have a large range: a 1 MeV electron travels 1 mm inside a silicon layer and can cause a COG shift of up to ~ 355 μm (~ 1.5 the readout pitch) [96]. Such an emission is not unlikely: a $\sim 0.4\%$ probability has been evaluated [96]. Furthermore, high-energy δ-rays can be knocked off the silicon layer and freely propagate: as already mentioned (section 2.2), this represents a major background source in the MUonE case; as discussed in section 4.6, dedicated criteria to exclude δ-rays in the 2018 data have been studied.
As shown in figure 2.15, the sensors are assembled on 3 or 5 mm thick fiberglass supports together with the ASICs Printed Circuit Board (PCB – figure 2.16 left).

[3] The COG corresponds to the hit position on the sensor, computed as the average of the strip center positions weighted with their signals [96] – details on the hit point reconstruction will be given in subsection 3.3.2.

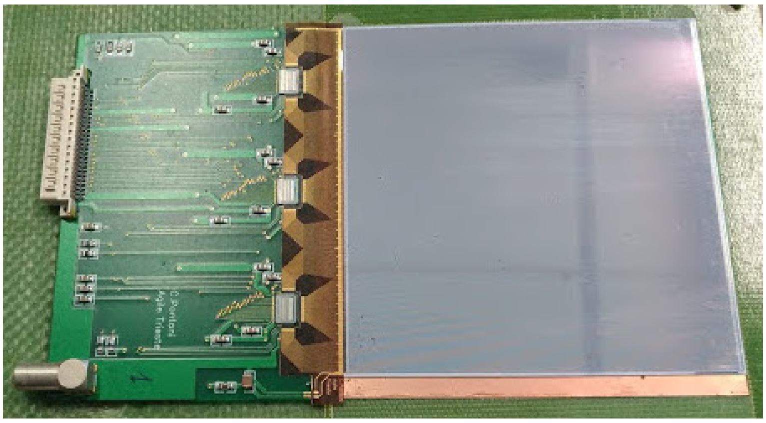

FIGURE 2.15. An AGILE silicon microstrip layer coupled to the ASICs PCB and assembled on the fiberglass support.

The strips are connected via 17 µm aluminum wire-bonds (figure 2.16 right) to a pitch adapter, i.e. a circuit that adapts the sensor readout pitch (242 µm) to the ASIC channels pitch (100 µm) [96]. Each sensor is read out by three 128-channel, low-noise, analog-digital ASICs[4]. The readout of the differential analog output is multiplexed, with a maximum clock frequency of 10 MHz [95, 96]. Typical beamtest clock values are 5 MHz or 2.5 MHz; the latter has been used in the MUonE run.

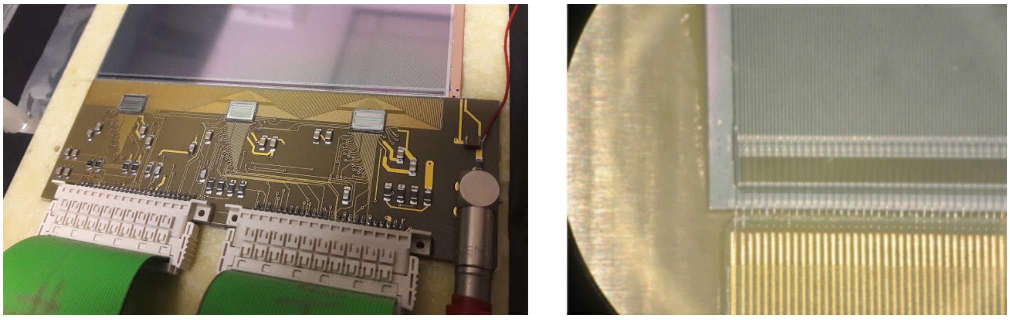

FIGURE 2.16. *(left)* ASICs PCB. *(right)* Detail of the wire-bonding between the sensor and the pitch adapter.

Each tracking module of the MUonE apparatus features two different-view planes like the one shown in figure 2.15. The only exception is represented by the $(15y, 16x)$ module, which features the same sensors and ASICs but in a different configuration: in this case a tray of the Minitracker, a small AGILE tracker prototype, has been used. A Minitracker tray consists of a pair of silicon sensors arranged in a xy configuration and assembled at the opposite sides of a $\sim 20 \times 20$ cm^2, ~ 1.3 cm thick support made of aluminum honeycomb sheets

[4]TA1 or TAA1 – the features can be found in [96, 100, 101].

and carbon fiber which contains a 99.95% pure, 245 µm ($\sim 0.0684931 X_0$) thick tungsten converter [95, 96]. Details on the AGILE tracker can be found in [94–96, 102]. The $(15y, 16x)$ module has been placed downstream with respect to the other tracking planes in order to minimize the MCS contribution of the tungsten to the pattern reconstruction precision.
Each pair of different-view planes is assembled (figure 2.17 left) in a $\sim 50 \times 25 \times 4.2$ cm^2 aluminum box (figure 2.17 right), with the active areas aligned to the $\sim 9.6 \times 9.6$ cm^2 apertures in the aluminum walls; black cardboard and tinfoil layers are interleaved between the apertures and the sensors (figure 2.17 right) in order to protect the sensors from the external light and electromagnetic noise. A couple of ERNI cables connects each ASICs PCB to its repeater, i.e. the first element of the readout electronic chain, which is assembled on the outer side of the aluminum box. Details on the readout chain will be given in subsection 2.3.7.

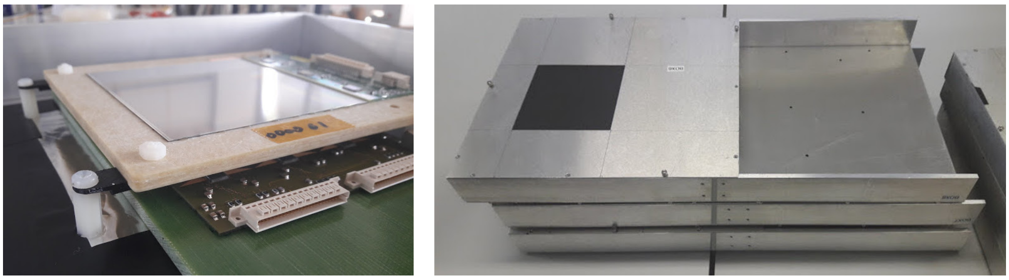

FIGURE 2.17. *(left)* Two silicon sensors assembled in their aluminum box. *(right)* The aluminum boxes; the closed half (left side) hosts the silicon detectors while the open half (right side) hosts the readout electronic boards.

2.3.2 The tracking system

Figure 2.18 shows a scheme of the MUonE tracking setup 1 (top) and 2 (bottom) with all the strip orientations (figure 2.14) and positions along the beam direction z in the reference system that originates in the $1u$ layer (in the first configuration). The whole system is ~ 2 m long.
In setup 1, the tracking system is composed of three stations:

- the input station, which features 6 planes in 52.1 cm;
- the upstream target output station, which features 6 planes (although the $10x$ malfunctioning layer has been excluded in the analysis – subsection 2.3.8) in 56.5 cm;
- the downstream target output station, which features 4 planes in 50.56 cm.

Each station has a stereo plane. Once the downstream target was removed, the second and third stations were merged into a 127.2 cm long output station with 10 tracking planes.
After the upgrade to setup 2 (see subsection 2.3.8) the tracking system featured:

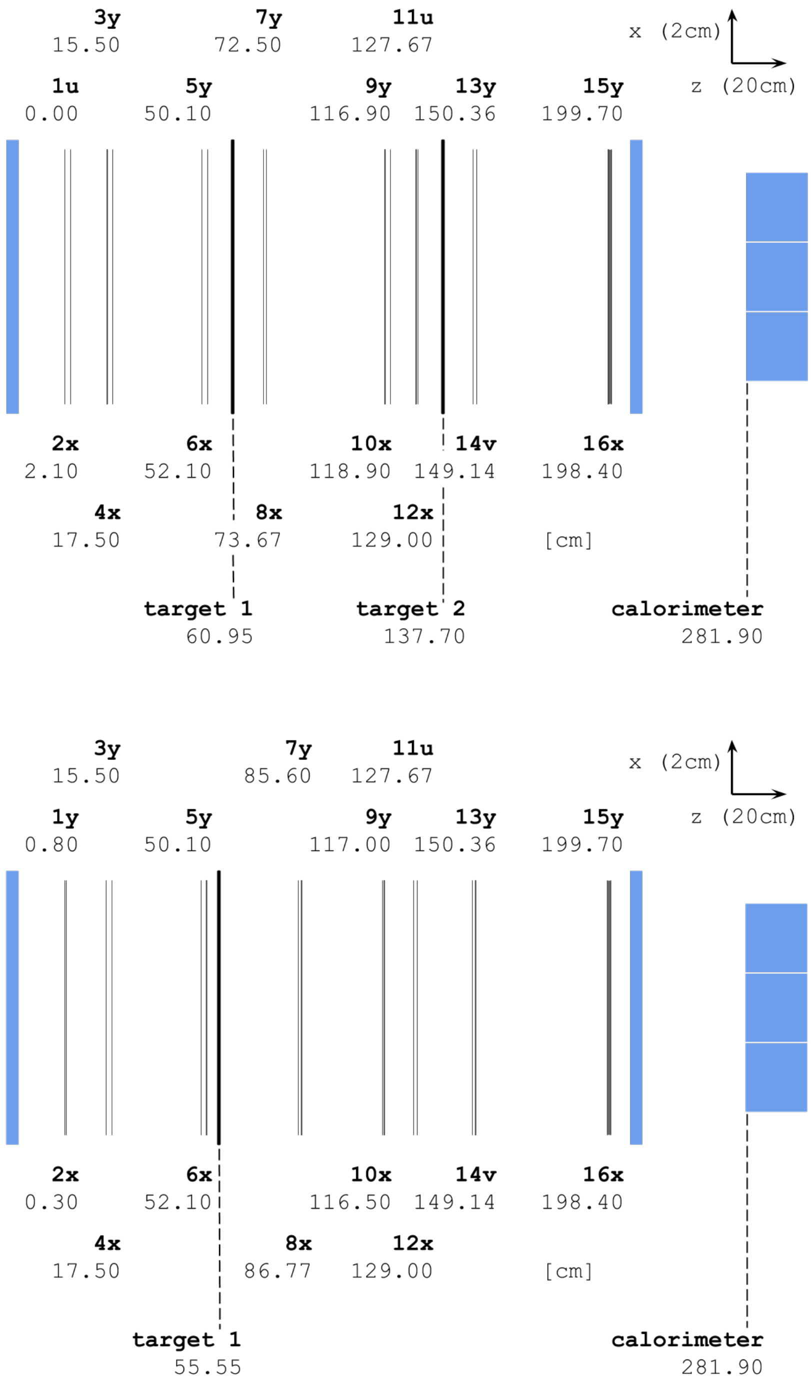

FIGURE 2.18. On-scale scheme of the MUonE tracking system in setup 1 *(top)* and 2 *(bottom)*. The unmarked light blue boxes represent the 4.5 cm thick trigger counters (subsection 2.3.6). The z positions refer to the upper edge of the detectors.

- a 51.8 cm long input station with 6 xy planes and no stereo planes;
- a 114.1 cm long output station with 10 planes (2 stereo).

2.3.3 Stereo layers

Tracking planes measuring single coordinates do not provide 2D hit points but only a 1D projection [103]. Therefore, if multiple particles cross a pair of orthogonal (xy) microstrip sensors at the same time, ghosts arise and make the hit point reconstruction ambiguous [104]. In general, a ghost is defined as a hit point reconstructed by the tracking algorithm that does not correspond to any particle [103].
An example of this effect is shown in figure 2.19: in the single-hit case the position reconstruction is unambiguous, while in the double-hit case 4 hit points are reconstructed, 2 of them being the true crossing points and the other 2 being ghosts. In general, if N particles cross the tracking module at the same time, $N(N-1)$ ghosts arise [104].
In double-side sensors the correlation between the charge collected at the opposite edges can be exploited as a tool for disambiguation [104]. On the other hand, in single-side sensor pairs there is no way to identify ghosts without using some external information. Stereo planes represent a tool for ghost identification: as shown in figure 2.20, the information on the hit positions along a third reference axis coplanar with x and y allows the disambiguation of physical hit points and ghosts.
As already mentioned, the MUonE tracking system features three 45° stereo layers. These layers have been assembled on dedicated custom fiberglass supports (figure 2.21).

2.3.4 The carbon targets

The apparatus features two $\sim 10 \times 10$ cm^2 8 mm thick graphite layers. As shown in figure 2.22, the targets are installed on a custom plastic holder which is coupled to the Newport rail via a Bosch mechanical support.
When upgrading the tracking system to setup 2, the output lever arm was increased and hence the minimum distance needed for double hit disambiguation in the first output module was reduced. The second target was removed ~ 3 months after the run start; the focus of the test was therefore moved to the study of a single module with a longer lever arm.

2.3.5 Calorimeters

Three different electromagnetic calorimeters (second column in figure 2.13) have been used during the run: a sampling and two homogeneous ($PbWO_4$ and BGO – the main features are compared in [2]) scintillating detectors.

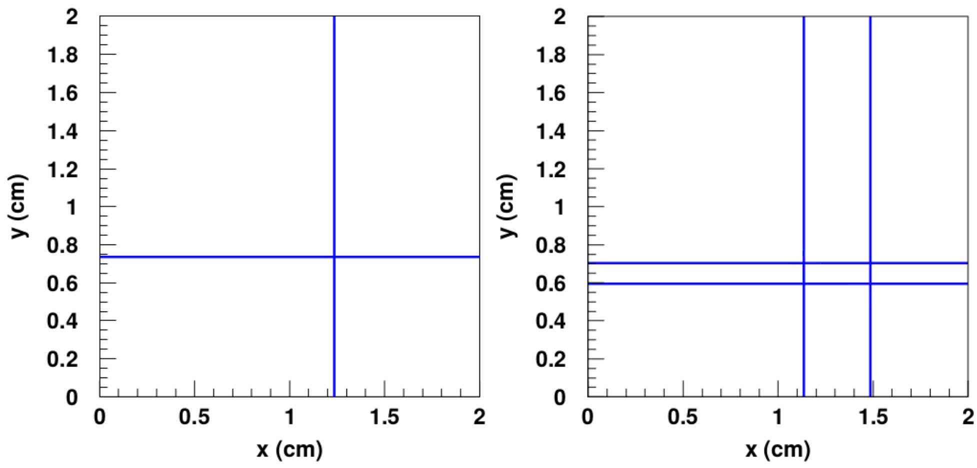

FIGURE 2.19. Examples of single- *(left)* and double-hit *(right)* events reconstructed by a double-sided, $\sim 2 \times 2$ cm^2 silicon microstrip sensor – edited from [104].

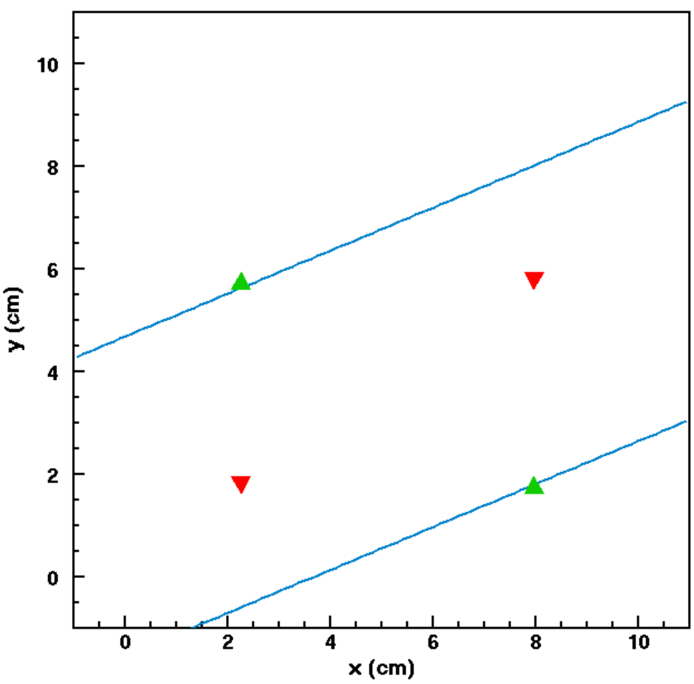

FIGURE 2.20. Example of physical hit points (green) and ghosts (red) disambiguation via a stereo layer.

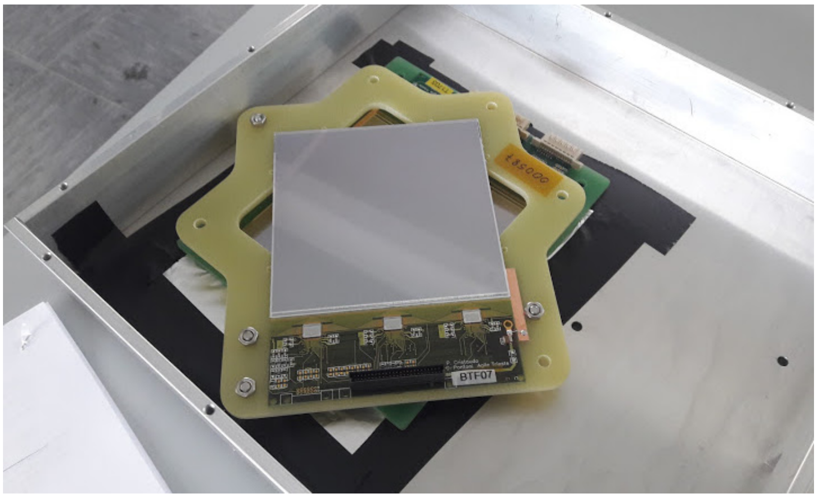

FIGURE 2.21. Stereo layer assembled on its fiberglass support and in its aluminum box.

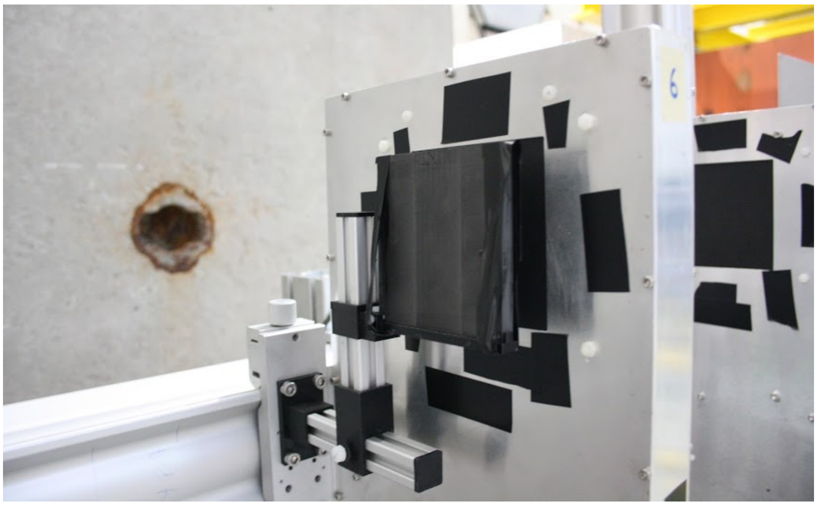

FIGURE 2.22. Upstream target.

2.3.5.1 DEVA – the sampling detector

During the first month the calorimeter was DEVA, a sampling calorimeter composed of 12 $15 \times 15 \times 2$ cm^3 plastic scintillator layers interleaved with 11 lead tiles (the upstream eight 0.5 cm thick and the remaining three 1 cm thick) and coupled via WaveLength Shifter (WLS) optical fibers to a Hamamatsu R5600-M16 Multi-Anode PhotoMultiplier Tube (MAPMT) [105].
Details on the performance and on the typical use of DEVA can be found in [105]. This detector was developed by the INSULAb group for the CERN North Area high-energy (tens to hundreds of GeV) electron and hadron beams and did not meet the MUonE needs for the measurement of the few-GeV electron energy and of the Minimum Ionizing Particle (MIP) peak.

2.3.5.2 STEFI – the $PbWO_4$ detector

The STEFI (scheme in figure 2.23) active volume consists of a 3×3 matrix of $PbWO_4$ crystals, spare pieces of the CMS endcap calorimeter [106]. The CMS $PbWO_4$ crystals have been extensively tested [107].

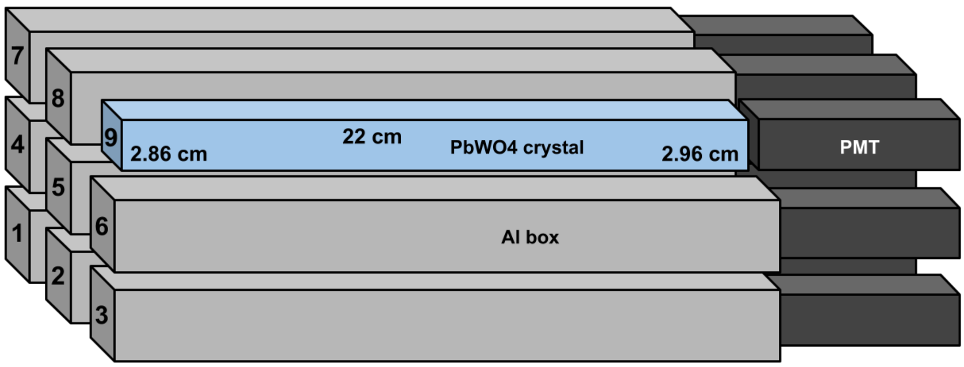

Figure 2.23. Scheme of STEFI.

Each crystal is contained in a custom aluminum box with a plastic plug for the coupling to the photodetector; the whole matrix is held together by a Bosch structure and is contained in a ~ 50 cm long aluminum box (photo in figure 2.24 left). A photo of one of the crystals out of its aluminum box is shown in figure 2.24 right. It is trapezoidal, with a front section of 2.86×2.86 cm^2, a rear section of 2.96×2.96 cm^2 and a length of 22 cm, which corresponds to $\sim 24.7X_0$. It is wrapped in a Tyvek sheet to increase the light yield [106].
STEFI was developed by the INSULAb group as a high-energy γ-calorimeter with a SiPM-based readout system [106]. This configuration was optimized for $\gtrsim 100$ GeV photons and required major modifications in order to meet the MUonE feasibility test needs.
The photodetectors have been completely replaced with Hamamatsu H6780-03 PMTs [108], whose sensitivity peak wavelength perfectly matches those of the

$PbWO_4$ emission peak.
Figures 2.23 and 2.24 clearly show that there is a few-mm gap between the different channels active areas due to the mechanical structure: these dead regions inside the active volume cause an energy loss and thus negatively affect the detector energy resolution. The results of the performance of STEFI will be given in section 3.5.

2.3.5.3 GENNI – the BGO detector

GENNI (figures 2.25 and 2.26) is a 3×3 matrix of BGO crystals, spare pieces of the PADME calorimeter. The PADME crystals have been obtained by cutting the bigger crystals of the L3 endcap calorimeter and have an approximate dimension of $2.1 \times 2.1 \times 23$ cm^3 [109, 110]. Each crystal is coupled to a Photonis XP1912 PMT [111] biased at 850 V.
It is evident from figures 2.25 and 2.26 that such a compact structure allows to minimize the dead regions in the active volume to the $\lesssim 1$ mm irreducible gaps created by the white painting. As it will be shown in section 3.5, this configuration allows to achieve an excellent energy resolution.

2.3.6 The trigger system and the scalers

The trigger signal is generated by the trigger board starting from the beginning-of-spill and the end-of-spill signals, which come from the SPS, and the coincidence of the signals of two scintillating counters placed upstream (S1) and downstream (S2) with respect to the MUonE tracking system. Each counter (figure 2.27) consists of a $\sim 10 \times 10 \times 4$ cm^3 plastic scintillator layer coupled to a PMT.
The trigger rates per spill of S1, S2 and their coincidence are measured by the scalers implemented in the trigger board and written in dedicated log files. During the commissioning phase, 20 bit scalers were used, therefore the measured trigger rate was capped at $2^{20} - 1 = 1048575$ counts per spill, which was not enough for the expected intensity (see section 2.1). The scalers were thus upgraded to 24 bit ones.

2.3.7 The DAQ system

The high-performance INSULAb readout electronic chain (figure 2.28), whose detailed description is given in [97], has been used for the MUonE tracking detectors. The first element of the chain is the repeater, a PCB that [97]

- amplifies the ASICs multiplexed analog output.
- allows to configure the ASICs.
- provides the bias to the sensor and the power to the ASICs.

Each tracking module features two repeaters. The repeaters are coupled to an ADC board for the digitalization of the multiplexed analog signal [97]. Both the

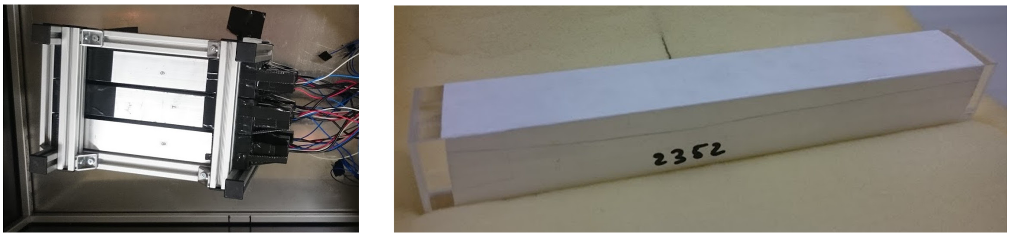

FIGURE 2.24. *(left)* STEFI on its mechanical support installed in the aluminum box. *(right)* A CMS endcap calorimeter crystal.

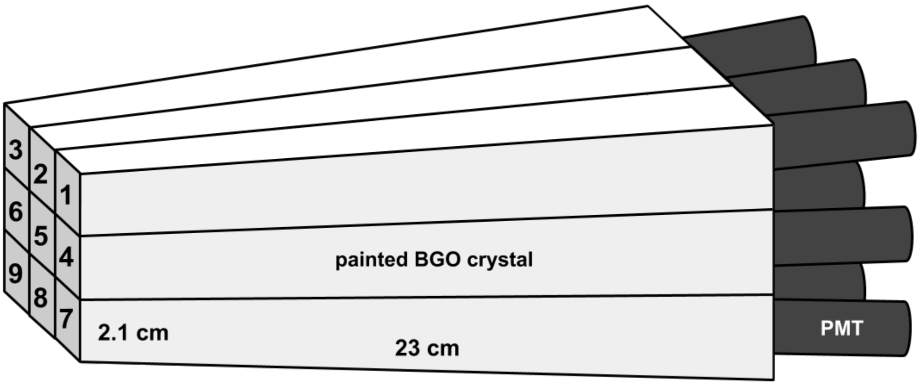

FIGURE 2.25. Scheme of GENNI.

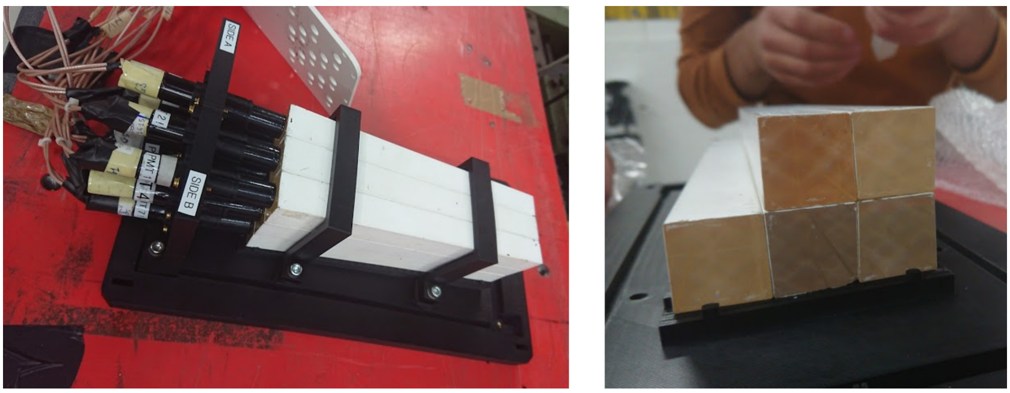

FIGURE 2.26. GENNI in its mechanical support *(left)* and during the assembly *(right)*.

FIGURE 2.27. Upstream scintillating counter.

repeaters and the ADC board are assembled on the outer side of the tracking module box (figure 2.29).
The last part of the chain is housed in a VME crate (figure 2.30 left). The communication between the crate and the repeater and ADC boards is performed via ~ 5 m long $16+16$ I/O LVDS lines. The VME crate hosts 8 VRBs (VME Readout Boards – one per tracking module), whose main tasks are [97]

- the readout of the ADC output data during the spill, their storage in a dedicated RAM and their transfer to the DAQ PC during the interspill period;
- the generation of the hold for the strip signal sampling (whose details are given in [96]) and the clock for the multiplexing (subsection 2.3.1);
- the management of the ASIC and ADC configuration parameters, such as the threshold for the zero suppression.

The trigger is generated and delivered to the VRBs by a trigger board [97] (subsection 2.3.6). The DAQ is controlled by a SBS Bit3 620 board [112] connected to the DAQ PC via optical fiber [97].
The tracking system can be read out in both normal and zero suppression mode:

- when in normal mode, the ADCs output is de-multiplexed and all the $384 \times N_{layer}$ channels data (6144 strip signals per event in the MUonE configuration) are stored in the RAM; the number of events per spill is limited to 4096 [97].
- When in zero suppression mode, only the strips with a over threshold signal are stored in the RAM; the maximum number of strips that can be stored per layer per event is limited to 16 due to the hardware configuration; the number of events per spill is limited to 65536 [97].

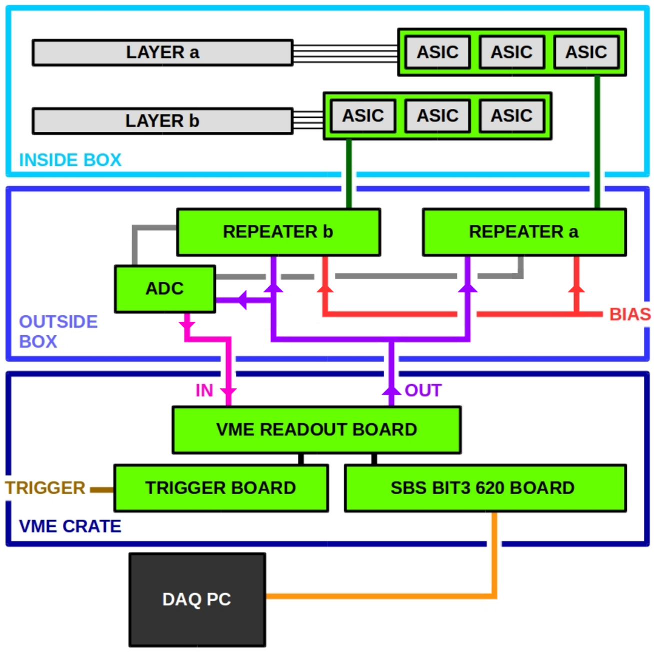

FIGURE 2.28. Scheme of the tracking detectors electronic chain.

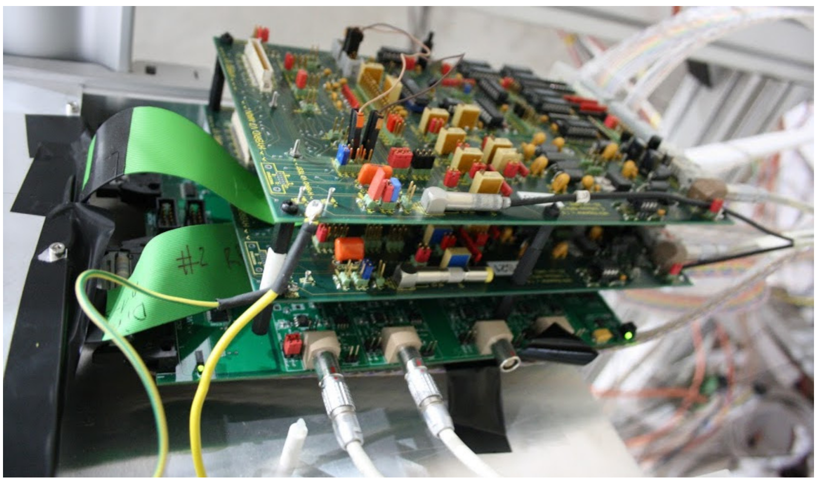

FIGURE 2.29. Tracking detectors electronic chain assembled on the module box: repeaters (above) and ADC board (below).

FIGURE 2.30. *(left)* VME crate with the VRBs, the trigger board and the SBS Bit3 620 board, the power supplies, the DAQ PC. *(right)* VME crate with the digitizers.

The MUonE system runs in zero suppression mode; on the other hand, the normal mode has been extensively used during the first period of data taking in order to study the system behaviour in detail.
The calorimeter is read out by two 8-channel, 12 bit, 250 MS/s, 2 V_{PP} range CAEN V1720 waveform digitizers (figure 2.30 right) [113]. In general, this readout has enough range to measure both the muon MIP peak and the elastic electron energy. However, high-energy ($\gtrsim$ 20 GeV) electrons make the channels saturate. Details on these events and on their kinematics analysis will be discussed in subsection 4.7.3.
A conservative estimate of the acquisition rate is given by [114]

$$R_{\mathrm{DAQ}} = \left(\frac{400}{f_{\mathrm{clk}}\ [\mathrm{MHz}]} + 20\ \mu\mathrm{s} \cdot N_{\mathrm{VRB}} + 10\ \mu\mathrm{s} \cdot N_{\mathrm{digi}} + 800\ \mu\mathrm{s} \right)^{-1} \tag{2.9}$$

where:

- the first term is an incompressible shift time; f_{clk} is the clock frequency;
- the second and third terms are the VRBs and digitizers initialization times;
- the fourth term is the digitizer data readout time.

For the MUonE configuration, equation 2.9 results in a $\sim$ 900 Hz rate; therefore, with an extraction time of 4.8 s [84], $\sim$ 4300 particles per spill are expected. On average, the actual acquisition rate matches this prediction, as shown in section 3.1.
The DAQ is controlled via a Tcl/Tk interface. A remote control system has been implemented: the DAQ PC can be accessed through a VNC server, and thus the DAQ and the power supply interfaces (subsection 2.3.7.1) can be controlled remotely.

2.3.7.1 Slow control

The MUonE system needs several power supplies:

- an Agilent E3647A [115] for the silicon detectors 40 V bias;
- an Agilent E3631A [116] for the STEFI PMTs power and control voltages (in setup 1);
- three TTi PL330DP [117] and QL355TP [118] for the tracking system ± 5 V and ± 7.5 V levels;
- a CAEN DT5533E [119] for the high voltage.

A remote control system has been implemented in order to configure all the voltage levels via the DAQ PC. In particular:

- the DT5533 is controlled via Ethernet and has its own GUI (CAEN GECO2020 [120]).
- The Agilent and TTi devices are controlled via GPIB with a Tcl/Tk inferface.

2.3.8 Hardware upgrades

As already mentioned, many components of the setup were moved or replaced during the run. Many major upgrades were performed at the end of the commissioning phase, the most relevant being the increase of the number of tracking planes from 14 (tracking setup 0) to 16 via the installation of the $(1u, 2x)$ module. The following hardware modifications are represented in figure 2.31:

- the upstream target was moved and the downstream target was removed, in order to turn the double-module setup into a single-module setup with a longer lever arm (subsection 2.3.4).
- As already described in subsection 2.3.5, three different electromagnetic calorimeters were employed.
- The tracking system was upgraded; in particular, the modules that included the $1u$ and $10x$ malfunctioning layers were replaced.

The beam profile reconstructed by the $1u$ layer as a function of the strip number is shown in figure 2.32: almost no hit points are detected by the strips in the $(256, 384)$ range, i.e. by the strips read out by the third ASIC. Since $1u$ is a stereo plane, this malfunctioning results in a $\sim 29.9\%$ reduction of the tracking station active area. The $(1u, 2x)$ module was replaced with a xy one.
On the other hand, layer $10x$ presents many large inefficient or dead regions in the whole active area. Figure 2.33 shows a comparison between the hit point distributions reconstructed by the $(7y, 8x)$ and $(9y, 10x)$ modules during the first

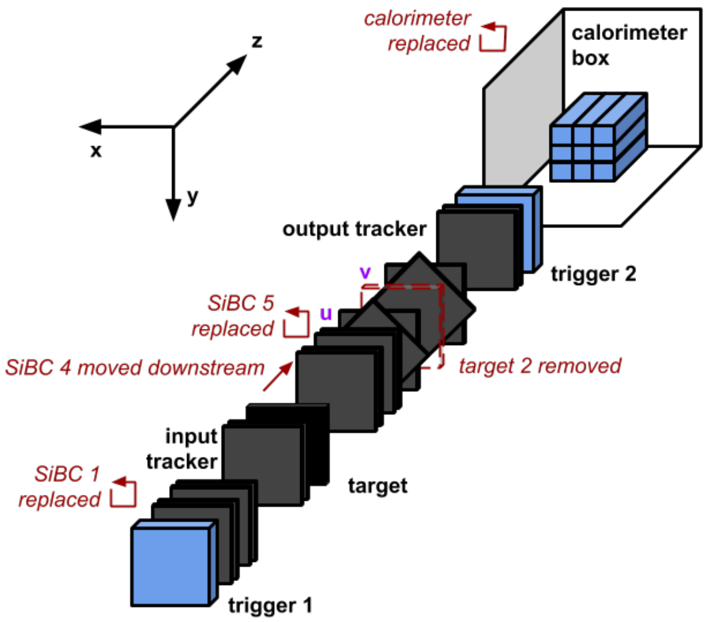

FIGURE 2.31. Hardware modifications to the feasibility test setup.

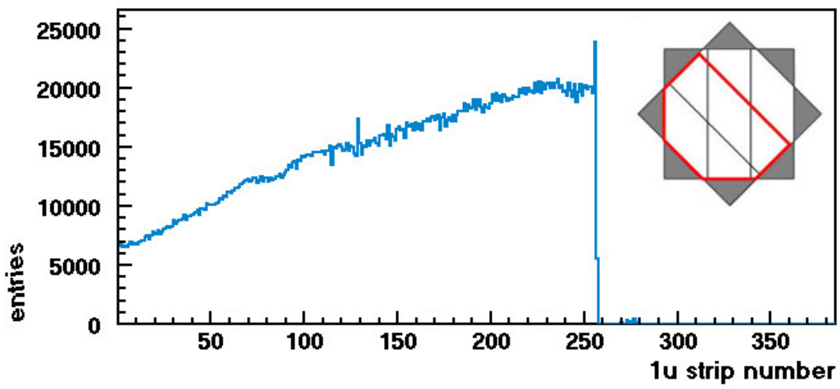

FIGURE 2.32. $1u$ beam profile: the third ASIC (which reads the strips in the $(256, 384)$ range) malfunctioning is clearly visible; the reduction of the corresponding tracking module active area is shown.

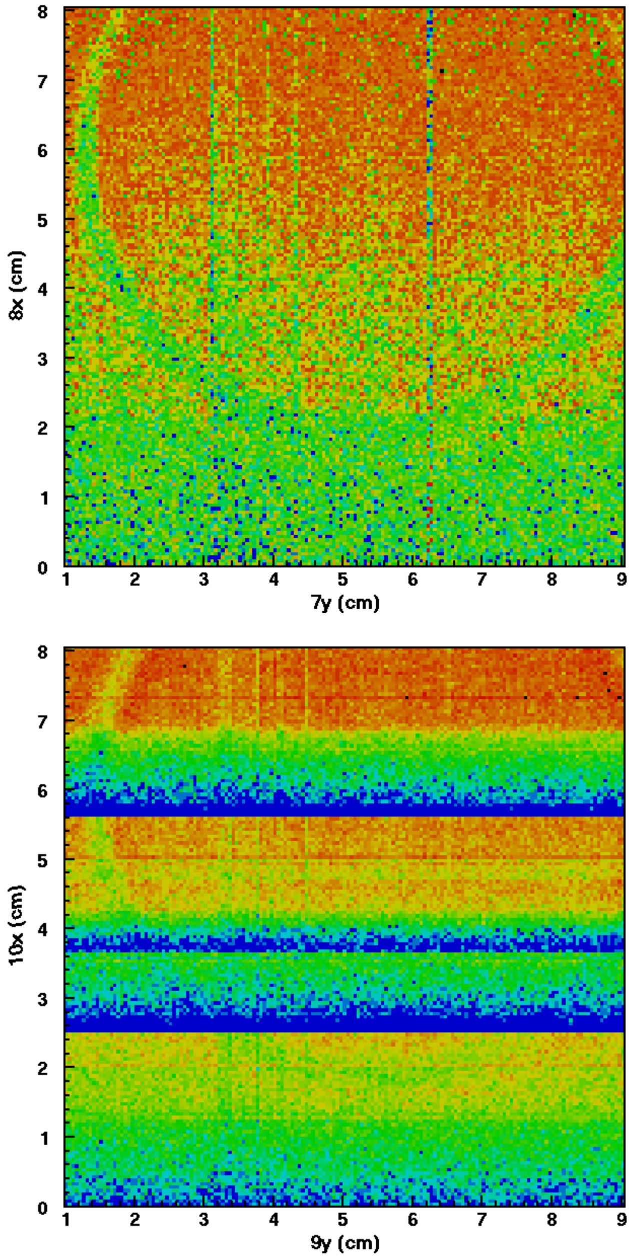

FIGURE 2.33. $(7y, 8x)$ *(top)* and $(9y, 10x)$ *(bottom)* hit point distributions measured before the malfunctioning tracking module replacement. The circular pattern is due to an upstream vacuum pipe or to the inner part of the COMPASS++ TPC, which was installed upstream with respect to the MUonE apparatus during the first month of data taking.

weeks of the data taking, in which the COMPASS++ apparatus was installed upstream with respect to the MUonE area: both the tracking modules reconstruct the same circular pattern, which is due to an upstream vacuum pipe or to the inner part of the COMPASS++ TPC [121], but the $10x$ inefficiency pattern is clearly visible in the horizontal bands in figure 2.33 bottom.

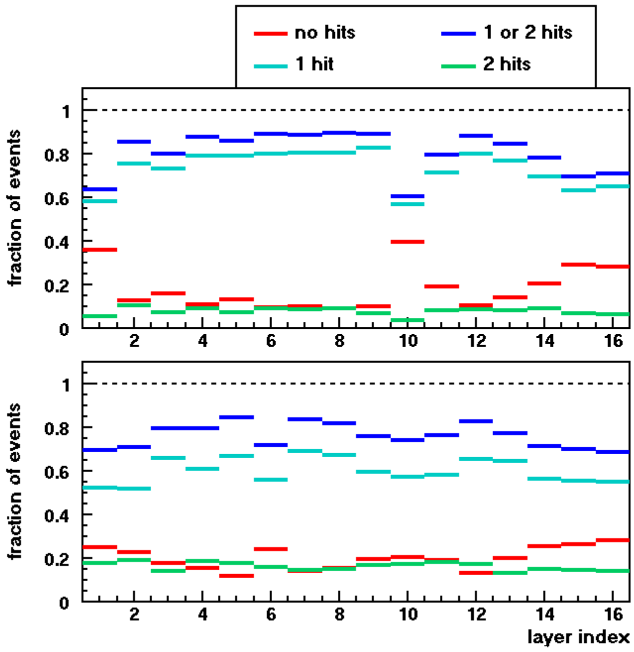

FIGURE 2.34. Multiplicity fractions for each silicon layer in the tracking setup 1 *(top)* and 2 *(bottom)*. Layers $1u$-y, $2x$, $9y$ and $10x$ differ between the two configurations. In the setup 2 case the beam intensity was higher.

Figure 2.34 shows the fraction of zero-, single- and double-hit events measured over different time intervals with the tracking setup 1 (top) and 2 (bottom): it is clear that the $1u$ and $10x$ layer replacement improved the hit detection efficiency, which in setup 2 is similar among all the tracking stations. The malfunctioning tracking modules were replaced with two INSULAb Silicon Beam Chambers (SiBC) [122].

Many other silicon layers exhibited minor issues, but they did not need to be replaced since their malfunctioning could be treated by means of software corrections. Details on these issues and on their treatment will be given in section 3.6.

It has to be noted that many components of the tracking system were disinstalled on September 18$^{\text{th}}$ and reinstalled on September 26$^{\text{th}}$; although all the silicon detectors were reinstalled (setup 2b) at the same positions along z they were located at before the disinstallation (setup 2a), different alignment parameters (section 3.4) are needed for the track reconstruction with the two different datasets.

CHAPTER 3

Data collection and conditioning

The 2018 MUonE feasibility test lasted more than seven months and resulted in the collection of more than 1.4 billions of events. The identification and characterization of the $\mu^{\pm}e^{-}$ elastic scattering candidates in such a large dataset requires several levels of data conditioning and filtering.
This test did not limit itself to the exploration of the possibility of exploiting the setup described in chapter 2 to detect the $\mu^{\pm}e^{-}$ scattering; indeed, part of its goal was the experimental evaluation of all the contributions that this apparatus gives to the total uncertainty on the kinematics reconstruction. The quest for high precision resulted in the development of many software tools for data conditioning. This chapter summarizes the steps of the analysis procedure and describes in detail the features of the software developed for the tracking system alignment, for the calorimeters calibration and for the offline correction of many detector issues.

3.1 Statistics summary

Figure 3.1 shows the timeline of the MUonE 2018 data taking: in particular, the input particle intensity per spill, together with the running of the collected statistics (top) and the writing rates for the raw data and for the Data Summary Tape (DST) files (bottom) are shown. All the stop sessions mentioned in section 2.3 are clearly visible.
During the $\sim$ 6 month long net data taking period, $\sim$ 1431781705 raw events have been collected ($\sim$ 1 TB). An online selection has been performed on this dataset with the following conditions, which do not affect the elastic events detection efficiency:

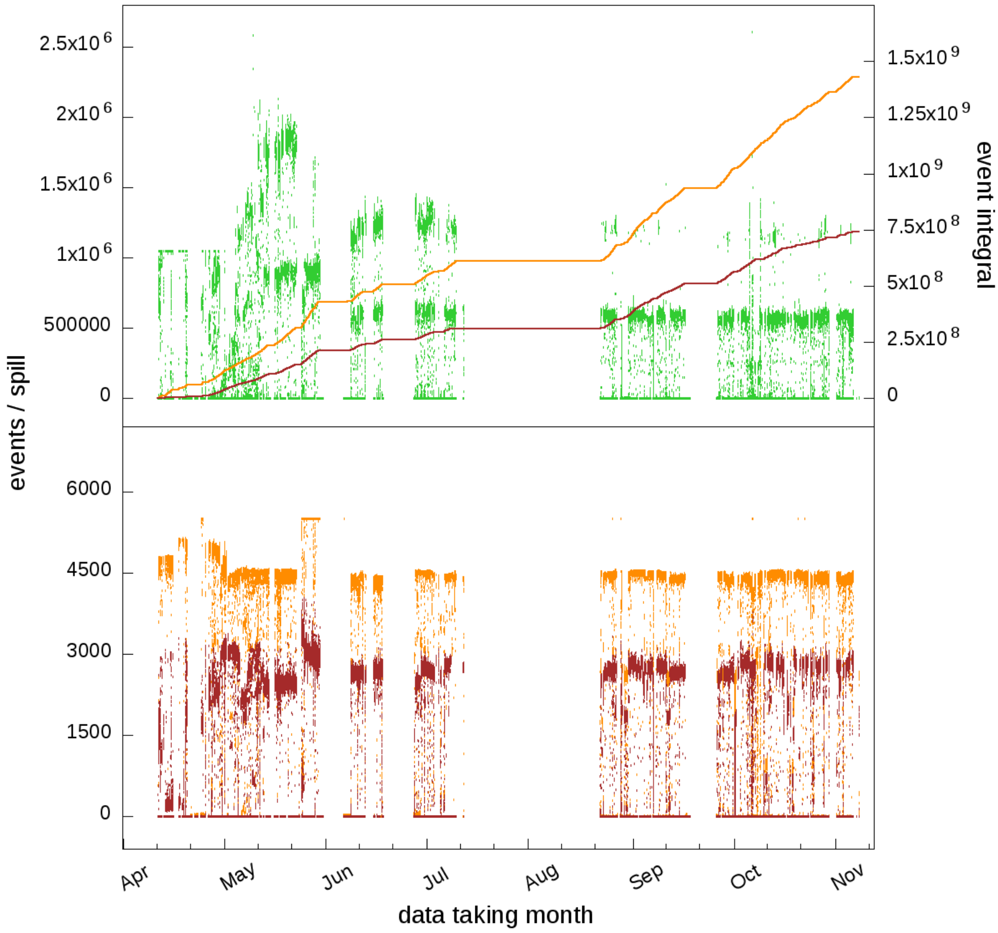

FIGURE 3.1. *(top)* Timeline of the number of incoming particles per spill measured by the S1+S2 coincidence; the scaler saturation at 1048575 can be observed in the first month; the $\sim 0.6 \times 10^6$ events/spill ($\sim 1.2 \times 10^6$ events/spill) level corresponds to the one-spill (two-spill) cycle; the orange (red) line indicates the integral of the number of events in the HBOOK (DST) files. *(bottom)* Timeline of the number of events written in the HBOOK (orange) and in the DST (red) files.

- 1 hit on layers $4x$, $5y$ and $6x$ and ≤ 1 hit on layer $3y$ in the tracking setup 0 (commissioning phase, with 7 tracking stations only and the sampling calorimeter);
- 1 or 2 hits on layers $2x$, $4x$, $5y$ and $6x$ in the tracking setup 1 and 2 (figure 3.2).

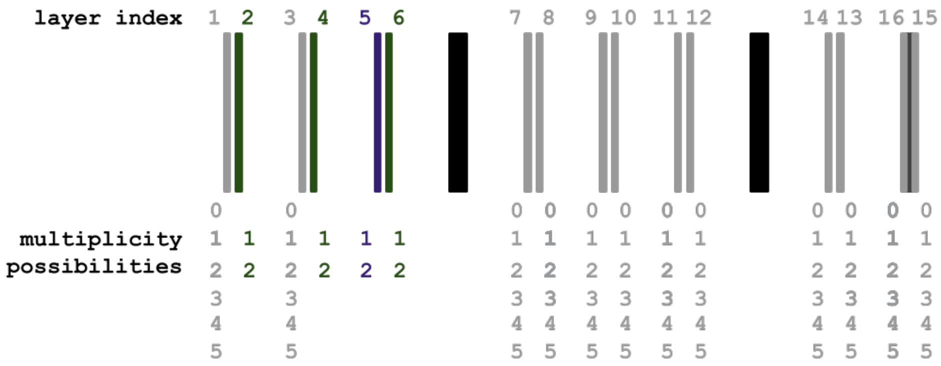

FIGURE 3.2. Multiplicity selection on the tracking system raw data.

The selected events have been written in DST ASCII files (section 3.3). Leaving aside the data collected during the commissioning phase and when the apparatus was missing some components, ~ 552833856 events have been written; among these, ~ 152451096 have been written before the downstream target removal. Table 3.1 shows the details of the collected statistics.

setup	calorimeter	nr. of targets	events in the DST files
1	STEFI	2	106416401
	GENNI		46034695
		1	50136819
2a			119286576
2b			230959365

TABLE 3.1. Summary of the DST files statistics.

3.2 Data analysis environment

A scheme of the whole analysis process in shown in figure 3.3. The silicon strip indexes and charge signals and the Pulse Height (PH) and hit time of all the calorimeter channels (9 in the STEFI and GENNI cases) are written in HBOOK ntuples. The online procedure identifies the hit positions and produces the DST

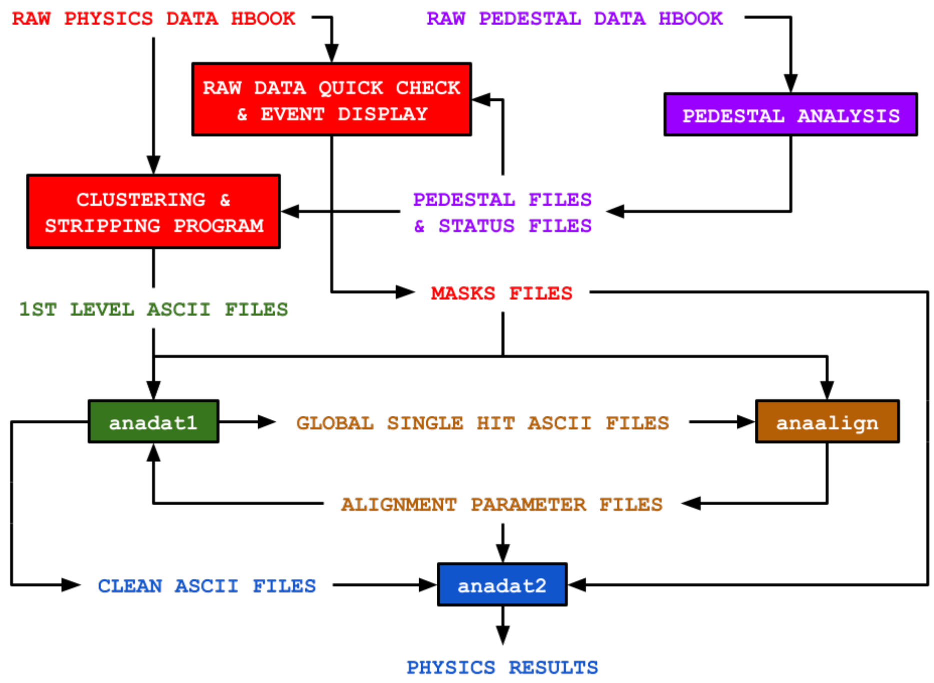

FIGURE 3.3. Data analysis scheme. Each step is described in detail in the text.

files, which undergo two stages of offline data conditioning and event selection, generating second level DST files with the elastic candidates only.
In the following sections the good event selection conditions and the preliminary data conditioning procedures will be described. Details on the physics analysis will be given in chapter 4.

3.3 From raw data to DST files

The computation of the cluster total signals and positions from the charge of the single strips, the input multiplicity selection and the DST files writing are performed event by event in real-time.

3.3.1 Pedestal analysis

The first step in the tracking raw data analysis is the pedestal subtraction. The pedestal is the signal level measured when there is no particle crossing the sensor; it depends on the baseline of both the detector and its electronic chain [97, 104]. In order to evaluate the pedestal and the noise of each strip, the so-called pedestal runs are performed with ~ 200 random triggers and the signal distribution of each strip is analyzed: the resulting mean value and RMS correspond to the pedestal and noise respectively [97, 104]. Figure 3.4 shows the noise values as a function of the strip number for all the MUonE silicon layers.

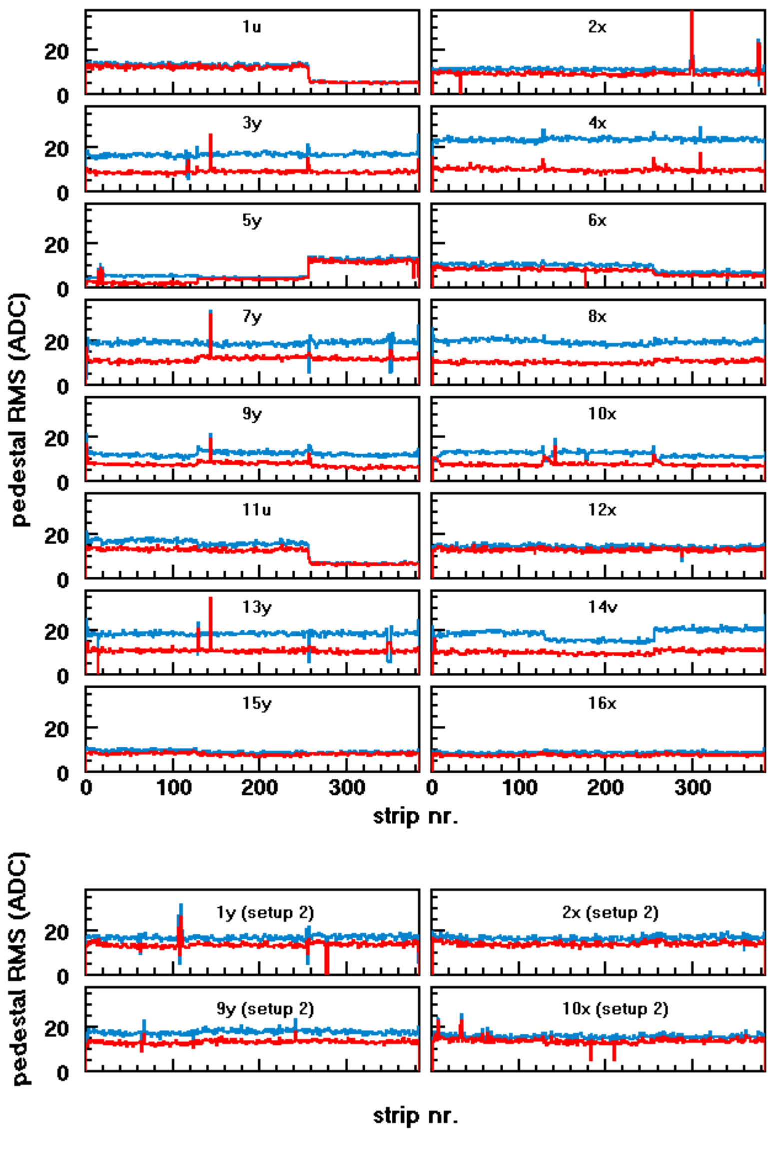

FIGURE 3.4. Noise distributions of the silicon detectors: those used in setup 1 *(top)* and the malfunctioning layers replacements *(bottom)*. The light blue (red) distributions have been obtained before (after) the CM subtraction. The malfunctioning channels are characterized by the RMS spikes.

The RMS distributions allow

- to identify the noisy or dead channels, which are marked as not working in a status file and excluded from the physics analysis, and to set the threshold values for the zero suppression [97, 104];
- to evaluate the so-called Common Mode (CM) noise, i.e. the contribution given by the external electromagnetic noise that couples to the detector bias line, which results in a common baseline fluctuation of all the detector channels [97, 104].

The CM contribution is evaluated event by event and ASIC by ASIC as the average difference between the raw PH and the pedestal. Once the common mode subtraction has been performed, only the intrinsic noise is left. The CM evaluation can only be performed when in normal mode acquisition, given the fact that it is computed as the average fluctuation of all the channels. Since MUonE typically runs in zero suppression mode, the CM suppression cannot be performed; nevertheless, since the CM values are small (figure 3.4) their contribution to the silicon detectors performance is negligible[1].

3.3.2 Cluster reconstruction

Once the pedestal (and CM, if available) subtraction has been performed, the hit (or cluster) positions are identified. Figure 3.5 shows the cluster reconstruction steps:

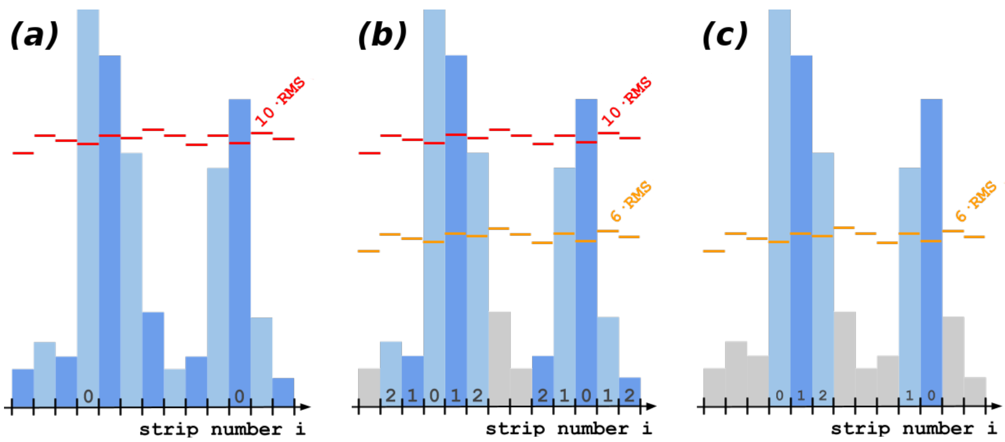

FIGURE 3.5. Hit reconstruction steps: *(a)* identification of the over threshold channels; *(b)* loop on the neighbouring channels; *(c)* identification of the cluster member channels and center of gravity evaluation.

[1]If the CM values were larger, the zero suppression could not be used: indeed, high CM values result in a high noise, in the saturation of the maximum number of over threshold strips and in detection inefficiencies.

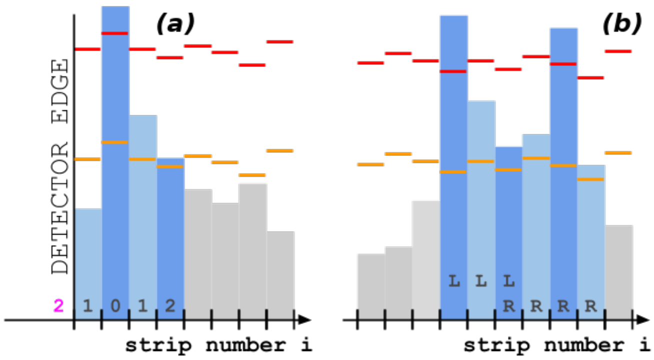

FIGURE 3.6. Hit reconstruction limit cases: *(a)* boundary cluster; *(b)* pair of close clusters that overlap; *(c)* cluster with a under threshold strip between two over threshold strips.

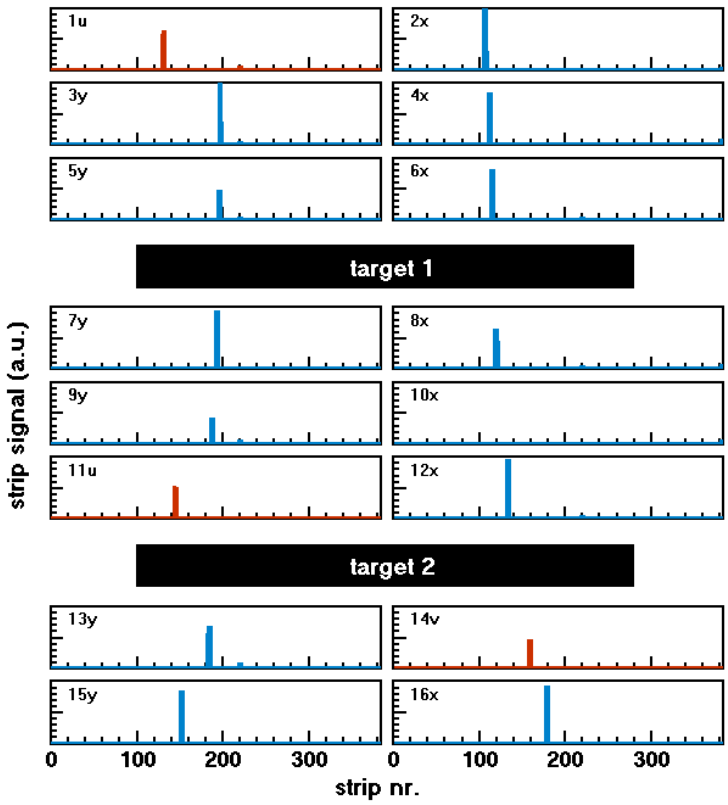

FIGURE 3.7. Example of event display showing a full-single-hit event. Stereo coordinates are shown in red.

- for each layer, the strip PHs are compared to the corresponding pedestal RMS values; the strips whose signal is larger than 10 times the RMS value are selected.

- For each of the selected strips, the two closest neighbouring channels per side are considered; only the strips whose signal is larger than 6 times their RMS values are included in the cluster.

- The position of the cluster reconstructed starting from the m-th strip is evaluated with the COG, defined as [96]

$$x^{\text{meas}}(m) = \frac{\sum_{i=-2}^{+2} (m-i) \cdot \text{PH}\,(m-i)\Big|_{\text{over thr}}}{\sum_{i=-2}^{+2} \text{PH}\,(m-i)\Big|_{\text{over thr}}} w_{\text{ro}} \tag{3.1}$$

  where $w_{\text{ro}} = 242$ μm is the readout pitch and $\text{PH}(l)|_{\text{over thr}} = 0$ if the l-th channel signal is under the $6 \cdot \text{RMS}$ threshold.

The way this hit reconstruction algorithm treats some limit cases is non-trivial and requires a dedicated discussion. In particular:

- there must be a $\geqslant 3$-strip distance between the central strips of adjacent clusters.

- When in zero suppression mode, the cluster position is reconstructed using the available strip signals.

- If the central strip is near the sensor edge (i.e. the 1-st, 2-nd, 383-rd or 384-th one), the range of the loop around it is properly redefined (figure 3.6a).

- If two clusters overlap, the strips in the intersection region enter both the hit positions evaluation (figure 3.6b).

- If there is a strip under the $6 \cdot \text{RMS}$ threshold between two strips over threshold within a loop on the central channel neighbours, the former is excluded from equation 3.1 while the latter are included (figure 3.6c); as shown in subsection 3.6.1.3, in general this biases the hit position reconstruction.

A first level raw data analysis algorithm allows to compute the statistical distributions of all the information stored in the raw ntuples and hence to perform a real-time check of the collected data. Furthermore, an online event display (figure 3.7) represents a useful tool to check the silicon sensors alignment and orientation.

3.4 Tracking system alignment

In general, the few-µm spatial resolution of modern position-sensitive detectors is considerably smaller than the accuracy of the mechanical assembly [123]. It is therefore essential to use software tools for the offline determination of the tracking planes position with high precision [123].
Figure 3.8a shows an example of a layer misalignment: the central 1D (y) layer has a lateral shift and a tilt around z with respect to the reference system defined by the upstream and downstream tracking stations. If the central layer were perfectly aligned to the reference, both the green and blue tracks would cross the orange strip; on the other hand, the actual positions reconstructed by the layer (green and blue strips) present an overall shift with respect to the former and differ from each other due to the tilt.
These shifts and tilts can be corrected in many different ways. A survey on several software alignment methods is given in [123, 124]. The so-called histogram method has been exploited for the MUonE alignment: its basic idea is to extract the information on the relative shifts and tilts from the residual histograms [123]. For single-coordinate tracking detectors, the residual of the n-th plane is defined as [96, 97]

$$\rho_n = x_n^{\text{meas}} - x_n^{\text{true}} \tag{3.2}$$

where x_n^{meas} is the hit position reconstructed by the tracking plane and x_n^{true} is the projection to the n-th plane of the track identified by the reference detectors. These detectors are supposed to be perfectly aligned and thus they do not enter the alignment procedure. If the contribution of the mechanical assembly to the hit reconstruction uncertainty is the same for each detector, which is reasonable if all the tracking stations share the same mechanical support, the uncertainty on x_n^{true} reduces as the reference system lever arm increases, i.e. as the reference pairs relative distance increases. Furthermore, the use of the external detectors, i.e. the first and the last one along the beam direction, as reference layers minimizes the MCS contribution to the alignment performance.
The parameters obtained from the residual distributions allow to correct

- the shifts:

$$x_n^{\text{meas}} \rightarrow x_n^{\text{meas}} - S_n \tag{3.3}$$

  where $S_n = \langle \rho_n \rangle$ corresponds to the mean value of the ρ_n distribution.

- The tilts:

$$x_n^{\text{meas}} \rightarrow x_n^{\text{meas}} - T_n \left(y_n^{\text{meas}} - \frac{W}{2} \right) \tag{3.4}$$

  where y_n^{meas} is the hit position reconstructed by another layer whose measurement direction differs from the n-th one and W is the sensor width. Both equation 3.4 and the relation

$$\rho_n \left(y_n^{\text{meas}} \right) = T_n y_n^{\text{meas}} + q \tag{3.5}$$

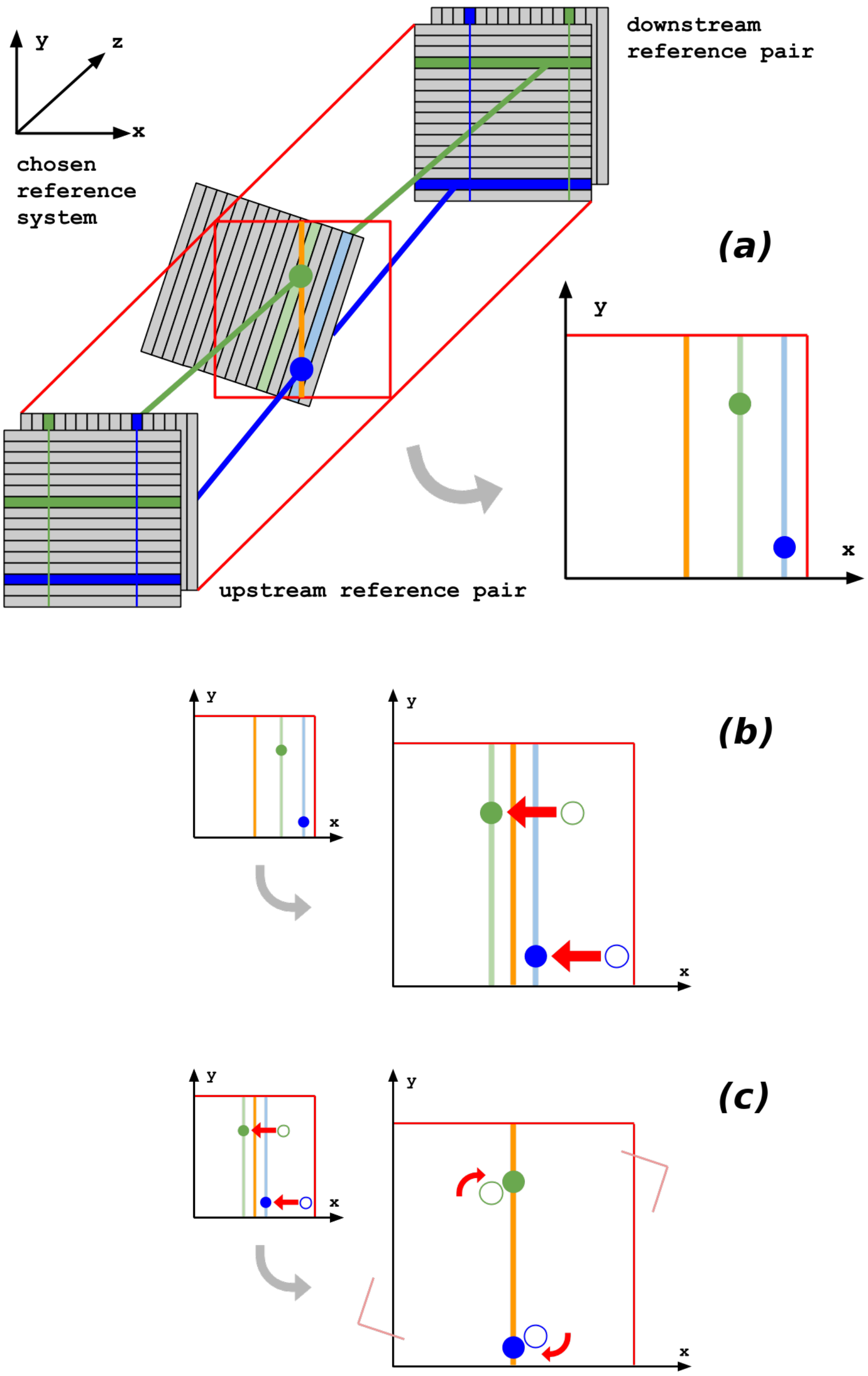

FIGURE 3.8. Tracking layer alignment with respect to a fixed reference system (red) based on two tracks (green and blue). The hit position in case of perfect alignment is depicted in orange. The actual misalignment *(a)* requires shift *(b)* and tilt *(c)* corrections.

result from the linear approximation of a small-angle rotation around z and hence are limited to $\ll 1$ rad tilts.

This method can be applied to the example of figure 3.8a: the shift correction (equation 3.3) centers the mean of the measured hit positions within the orange strip (figure 3.8b), but the difference between them is still present and requires the transformation in equation 3.4, which introduces a correlation between the measured positions of the n-th layer and of an opposite-view partner layer (figure 3.8c). It has to be stressed that these corrections are relative to the reference detectors, which in practice are not perfectly aligned; the reference system possible large displacements should be minimized in the installation phase.

3.4.1 The iterative algorithm

The alignment algorithm developed for the MUonE feasibility test applies the histogram method iteratively to the tracks of the single input muons that do not undergo either $\mu^{\pm}e^{-}$ scattering or any inelastic interaction within the apparatus. Dedicated DST files with such single track events have been produced by the first level analysis software (figure 3.3).
The algorithm consists of two steps:

- in the first one, all the xy detectors are shifted and rotated around z to be aligned to a fixed reference system (two x and two y planes) in N iterations.
- In the second one, the projections of the global single tracks to the stereo planes z are used to compute the residual distributions for the stereo detectors along their coordinate; they are then aligned in the same way as the xy ones in N iterations.

The reference pairs have been chosen in order to maximize their relative distance: the $(3y, 4x)$ and $(15y, 16x)$ stations have been used for the setup 1 data (the $(1u, 2x)$ station has been discarded because of the stereo layer) while the $(1y, 2x)$ station has been used as the upstream pair for the setup 2 data. All the reference detectors showed an excellent performance with the only exception of the $3y$ layer; nevertheless, as it will be discussed in subsection 3.6.1.1, the $3y$ layer malfunctioning results only in a lower detection efficiency while its spatial resolution is not affected.
Table 3.2 shows the tilt correction partners chosen for all the layers. The most important criterion in choosing the partners is the independence between the three different tracking stations (input, target 1 and target 2 output – see subsection 2.3.2); indeed, $\mu^{\pm}e^{-}$ elastic interactions in the targets change the input trajectories and thus break the correlations between the input and output stations measured positions.
Furthermore, the MCS contribution to the particle track between a layer and its partner limits the alignment precision and thus, when possible, has to be minimized. Nevertheless, there are many exceptions:

	tilt partner (setup 1)	tilt partner (setup 2)
1*u*-*y*	$2x$	–
2*x*	$3y$	–
3*y*	–	$4x$
4*x*	–	$3y$
5*y*	$6x$	$6x$
6*x*	$5y$	$5y$
7*y*	$8x$	$8x$
8*x*	$7y$	$7y$
9*y*	$12x$	$12x$
10*x*	$9y$	$9y$
11*u*	$12x$	$12x$
12*x*	$9y$	$9y$
13*y*	$16x$	$16x$
14*v*	$15y$	$15y$
15*y*	–	–
16*x*	–	–

TABLE 3.2. Tilt correction partner layers. Reference layers do not enter the alignment procedure, therefore they have no partner.

- since stereo layers enter the procedure only at the second stage, it has been chosen not to use them as xy layer partners.
- Albeit included in the alignment procedure, the $10x$ layer has not been used as a partner due to its not working properly (subsection 2.3.8).

In the k-th algorithm iteration, the residuals are computed and their distributions are used to extract the k-th corrections to the alignment parameters, $S_n^{(k)}$ and $T_n^{(k)}$. The $S_n^{(k)}$ shift correction parameters are obtained via Gaussian fits on the $\rho_n^{(k)}$ distributions (examples in figures 3.9 top and 3.10 top). The $T_n^{(k)}$ tilt correction parameters are obtained via linear fits of the form shown in equation 3.5 on the $(y_n^{\text{meas }(0)}, \rho_n^{(k)})$ profile plots (figures 3.9 bottom and 3.10 bottom), where $y_n^{\text{meas }(0)}$ is the position reconstructed by the n-th partner before any alignment iteration.
The total relative transverse shifts are in general rather large (up to ~ 8 mm). Since the main contributions to the shift adjustment (typically $\gtrsim 90\%$) come from the first iteration, this iteration only shifts the residual distributions to approximately zero and does not correct for the tilts, whose evaluation starts

from the second iteration; in other words, the $T_n^{(1)}$ term is forced to be zero for all the layers.
Once the $S_n^{(k)}$ and $T_n^{(k)}$ have been found, the position of each layer can be rewritten as

$$\begin{aligned} x_n^{\text{meas }(k)} &= x_n^{\text{meas }(k-1)} - S_n^{(k)} - T_n^{(k)} \left(y_n^{\text{meas }(0)} - \frac{W}{2} \right) \\ &= x_n^{\text{meas }(0)} - \sum_{q=1}^{k} S_n^{(q)} - \sum_{q=1}^{k} T_n^{(q)} \left(y_n^{\text{meas }(0)} - \frac{W}{2} \right) \end{aligned} \tag{3.6}$$

where $x_n^{\text{meas }(0)}$ is the unaligned position of the n-th layer. The $x_n^{\text{meas }(k)}$ replace the $x_n^{\text{meas }(k-1)}$ in the $(k+1)$-th iteration.
After N iterations the final alignment parameters

$$S_n = \sum_{k=1}^{N} S_n^{(k)} \qquad \text{and} \qquad T_n = \sum_{k=1}^{N} T_n^{(k)} \tag{3.7}$$

and the aligned positions

$$x_n^{\text{meas}} = x_n^{\text{meas }(0)} - S_n - T_n \left(y_n^{\text{meas }(0)} - \frac{W}{2} \right) \tag{3.8}$$

are obtained.
As an example, figures 3.9 and 3.10 show the comparison between the residual distributions of two layers after 1 (left) and 7 (right) iterations. In particular:

- figure 3.9 refers to the $9y$ layer in setup 1; besides the transverse shift that has been corrected in the first iteration, this layer only presents a little tilt around z and hence proves to be a priori well-aligned.
- Figure 3.10 refers to the setup 2b $12x$ layer; in this case a major tilt, which increases the residual distribution width and thus the spatial resolution, is observed. Furthermore, such a tilt makes the inefficiency pattern (introduced by the exclusion of active regions via the masks – subsection 3.6.1.3) affect the distribution in figure 3.10 top-left by breaking its peaked shape. Nevertheless, the plots in figure 3.10 right show that the algorithm is able to treat these issues.

In general, the unaligned $x_n^{\text{meas }(0)}$ and $y_n^{\text{meas }(0)}$ positions correspond to the raw positions given by equation 3.1; however, for some tracking planes dedicated corrections have to be applied prior to the alignment procedure. A priori corrections are needed in three cases:

- if the tracking plane is tilted around a transverse axis. This is the case of the $9y$ layer, which is discussed in subsection 3.4.2.

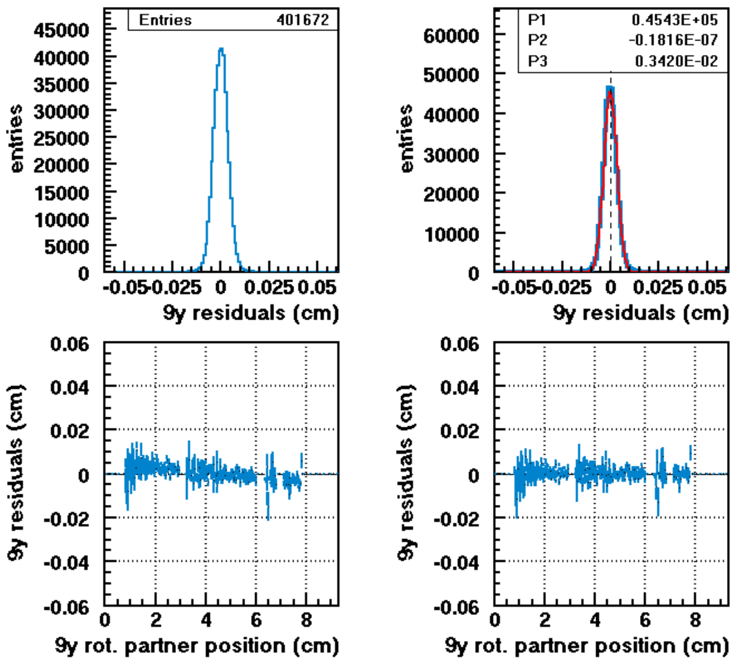

FIGURE 3.9. Alignment of the $9y$ layer in setup 1 after 1 *(left)* and 7 *(right)* iterations. *(top)* The $\rho_{9x}^{(k)}$ distribution. *(bottom)* The $(x_{12x}^{\text{meas }(0)}, \rho_{9y}^{(k)})$ profile plot.

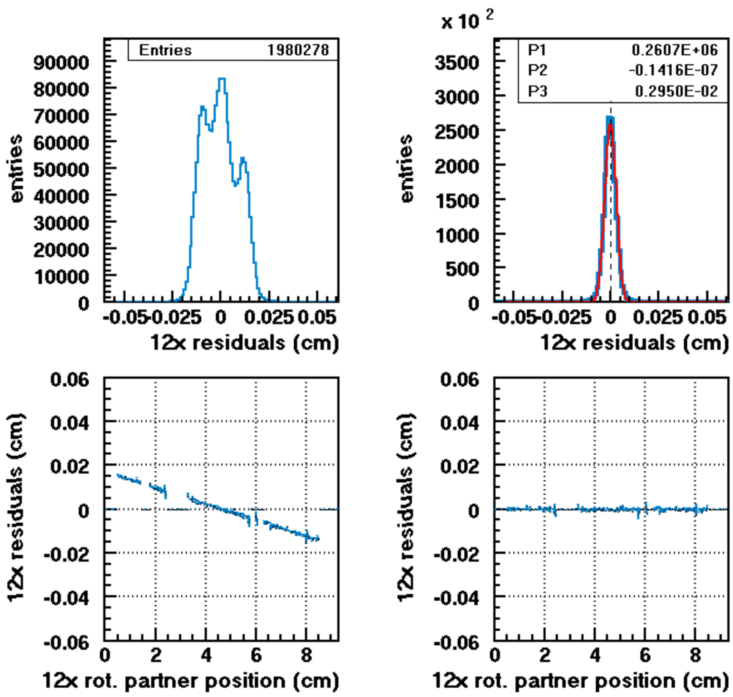

FIGURE 3.10. Alignment of the setup 2b $12x$ layer after 1 *(left)* and 7 *(right)* iterations. *(top)* The $\rho_{12x}^{(k)}$ distribution. *(bottom)* The $(x_{9y}^{\text{meas }(0)}, \rho_{12x}^{(k)})$ profile plot.

- For stereo layers, whose actual stereo angle in general differs from the design one. All the MUonE stereo layers are supposed to be at 45° with respect to the x and y axes, while the effective angles differ from each other. Details on this topic are given in subsection 3.4.3.
- If a single ASIC malfunction introduces a local bias in the position reconstruction, i.e. a shift whose value depends on the hit point on the sensor. The $3y$ and $5y$ layers presented such an issue, which will be described in detail in subsection 3.6.1.

The histogram method proves to be a versatile tool to study and treat all these items. Since none of these corrections introduces a correlation with the tilt partner layers, all the treatments can be performed prior to the alignment, regardless of the partner layer multiplicity and, in case of multiple clusters, independently for each hit point. Leaving aside the first item, all the correction values depend on the choice of the reference tracking planes.

3.4.2 Transverse tilts

Figure 3.11 shows how a tilt with respect to a transverse axis affects the absolute hit point reconstruction: if the tilted layer measures along the direction orthogonal to the rotation axis, such a tilt introduces a dependence of the layer residuals on its measured hit positions.

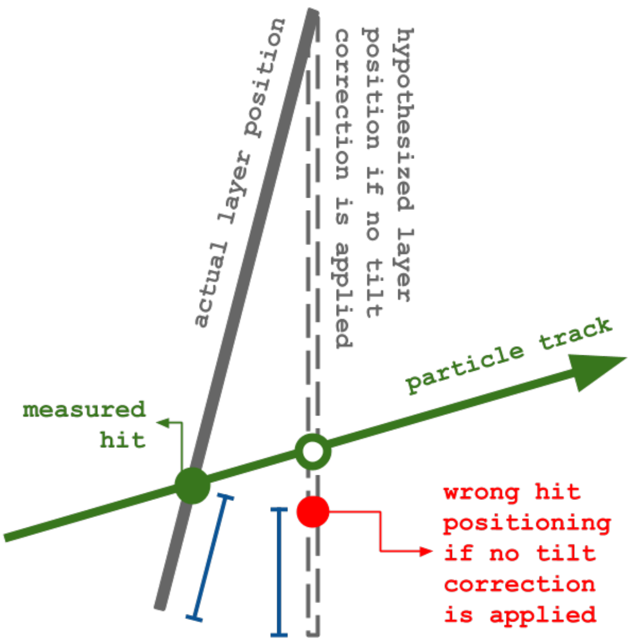

FIGURE 3.11. Hit position bias induced by a tilt around a transverse axis.

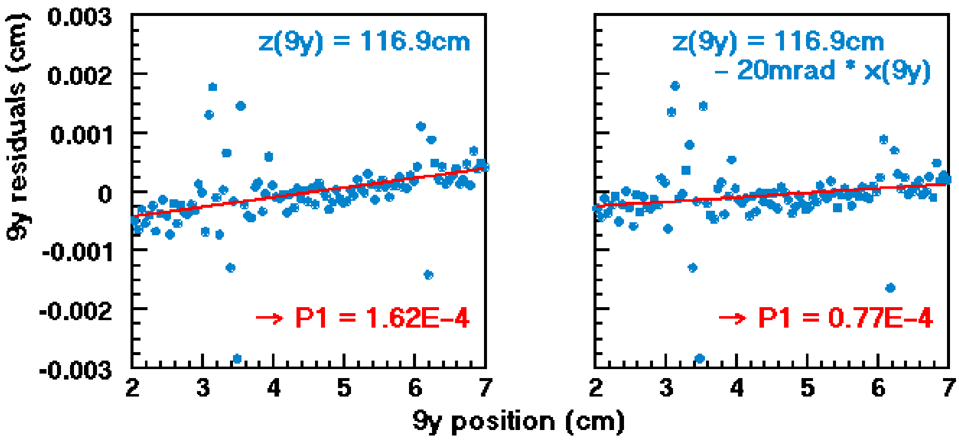

FIGURE 3.12. Effect of the $9y$ tilt around the x axis on the measured position.

The MUonE tracking detectors are approximately parallel to each other. The only exception is represented by the $9y$ layer of setup 1, for which a ~ 20 mrad tilt around the x axis was measured. Such a small tilt does not affect the position reconstruction heavily: as shown in figure 3.12 left, a linear fit on the $(x_{9y}^{\text{meas }(0)}, \rho_{9y}^{(k)})$ profile plot results in a 1.62×10^{-4} slope, which means that two hit positions 10 cm far one from the other along y present a relative displacement of ~ 16 µm only.
Nevertheless, a correction of the form

$$z_{9y} \to z_{9y} - 20 \text{ mrad} \cdot x_{9y}^{\text{meas }(0)} \tag{3.9}$$

has been performed in the setup 1 alignment phase: figure 3.12 right shows that the tilt effect has been reduced.

3.4.3 Wrong stereo angle correction

Figure 3.13 shows the effect a bias on the stereo angle value has on the layer residuals: such a bias introduces a dependence of the stereo layer residuals on its measured positions, which is not corrected by the alignment procedure. This effect is treated with the a priori transformation

$$x_n^{\text{meas }(0)} \to x_n^{\text{meas }(0)} - A_n \left(x_n^{\text{meas }(0)} - \frac{W}{2} \right) \tag{3.10}$$

where A_n is a correction factor that is computed as the slope of the linear fit of the $(x_n^{\text{meas }(0)}, \rho_n)$ distribution. An example of this procedure is shown in figure 3.14:

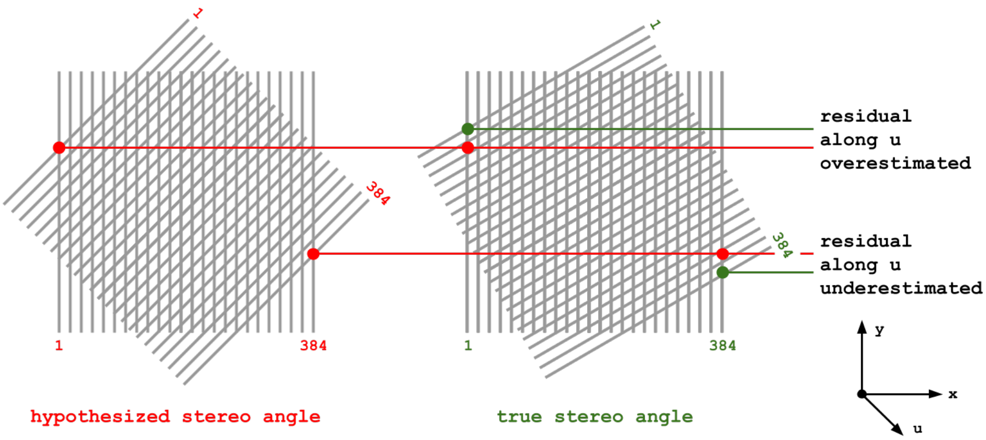

FIGURE 3.13. Scheme of the wrong stereo angle effect on the residuals. The green (red) dots represent the true (reconstructed) hit points of two events that cross the $(1, 1)$ and $(384, 384)$ strips of the ux layer.

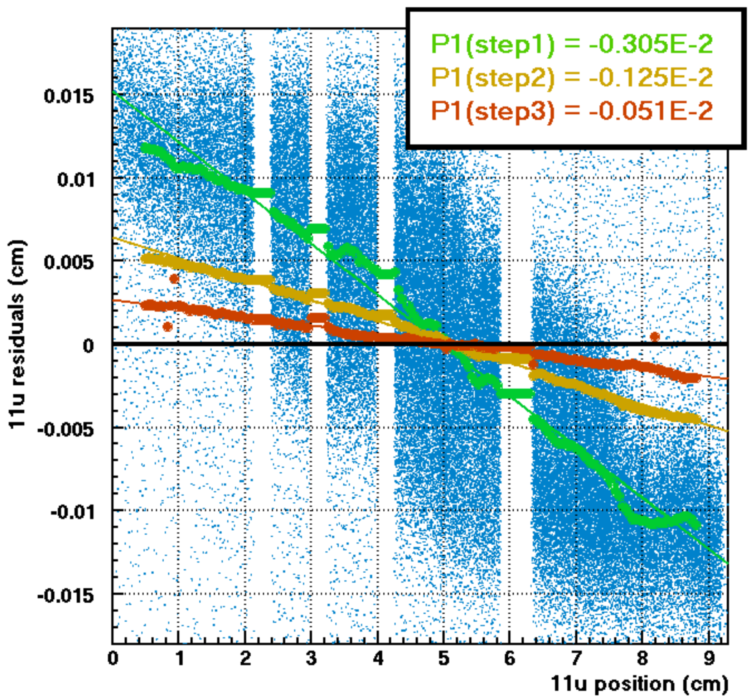

FIGURE 3.14. Iterative wrong stereo angle correction for the setup 2 $11u$ layer; the results of the first (green), second (yellow) and third (red) iterations are shown.

- the $(x_n^{\text{meas }(0)}, \rho_n)$ distribution (light blue) is split into many x slices.
- A Gaussian fit is performed on all the slices, and the resulting mean values fill an array (green, yellow and red points).
- A linear fit is performed on the array (green, yellow and red lines).

As can be seen in figure 3.14, this procedure requires multiple iterations to converge; three iterations have been performed on the $1u$, $11u$ and $14u$ layers data. Table 3.3 shows the overall A_n values.

	setup 1 $[\times\mathbf{10^{-2}}]$	**setup 2a** $[\times\mathbf{10^{-2}}]$	**setup 2b** $[\times\mathbf{10^{-2}}]$
$\mathbf{1u}$	-1.028	–	–
$\mathbf{11u}$	-0.581	-0.482	-0.533
$\mathbf{14v}$	-0.139	-0.139	-0.158

Table 3.3. A_n values.

The transformation of equation 3.10 is similar to the one that corrects for the tilt around z (equation 3.4). In principle, the former could be implemented in the alignment algorithm and, hence, applied to the raw positions automatically. However, it has been observed that in general introducing the A_n as new degrees of freedom makes the procedure oscillate without converging.

3.4.4 Algorithm performance

Figure 3.15 shows the fraction of each contribution to the S_n and T_n as a function of the algorithm iteration. As already mentioned, for both the xy and stereo layers the first iteration is responsible of the largest contribution to the shift correction, while no rotation around z is applied. The subsequent introduction of equation 3.4 is counterbalanced by another non-negligible shift correction term in the third iteration; after this, the procedure converges. It takes 6 iterations for all the alignment parameter new contributions to be smaller than 1 ppm of the initial misalignment.
The evolution of the $\rho_n^{(k)}$ distribution width as a function of k is shown in figure 3.16. Since the first iteration results consist in mere shifts, they do not contribute to the distributions narrowing. On the other hand, the width values rapidly converge to their asymptotic values after the introduction of the tilt corrections: all the distributions are $\lesssim 50$ µm large after the third iteration, and further changes are typically smaller than 1 µm.

3.4.5 Alignment parameters and hit position errors

Table 3.4 (3.5) shows the setup 1 (2) alignment parameters obtained with 8-iteration runs. All the layers are centered with a < 1 µm precision. The residual

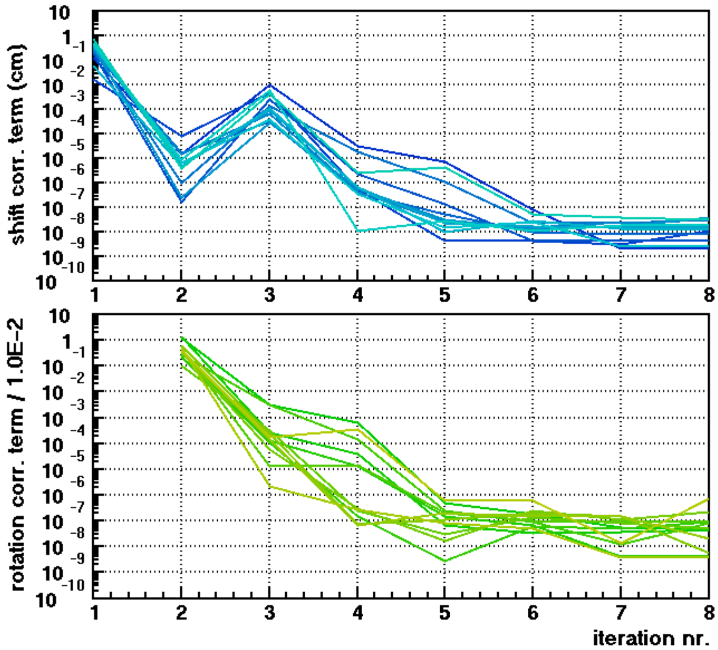

FIGURE 3.15. Fraction of the contributions to S_n and T_n as a function of the algorithm iteration. Example from the setup 1 tracking alignment.

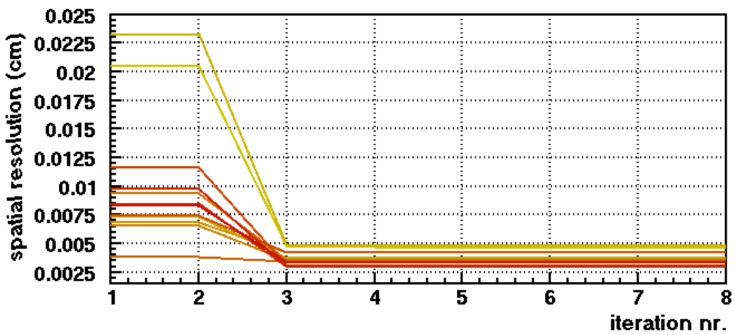

FIGURE 3.16. $\rho_n^{(k)}$ distribution widths as a function of the algorithm iteration number.

distribution widths σ_n are $\lesssim 50$ µm with the only exceptions of some of the reference system ones.
A dedicated procedure for the reference layers σ_n evaluation has been implemented: once all the tracking layers have been aligned by the algorithm shown in subsection 3.4.1, the tracks reconstructed by the non-reference layers are projected to the reference planes and the residual distributions of the latter are computed. This introduces a few-µm σ_n overestimation due to the shorter lever arm and the MCS. The σ_n values have been used as the hit position errors (chapter 4).

layer	S_n [cm]	T_n	σ_n [µm]
$1u$	−0.12295	0.011927	46.603
$2x$	0.022619	−0.013093	47.899
$3y$	–	–	55.918
$4x$	–	–	43.219
$5y$	0.18957	0.0033888	36.939
$6x$	−0.22793	−0.0023493	42.049
$7y$	0.26445	0.0028593	35.159
$8x$	−0.29645	−0.0047283	35.168
$9y$	0.38061	−0.0010178	34.203
$10x$	−0.40641	−0.0033258	42.507
$11u$	−0.058529	0.0063066	30.957
$12x$	−0.46827	−0.0039533	30.042
$13y$	0.50863	−0.0049534	29.319
$14v$	−0.73990	−0.0041395	33.565
$15y$	–	–	44.832
$16x$	–	–	45.615

TABLE 3.4. Setup 1 alignment parameters and width of the residual distributions.

3.5 Calorimeters calibration

The raw calorimeter channel PH is an integer in the $\sim(0, 3900)$ ADC range[2] and its hit time is an integer in the $(0, 255)$ ADC range. Figure 3.17 shows an example of PH-time scatter plot: physical events populate a high-PH peak in a narrow time interval; the delayed contribution is given by the pile-up events. Since the digitizer sampling rate is fixed at 250 MS/s [113], the physical time

[2]The digitizer $(0, 4095)$ ADC range is reduced because of the ~ 200 ADC baseline (different for each channel) subtraction performed prior to the HBOOK files writing.

layer	setup	S_n [cm]	T_n	σ_n [µm]
$1y$	2a	–	–	47.108
	2b	–	–	51.796
$2x$	2a	–	–	50.359
	2b	–	–	49.095
$3y$	2a	0.36600	0.00036523	43.049
	2b	0.46048	0.0033193	47.329
$4x$	2a	0.15244	0.0034155	44.734
	2b	0.19994	0.00053045	43.401
$5y$	2a	0.48684	0.0037756	37.415
	2b	0.56333	0.0061014	41.582
$6x$	2a	−0.10421	0.00038715	39.494
	2b	−0.065729	−0.0019349	39.627
$7y$	2a	0.52894	0.0024347	30.682
	2b	0.58697	0.0041967	33.693
$8x$	2a	−0.25348	−0.0017863	31.631
	2b	−0.22410	−0.0034990	30.910
$9y$	2a	0.043104	−0.0071451	33.028
	2b	0.14163	−0.0036992	35.214
$10x$	2a	−0.62966	−0.0013015	34.379
	2b	−0.57175	−0.0046992	35.280
$11u$	2a	0.082163	0.0061426	32.521
	2b	0.12141	0.0067226	31.065
$12x$	2a	−0.41206	−0.0025840	28.750
	2b	−0.39407	−0.0036492	29.504
$13y$	2a	0.60486	−0.0047581	28.371
	2b	0.62889	−0.0040427	29.005
$14v$	2a	−0.77969	−0.0033446	32.577
	2b	−0.78939	−0.0037680	31.650
$15y$	2a	–	–	38.362
	2b	–	–	38.334
$16x$	2a	–	–	47.100
	2b	–	–	48.082

TABLE 3.5. Setup 2 alignment parameters and width of the residual distributions.

range is $(0, 1020)$ ns.
On the other hand, in order to find the correspondence between the PH and the actual energy deposited in the detector by the incoming particles, a calibration with a monochromatic electron beam with tunable momentum is required. For this purpose, a beamtest at the CERN East Hall low-energy T9 beamline has been performed by the INSULAb group: this allowed the characterization of all the MUonE calorimeters in the elastic electron energy range (section 2.2). The details on the characterization methods will be discussed in appendix A.
The response of all the channels needs to be equalized for the total calorimeter energy to be computed. The equalization is performed via the transformation

$$\mathrm{PH}(i) \rightarrow Q_i \cdot \mathrm{PH}(i) \tag{3.11}$$

where Q_i is the ratio between the MIP peak values (Landau Most Probable Value – MPV) of the central channel, chosen as reference, and of the i-th channel. Table 3.6 shows the equalization coefficients[3].

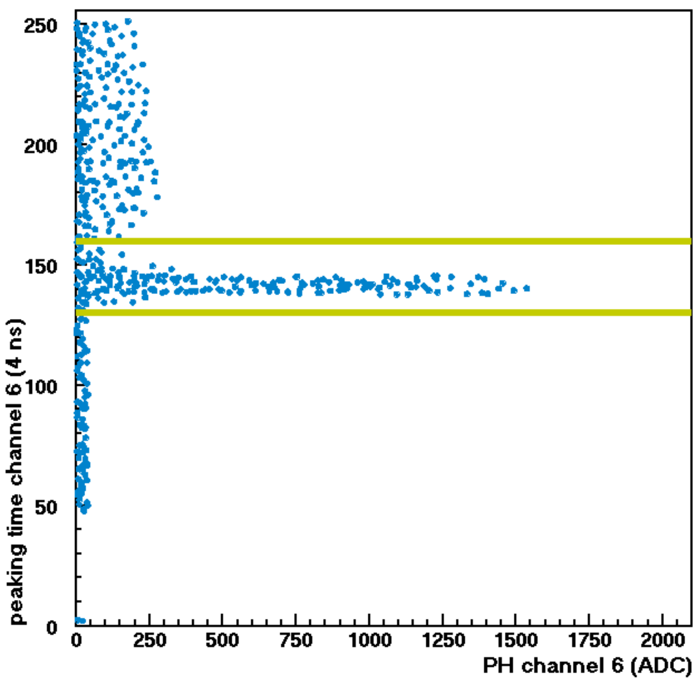

FIGURE 3.17. Example of STEFI channel PH-time scatter plot. The physical time range is highlighted in yellow.

[3]The GENNI MIP peak values have found to be different from the ones obtained with the T9 beamtest data and thus the Q_i required a correction factor – details are given in subsection 3.6.2.

	STEFI	GENNI
ch. 1	1.8	1.16943669
ch. 2	1.9288470	1.46265018
ch. 3	2.3659306	1.16958845
ch. 4	1.9565217	1.62025559
ch. 5	1	1.42088652
ch. 6	0.70810384	0.903954268
ch. 7	2.8002491	1.05852628
ch. 8	2.0594964	1.02562070
ch. 9	0.94221109	1.71203196

TABLE 3.6. Q_n values. The STEFI (GENNI) channel positions are shown in figure 2.23 (2.25).

Once equalized, the single channel signals can be summed:

$$\mathrm{PH}_{\mathrm{calo}} = \sum_{i=1}^{9} \mathrm{PH}(i)\Big|_{\text{on time}} \tag{3.12}$$

where only the channels whose signal is within the physical time range (figure 3.17) are included. The calorimeter energy is therefore computed with

$$E_{\mathrm{calo}} = C_0 + C_1 \cdot \mathrm{PH}_{\mathrm{calo}} \tag{3.13}$$

where C_0 and C_1 are the calibration coefficients (table 3.7) obtained by fitting the arrays in figure 3.18 with first-degree polynomials.

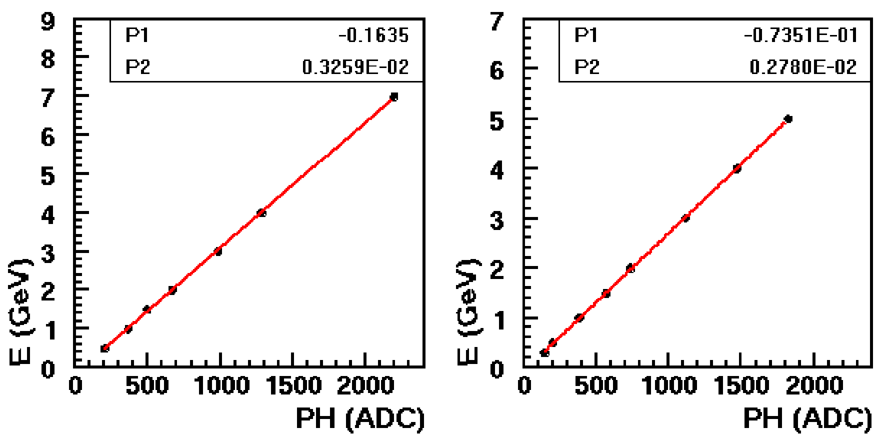

FIGURE 3.18. STEFI *(left)* and GENNI *(right)* linearity. P1 (P2) is C_0 (C_1).

	STEFI	**GENNI**
C_0 **[GeV]**	-0.1635	-0.07351
C_1 **[GeV/ADC]**	0.003259	0.002780

TABLE 3.7. Calorimeter calibration coefficients.

Furthermore, equation 3.13 allows to estimate a ~ 13 GeV (~ 11 GeV) single channel saturation energy for STEFI (GENNI). Since high-energy electrons produce large electromagnetic showers, the events that saturate one of the channels often share part of their deposited energy among adjacent crystals; if the shared energy lies below the saturation threshold, the adjacent channels produce few-GeV signals that slightly increase the total calorimeter energy value for such an event. Nevertheless, in this case there is no way to compute the true electron energy from the measured value. As the kinematic phase-space under study extends up to many tens of GeV (figure 2.7 bottom), this issue requires careful investigation: a detailed discussion on this topic will be given in subsection 4.7.3. Figure 3.19 shows the calorimeter energy resolutions as a function of the incoming electron energy, $\mathrm{res}_{\mathrm{calo}}(E_{\mathrm{calo}}) = \sigma(E_{\mathrm{calo}})/E_{\mathrm{calo}}$; it has been fitted with the function

$$\mathrm{res}_{\mathrm{calo}}(E_{\mathrm{calo}}) = \sqrt{\left(\frac{a}{\sqrt{E_{\mathrm{calo}}}}\right)^2 + c^2} \tag{3.14}$$

where $a/\sqrt{E_{\mathrm{calo}}}$ is the stochastic term, i.e. the contribution of the fluctuations in the physical development of the shower [125], and c is the constant term, which is related to the active volume geometry and non-uniformities [125] (values in table 3.8). As already mentioned, the STEFI and GENNI different mechanical structures result in a different performance; in particular, the GENNI compact structure (subsection 2.3.5.3) allows to achieve a ~ 5 times better resolution than STEFI, which has huge gaps between adjacent channels (subsection 2.3.5.2).

	STEFI	**GENNI**
a **[%$\sqrt{\text{GeV}}$]**	19.70	3.728
c **[%]**	15.13	2.428

TABLE 3.8. Calorimeters energy resolution terms.

3.6 Issues and software corrections

Many issues in the apparatus behaviour emerged while performing the tracking system alignment and the calorimeters calibration. Most of these issues resulted in predictable biases in the data, and therefore could be treated via software. In

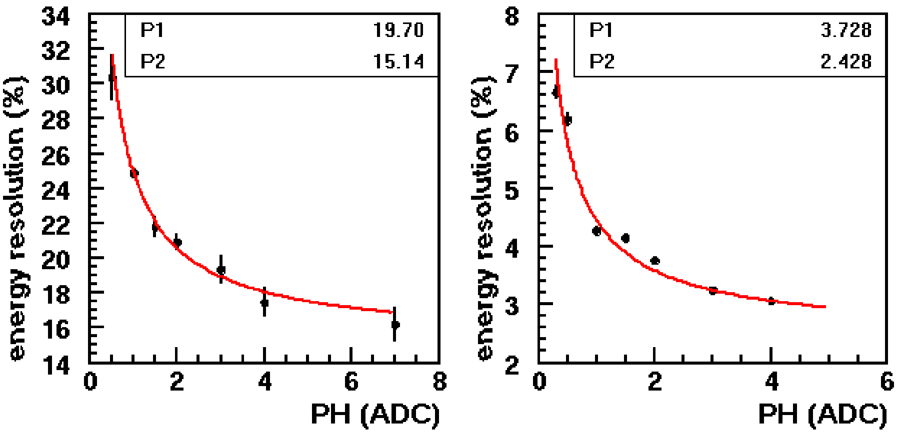

FIGURE 3.19. STEFI *(left)* and GENNI *(right)* energy resolution. P1 (P2) is the stochastic (constant) term.

the following, a detailed description of the software correction procedures will be given.

3.6.1 Malfunctioning silicon layers

As already mentioned, no offline treatment can be performed on setup 1 $1u$ and $10x$ layers, whose malfunctioning results in major inefficiencies in a non-negligible fraction of the active area. On the other hand, the $3y$ and $5y$ layers present single ASICs issues which result in local tens of µm shifts in the hit position reconstruction; the $3y$ and $5y$ issues have different causes and are described in subsections 3.6.1.1 and 3.6.1.2 respectively.
Inefficiency patterns and position reconstruction issues limited to small parts of the active area (single strips in most cases) are observed in all the tracking planes. Although their effect is small, it has been chosen not to include the malfunctioning regions in the alignment procedures: in order to exclude them, mask files have been produced (subsection 3.6.1.3).

3.6.1.1 $3y$ layer

Figures 3.20 and 3.21 show the $3y$ layer issues. In particular:

- the $(129, 256)$ channel region, i.e. the part of the sensor that is read out by the central ASIC, is less efficient than the rest of the sensor.
- The three ASICs regions present relative residual shifts one with respect to the other.

The first item results in a statistics loss that cannot be treated offline. This issue is related to the central ASIC CM distribution (figure 3.22), which is asymmetrical and much larger than those of the other ASICs. The residual shifts change

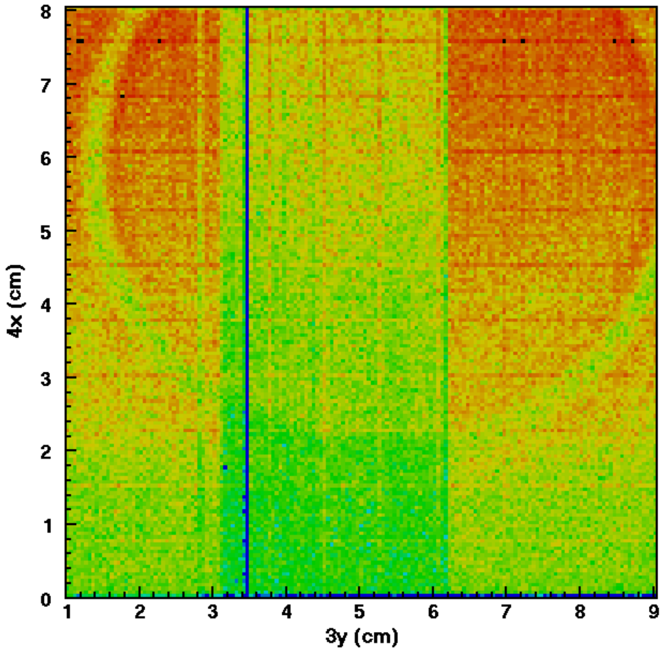

FIGURE 3.20. $(3y, 4x)$ hit point distribution: the $3y$ layer shows an efficiency loss in the $(129, 256)$ channel range (central vertical band).

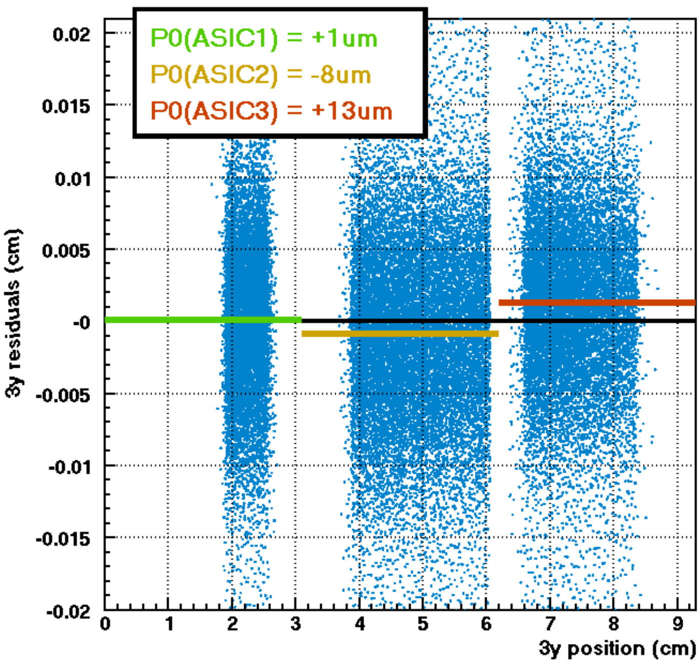

FIGURE 3.21. Setup 1 $(x_{3y}^{\text{meas }(0)}, \rho_{3y}^{(k)})$ scatter plot before the equation 3.15 corrections: the residual mean values of the three ASICs are shifted one with respect to the other.

over time: in particular, non-negligible relative shifts are only observed in the setup 1 configuration. The transformation

$$\begin{cases} x_{3y}^{\text{meas (0)}} \to x_{3y}^{\text{meas (0)}} + 8\ \mu\text{m} & \text{(ASIC 2)} \\ x_{3y}^{\text{meas (0)}} \to x_{3y}^{\text{meas (0)}} - 13\ \mu\text{m} & \text{(ASIC 3)} \end{cases} \tag{3.15}$$

is applied before the tracking system alignment.

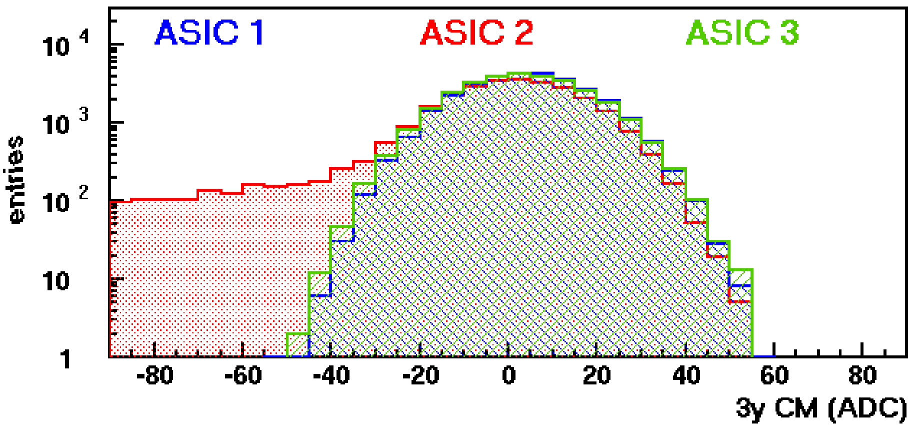

FIGURE 3.22. $3y$ layer CM distributions. The central ASIC distribution (red) clearly differs from those of the left (blue) and right (green) ASICs.

3.6.1.2 $5y$ layer

As shown in figure 3.23, the $5y$ layer central ASIC region has a ~ 60 µm bias, which can be treated with the transformation

$$x_{5y}^{\text{meas (0)}} \to x_{5y}^{\text{meas (0)}} - B_{5y}^{k} \qquad \text{(ASIC } k\text{)} \tag{3.16}$$

with the B_{5y}^{k} values reported in table 3.9.

k	setup 1 [µm]	setup 2a [µm]	setup 2b [µm]
1 (left)	−9	–	–
2 (central)	+62	+65	+60
3 (right)	–	–	–

TABLE 3.9. B_{5y}^{k} values. In setup 1 the relative shift between the left and right ASICs has also been corrected.

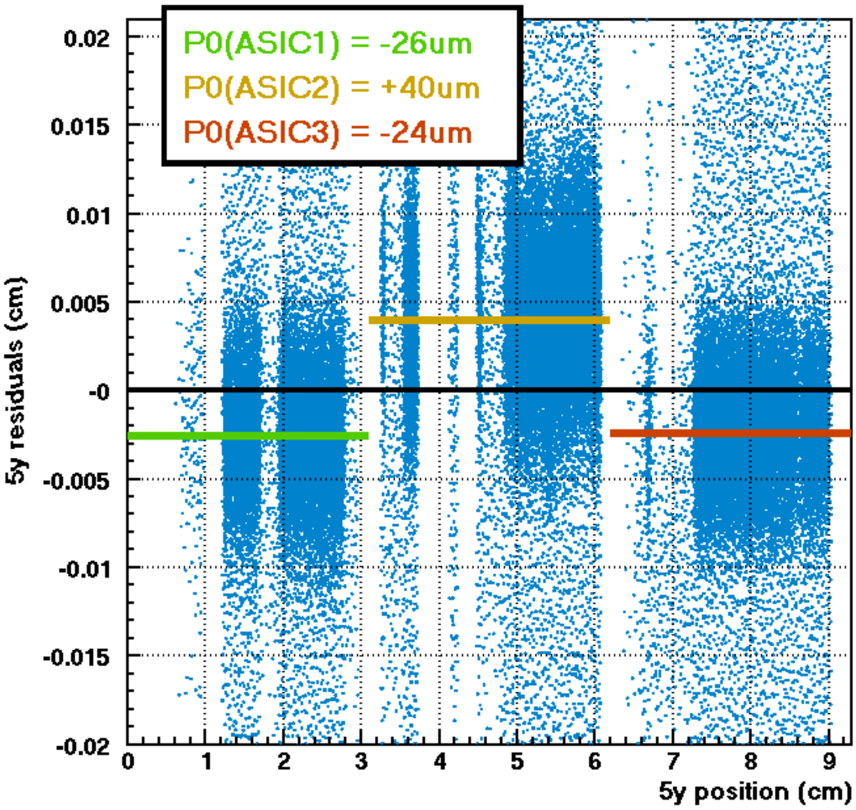

FIGURE 3.23. Setup 1 ($x_{5y}^{\text{meas}\ (0)}, \rho_{5y}^{(k)}$) scatter plot before the equation 3.16 corrections: a major shift in the central ASIC residual distribution is observed.

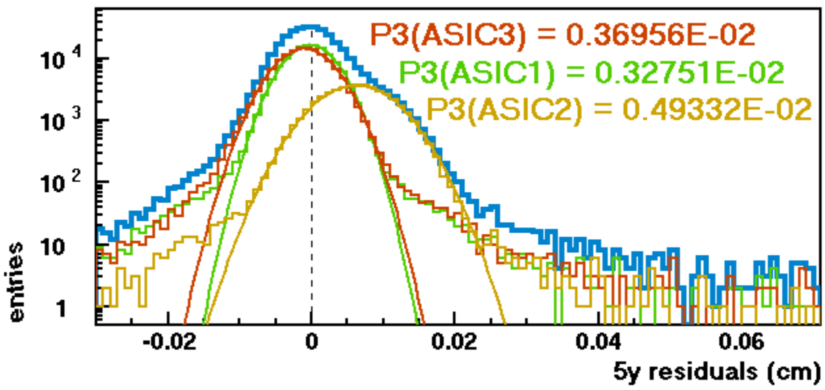

FIGURE 3.24. ρ_{5y} single-ASIC distributions before the equation 3.16 corrections. The hit point resolution values (P3) correspond to the Gaussian fit sigmas.

Furthermore, figure 3.24 shows that the hit point resolution in this region is $\sim$ 15 μm worse than in the rest of the sensor. This issue is a consequence of the central ASIC low gain: as shown in figure 3.25 the $5y$ layer signals are smaller than those of the other layers and thus a major fraction of the events that cross the floating strips is excluded by the zero suppression threshold, which makes the spatial resolution worse (see subsection 2.3.1).

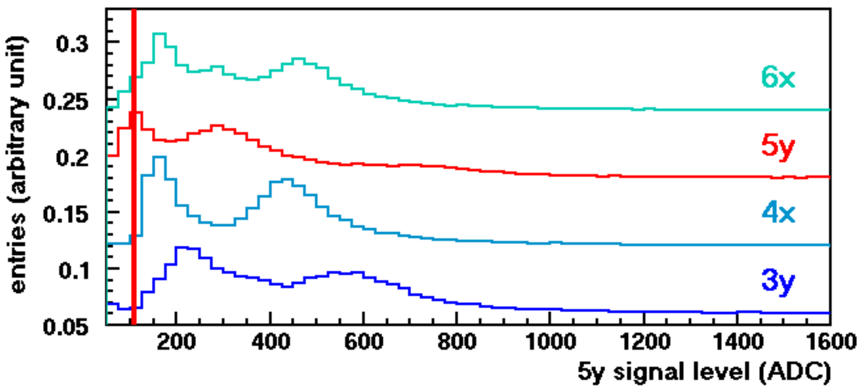

FIGURE 3.25. $5y$ layer charge spectrum. The $3y$, $4x$ and $6x$ layers spectra are shown for comparison. The lower (higher) peaks are due to the events that cross the floating (readout) strips.

3.6.1.3 Masks

Few-strip inefficiency and bias regions are observed in two cases:

- if one of the strips over which the cluster reconstruction algorithm loops is dead or has been excluded after the pedestal analysis, the resulting hit position will be biased (figure 3.26).
- Many strips, despite not having been marked as malfunctioning after the pedestal analysis, are inefficient.

Furthermore, the sensor edges have been excluded in order to limit the procedure to the reference pairs acceptance.
Mask files with the coordinates of all these malfunctioning regions ($\sim$ 9% of the overall active area in setup 1, $\sim$ 3% in setup 2) have been produced. Figure 3.27 shows an example of in-mask event exclusion applied to the DST data: since the latter have been produced with the multiplicity selection discussed in section 3.1, each layer beam profile is affected by the inefficiency patterns of the $2x$, $4x$, $5y$ and $6x$ layers.

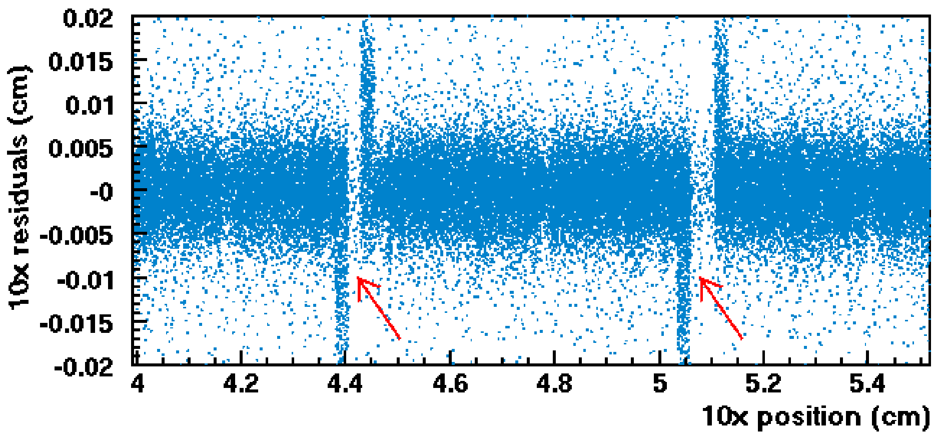

FIGURE 3.26. Example of biases in the cluster reconstruction near dead or excluded strips: if the cluster central strip is located to the left (right) with respect to the malfunctioning strip, the resulting hit position is underestimated (overestimated).

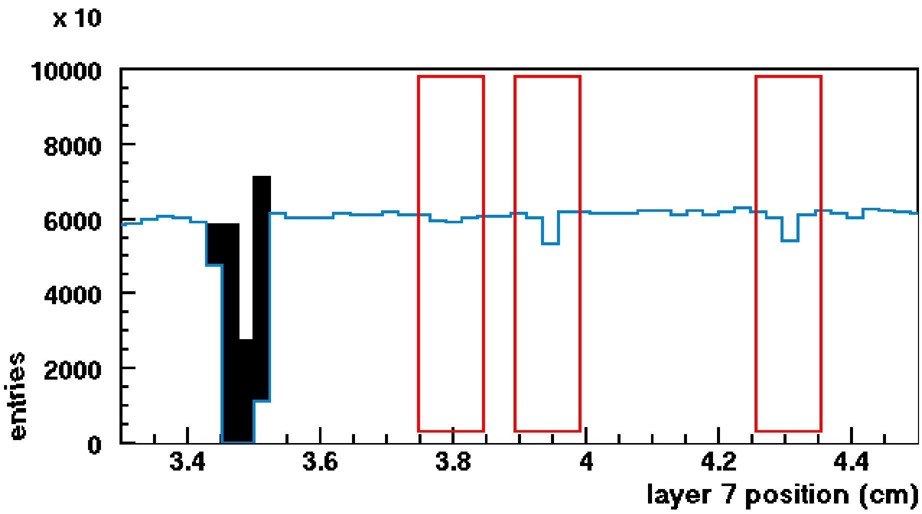

FIGURE 3.27. Example of tracking plane masks: the black events have been excluded; the red boxes indicate the inefficiency patterns introduced by the multiplicity selection performed on the $2x$, $4x$, $5y$ and $6x$ layers.

3.6.2 BGO-PMT coupling

GENNI was installed in the MUonE apparatus after the beamtest on the T9 PS beamline (appendix A). When the detector was moved to the COMPASS site, the mechanical crystal-PMT coupling changed, which affected each channel MIP peak position and hence its equalization coefficient (example in figure 3.28).

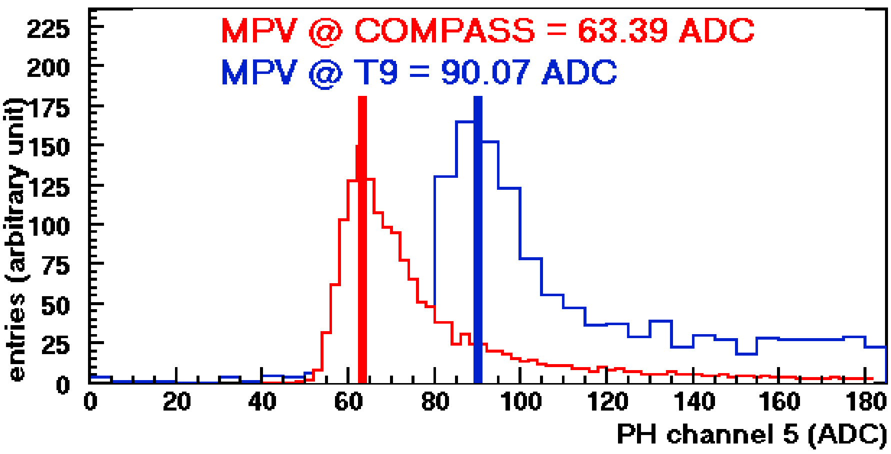

FIGURE 3.28. Change in the GENNI BGO-PMT coupling between the T9 and MUonE configurations.

Therefore, in order to apply the T9 calibration to the MUonE data, the transformation

$$\mathrm{PH}(i) \to \frac{90.07\ \mathrm{ADC}}{63.39\ \mathrm{ADC}}\mathrm{PH}(i) \tag{3.17}$$

must be performed; 90.07 ADC (63.39 ADC) is the central channel MIP peak position in the T9 (MUonE) case. The correction coefficient has already been taken into account in the values reported in table 3.6.

CHAPTER 4

The $\mu^{\pm}e^{-}$ scattering analysis

The offline tracking system alignment, calorimeter calibration and issue correction procedures presented in chapter 3 allow to achieve a high precision in the kinematics measurement and hence to keep the accuracy of the scattering analysis under control. This chapter exploits such methods to fulfill the MUonE 2018 run goal, i.e. to investigate the potential and the limits of studying the $\mu^{\pm}e^{-}$ elastic scattering with the apparatus described in chapter 2.
Before turning to the elastic kinematics analysis, the incident beam features have been studied. Furthermore, the small cross-section of the interaction under study and the large number of interfering processes required the development of many background rejection methods. As it will be shown in this chapter, these elastic candidate identification criteria lead to the selection of 134 ppm of the initial dataset.

4.1 The incident beam

The incident muon beam has a width of several tens of centimeters, much larger than the MUonE transverse acceptance. As shown in figure 4.1, the tracking system is out of the beam center along x, which was intentional in order to reduce the pile-up contribution due to the high-intensity beam region.
Looking at the beam angle distributions in figure 4.2 two observations can be made:

- there is a ~ 10 mrad (~ 5 mrad) tilt around the y (x) axis; this configuration improves the silicon detectors spatial resolution, since the fraction of the events whose signal is shared among adjacent strips increases [96].

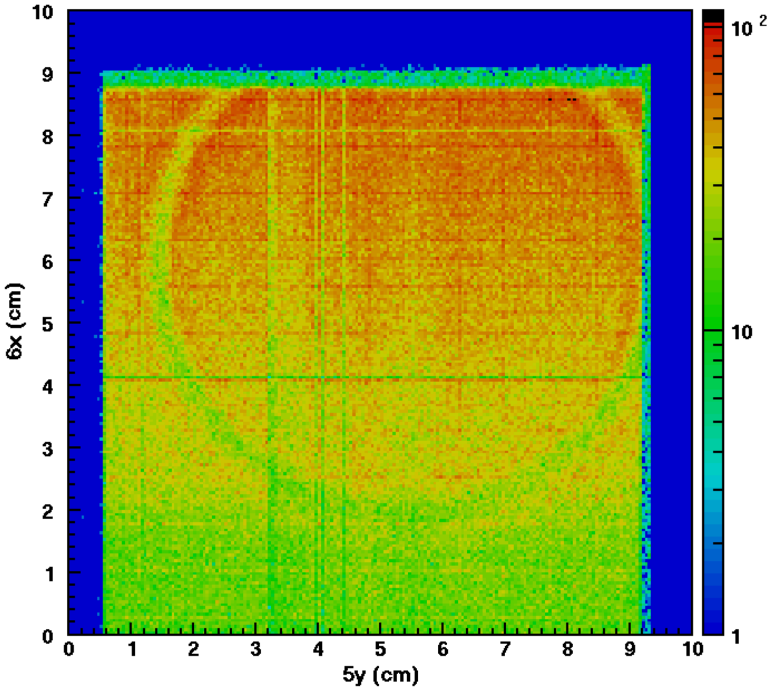

FIGURE 4.1. Input beam spot reconstructed by the $(5y, 6x)$ station.

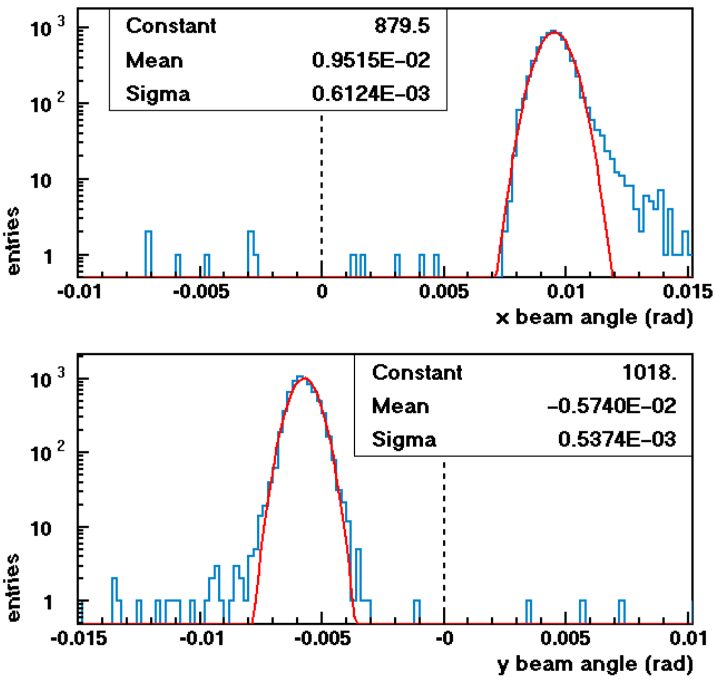

FIGURE 4.2. Typical beam input angles.

- The x (y) beam divergence is ~ 600 µrad (~ 500 µrad); these high values are due to the COMPASS multiple hadron absorption layers (subsection 2.1.1).

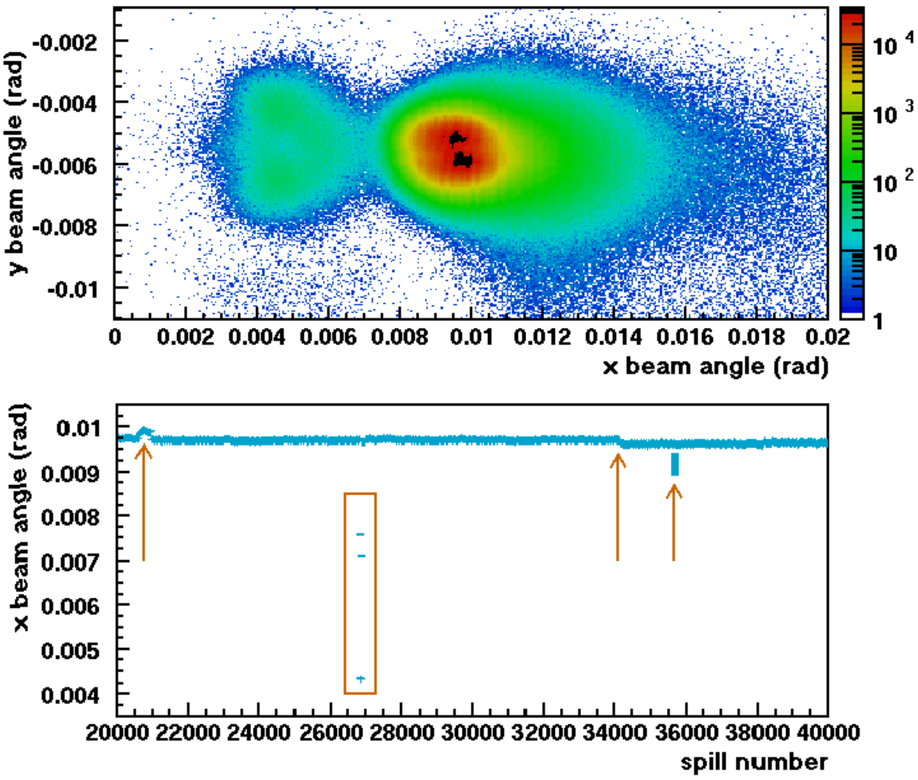

FIGURE 4.3. Input beam orientation changes over a 20000 spills measurement. *(top)* x-y angle phase-space; *(bottom)* x angle as a function of the spill number.

These distributions have been evaluated in a limited time range (~ 1000 spills) in which the beam was stable: indeed, albeit constant for most of the time, the beam orientation is observed to fluctuate of up to few-mrad (figure 4.3); such fluctuations might be due to the COMPASS target and magnetic fields changes and do not affect the MUonE physics analysis, since the scattering angles do not depend on the input beam orientation.
The input beam multiplicity (figure 4.4) has been evaluated using the $2x$ layer without the constraint of the DST files selection conditions (section 3.1). In the typical beam conditions, the single-hit events are $\sim 50\%$ of the overall statistics.

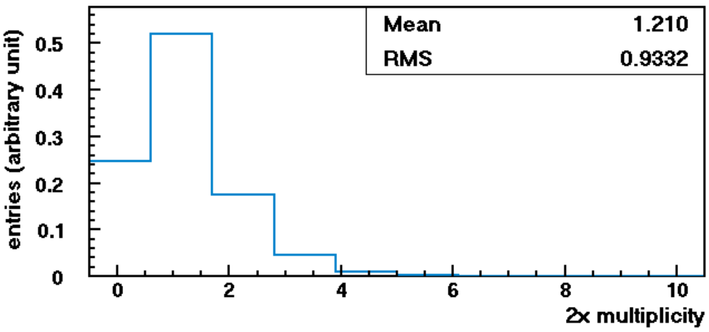

FIGURE 4.4. Typical beam input multiplicity. The zero-hit population includes events that have been triggered but have not been detected by the $2x$ layer due to acceptance limits or local inefficiencies.

4.2 Input tracking

The first step in the kinematics reconstruction is the input track analysis. The events that are single-hit in all the input station detectors are selected and linear fits are performed separately on the positions on the xz and yz planes. In the setup 1 case, the fit in the yz plane is performed first and the resulting track is projected to the $1u$ layer z; the x coordinate of the hit point on the latter is therefore found by means of a plane rotation of the positions along u and y and its error is calculated via propagation from σ_{1u} and the errors on the y fit parameters.

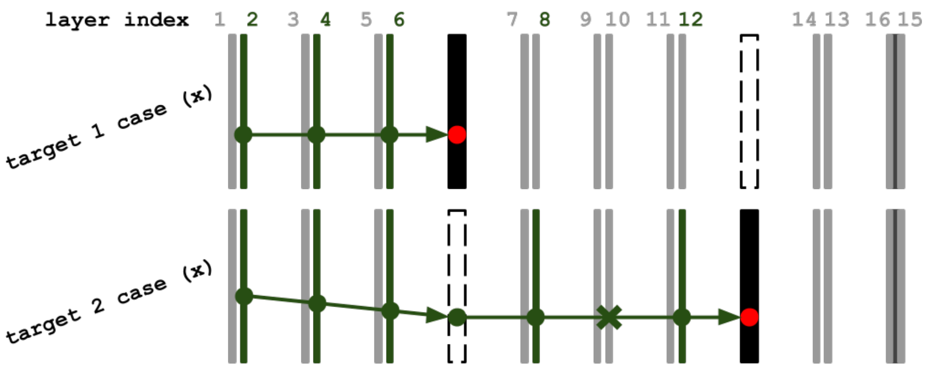

FIGURE 4.5. Input tracking in the target 1 *(top)* and 2 *(bottom)* cases.

When studying the downstream target, the same procedure is applied to the $(7y, 8x)$, $(9y, 10x)$ and $(11u, 12x)$ modules, with two differences:

- the malfunctioning $10x$ layer has been excluded from the track fit and its multiplicity is forced to be ≤ 1 instead of $= 1$.
- The input station track projections to the target 1 central z are included.

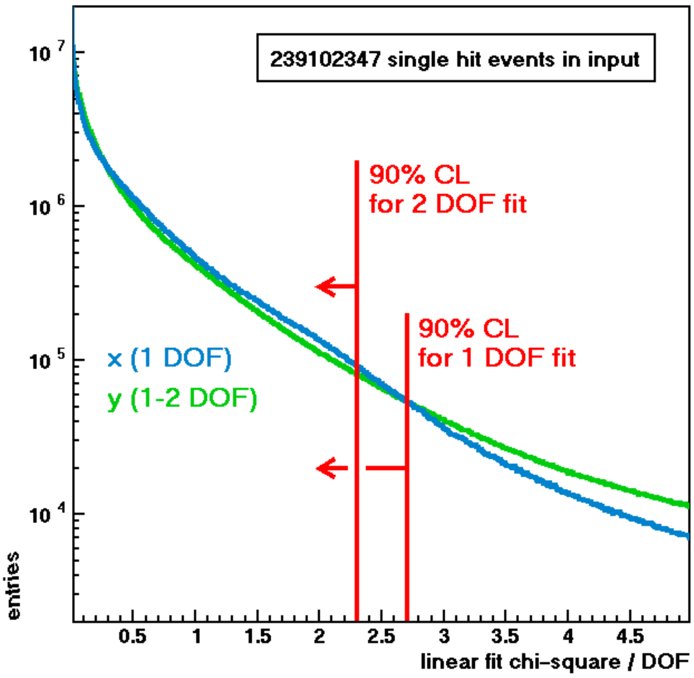

FIGURE 4.6. Input χ^2_{red} distributions.

The second item implies that the single-hit condition is required for all the tracking detectors that are located upstream with respect to target 2 (except the $10x$ layer). A comparison between the two configurations is shown in figure 4.5.
As already mentioned, the width of the residual distribution of the $\tilde{n}$-th layer $\sigma_{\tilde{n}}$ has been taken as the hit position error. In the linear fit case, the reduced chi-square is defined as [126]

$$\chi^2_{\text{red}} = \frac{1}{\text{DOF}} \sum_{\tilde{n}=1}^{N} \left[\frac{x^{\text{meas}}_{\tilde{n}} - (\tilde{m} z_{\tilde{n}} + \tilde{q})}{\sigma_{\tilde{n}}} \right]^2 \tag{4.1}$$

where N is the number of fitted points, $\tilde{m}$ ($\tilde{q}$) is the fit slope (intercept) and $\text{DOF} = N - 2$ is the number of degrees of freedom. The 90% CL limit, i.e. 2.71 (2.30) for DOF = 1 (2) [127], has been used as a threshold for the good track selection. The input χ^2_{red} distributions are shown in figure 4.6.
Table 4.1 shows the number of selected events per setup configuration: at this point, 213706546 good input fit events have been identified, i.e. $\sim 38\%$ of the

analyzed events, $\sim 87\%$ ($\sim 13\%$) of which enter the upstream (downstream) target. The target 2 good input statistics collected when both the targets were installed is $\sim 60\%$ of that of target 1: this is due to the larger number of layers on which the single-hit condition is required.

setup	calorimeter	target	input 1-hit events	good input fits
1	STEFI	1	33469895	30014414
1	STEFI	2	22166796	20935593
1	GENNI	1	24115982	20971478
1	GENNI	2	7091401	6607623
2a	GENNI	1	54465712	48805832
2b	GENNI	1	97792561	86371606

Table 4.1. Summary of the input analysis statistics.

4.3 Output topologies

The first level identification of the $\mu^{\pm}e^{-}$ elastic scattering candidates requires selection criteria based on the output multiplicity. If the criteria are too strict, the selection might be biased due to the tracking layers acceptance limits and inefficiency patterns; therefore, the minimal cuts that were needed to guarantee a non-negligible background rejection have been applied.
Different multiplicity conditions have been studied for both the upstream (figure 4.7 top) and downstream (figure 4.7 bottom) targets. However, there are some common features: In particular, for each view:

- the single- or double-hit condition is applied to the first output layer.
- The double-hit condition is applied to the following layer.

setup	calorimeter	target	lv. 2 selections
1	STEFI	1	335747
1	STEFI	2	450476
1	GENNI	1	247958
1	GENNI	2	159618
2a	GENNI	1	697844
2b	GENNI	1	1305649

Table 4.2. Summary of the level 2 analysis statistics.

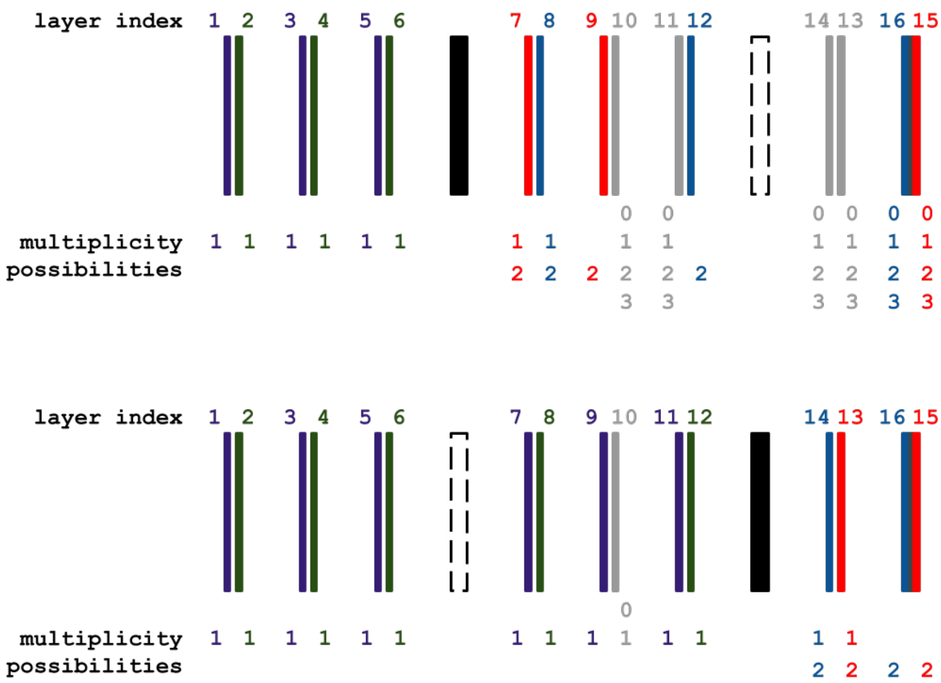

FIGURE 4.7. Target 1 *(top)* and 2 *(bottom)* output topology.

- The ≤ 3 multiplicity cut is applied to all the other output layers.

The first item details will be discussed in sections 4.4 and 4.6. The only exception to the second item is represented by the x view of the target 1 configuration: since the second output tracking plane would be the malfunctioning $10x$ layer, it has been chosen to set the double-hit condition on the $12x$ layer; this solution introduces many additional terms to the MCS overall contribution to the output electron track (section 4.6). The third item condition has been set in order to limit the (rare) high-multiplicity background that results from electromagnetic showers. Furthermore, as it will be shown in section 4.4, a limitation on the $(15y, 16x)$ station multiplicity optimizes the use of the latter for the output muon tracking in the target 1 case.
The events that have a good input track and match these output topology conditions are written in the second level DST files that are used for the kinematics analysis. The input raw positions are replaced with the fit parameters computed in double precision. Table 4.2 shows the size of these datasets: $\sim 0.6\%$ of the first level DST files has been selected, which allows to reduce the analysis running time from several days to less than ten minutes.

4.4 μ-e PID and pattern recognition

As shown in figure 4.7, the output tracking is performed with:

- the $7y$, $8x$, $9y$, $12x$, $15y$ and $16x$ layers and the input track projection, i.e. 3 or 4 points per view (there can be no hits in the $(15y, 16x)$ station), in the target 1 case;
- the $13y$, $14v$, $15y$ and $16x$ layers and the input track projection, i.e. 3 points per view, in the target 2 case.

The tracking system alignment correlates different view hit points (section 3.4); in case of multiple-hit events, all the possible combinations (whose number is equal to the product of the tilt correction partners multiplicities) must be computed. Therefore, the number of possible output tracks per view reduces to

$$N_{\text{fit}} = \begin{cases} M_{7y} \cdot M_{8v} + M_{9y} \cdot M_{12x} + M_{16x} & (x) \\ M_{7y} \cdot M_{8v} + M_{9y} \cdot M_{12x} + M_{15y} & (y) \end{cases} \tag{4.2}$$

for target 1 and

$$N_{\text{fit}} = \begin{cases} M_{13y} \cdot M_{14v} + M_{16x} & (x) \\ M_{13y} \cdot M_{14v} + M_{15y} & (y) \end{cases} \tag{4.3}$$

for target 2, where M_n is the n-th layer multiplicity. Equation 4.2 (4.3) shows that the event-by-event maximum number of possible output tracks (spectra in figure 4.8) is 48 (8); on the other hand, the minimum number of track possibilities is 4 in both cases.

An event-by-event identification of the physical tracks among all the possible combinations is required. Furthermore, since no PID system has been implemented in the MUonE apparatus[1], the μ-e disambiguation has to be performed by means of kinematics considerations: in most cases the electron is emitted at low energy (section 2.2) and hence the MCS heavily affects its motion; on the other hand, the ~ 190 GeV/c muon tracks show little deviations along the whole tracking system. Therefore, in typical conditions, the output muon track can be identified among all the possibilities as the one with the smallest deviations, i.e. the one that minimizes the linear fit χ^2_{red}; once the muon track has been found, the output double-hit layers unambiguously identify the electron track as well.

This PID method works for $\theta_\mu < \theta_e$ while it can lead to a μ-e misidentification if $\theta_\mu \gtrsim \theta_e$, i.e. $\theta_e \lesssim 3$ mrad: in this case the MCS contribution to the high-energy electron track is similar to or larger than the one of the muon track, thus making the identification ambiguous for 2 mrad $\lesssim \theta_e \lesssim 3$ mrad and wrong for $\theta_e \lesssim 2$ mrad. A way to solve such an ambiguity is currently under study.

[1]The use of the calorimeter single channels to perform the PID has been considered and is currently under study; however, the limited transverse acceptance and the crosstalk between adjacent crystals impose strict limitations to this approach.

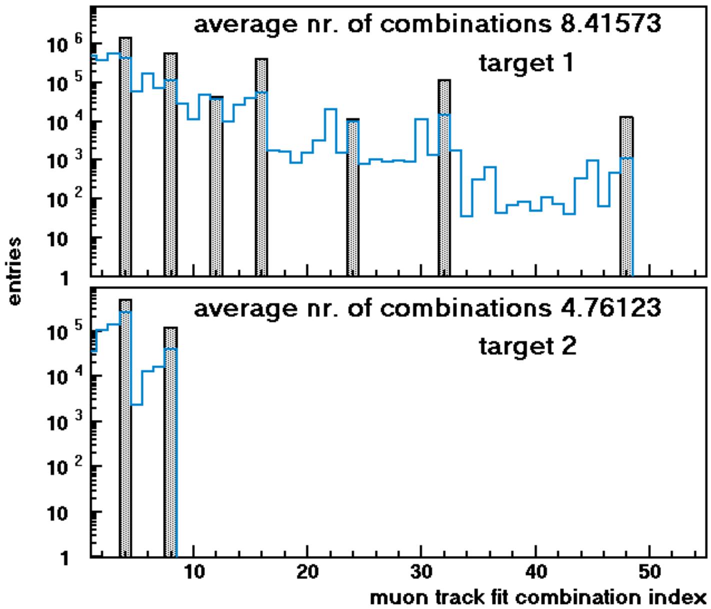

FIGURE 4.8. Spectra of the maximum number of possible output tracks (black) and of the least-$\chi^2_{\rm red}$ track index (light blue).

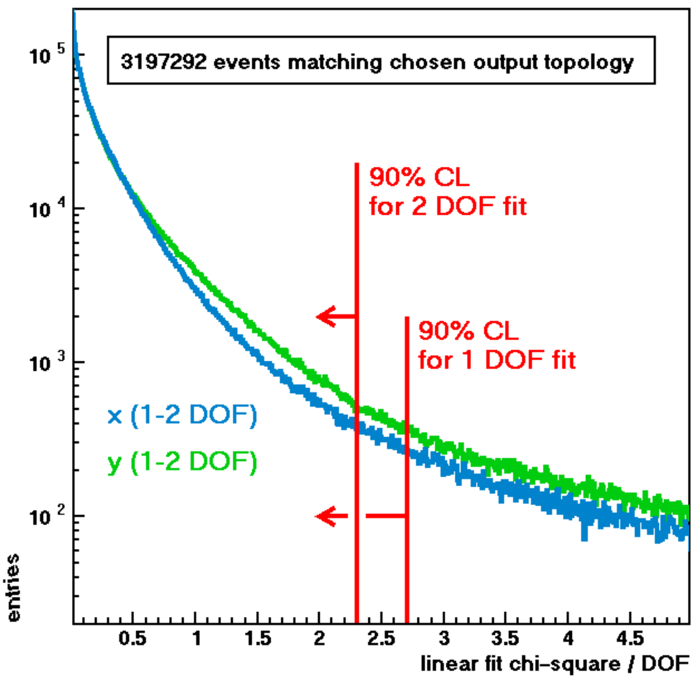

FIGURE 4.9. Output muon least-$\chi^2_{\rm red}$ distributions.

The muon track least-χ^2_{red} distributions are shown in figure 4.9. The 90% CL cut has been applied (section 4.2) in order to limit the background contamination given by those events in which only two low-energy particles (whose possible origins are summarized in section 2.2) are detected.
In general, the MCS makes the electron deviate by several tens of mrad and hence the μ-e kinematic correlation is broken after the crossing of few silicon layers. The electron track determination has therefore been performed using the output layers that are closest to the targets. In particular, in the target 1 (2) case:

- if $M_{7y} = M_{8x} = 2$ ($M_{13y} = M_{14v} = 2$) the electron hit point in the $(7y, 8x)$ ($(13y, 14v)$) module is unambiguously determined; the electron track is therefore reconstructed connecting the latter to the interaction point inside the target.
- If $M_{7y} = 1$ or $M_{8x} = 1$ ($M_{13y} = 1$ or $M_{14v} = 1$) the next pair of tracking planes ($10x$ and $11u$ excluded), whose multiplicities have been forced to be 2, are used, together with the target interaction point.

The second item has been included to remove the limit to the tracking system angular acceptance given by two particles that hit the first output layer at a $\lesssim 3\ w_{\text{ro}}$ relative distance, thus being identified as a single particle. However, as it will be shown in section 4.6, such a single-hit population includes a major fraction of background events, therefore it has been excluded from the final analysis.
The input ($m^{\text{in}}_{x,y}$) and output ($m^{e}_{x,y}$ and $m^{\mu}_{x,y}$) track slopes are used to evaluate the so-called direction cosines [128, 129]

$$\cos\theta_j = \frac{m^{\text{in}}_x m^j_x + m^{\text{in}}_y m^j_y + 1}{\sqrt{[(m^{\text{in}}_x)^2 + (m^{\text{in}}_y)^2 + 1][(m^j_x)^2 + (m^j_y)^2 + 1]}} \tag{4.4}$$

where $j = \mu, e$. The scattering angles θ_μ and θ_e are determined from equation 4.4.

4.5 Coplanarity

According to the special relativity, the elastic scattering input and output states are coplanar, i.e. the three tracks lie on the same plane [130]. The interaction plane and the unit vectors $\widehat{u}^{\text{in}}$, $\widehat{u}^{e}$ and $\widehat{u}^{\mu}$ that define the three tracks are represented in figure 4.10. Given the fact that $\widehat{u}^{\text{in}} \times \widehat{u}^{e}$ is orthogonal to the plane defined by $\widehat{u}^{\text{in}}$ and $\widehat{u}^{e}$, the process coplanarity implies that [128]

$$\widehat{u}^{\mu} \cdot \left(\widehat{u}^{\text{in}} \times \widehat{u}^{e}\right) = \left(u^\mu_x \widehat{x} + u^\mu_y \widehat{y} + u^\mu_z \widehat{z}\right) \cdot \begin{vmatrix} \widehat{x} & \widehat{y} & \widehat{z} \\ u^{\text{in}}_x & u^{\text{in}}_y & u^{\text{in}}_z \\ u^e_x & u^e_y & u^e_z \end{vmatrix} = 0 \tag{4.5}$$

where $\widehat{x}$, $\widehat{y}$ and $\widehat{z}$ are the reference axes unit vectors. In practice, the track unit vectors are given by

$$\widehat{u}^j = \left(u_x^j\widehat{x} + u_y^j\widehat{y} + u_z^j\widehat{z}\right) = \frac{1}{\sqrt{(m_x^j)^2 + (m_y^j)^2 + 1}}\left(m_x^j\widehat{x} + m_y^j\widehat{y} + \widehat{z}\right) \tag{4.6}$$

where $j = \text{in}, \mu, e$. By introducing the coplanarity angle

$$\vartheta_{\text{cop}} = \arccos\left[\widehat{u}^\mu \cdot \left(\widehat{u}^{\text{in}} \times \widehat{u}^e\right)\right] \tag{4.7}$$

equation 4.5 reduces to $\vartheta_{\text{cop}} = \pi/2 \sim 1.570796$.

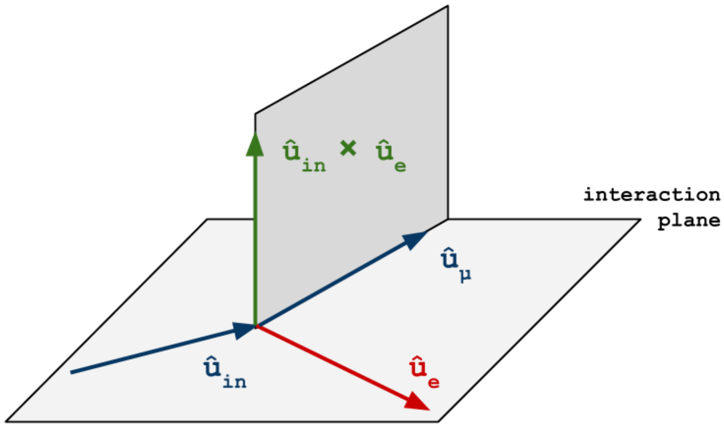

FIGURE 4.10. Coplanarity of the $\mu^\pm e^-$ elastic scattering states.

Equations 4.5, 4.6 and 4.7 give a criterion to identify and exclude the inelastic events, whose states are in general not coplanar. Figure 4.11 shows the distribution of the coplanarity angle ϑ_{cop}, which consists of a narrow, symmetric peak whose mean value is fully compatible with $\pi/2$. This result represents a first check of both the alignment goodness and the tracking system sensitivity to the elastic scattering kinematics.
The selections on χ^2_{red} and ϑ_{cop} allow a first level background rejection: more than 14% of the events that have the right output topology are excluded and the kinematic curve $\theta_\mu(\theta_e)$ is clearly visible for $\theta_e > 3$ mrad (figure 4.12).

4.6 Electron-positron pairs, δ-rays and MCS

Figure 4.12 shows a background band in the $\theta_\mu \lesssim 0.5$ mrad region that is more than 10 times more populated than the lower part of the angle-angle kinematic curve and hence covers it. Such events are characterized by

- good output muon tracks with small scattering angles;

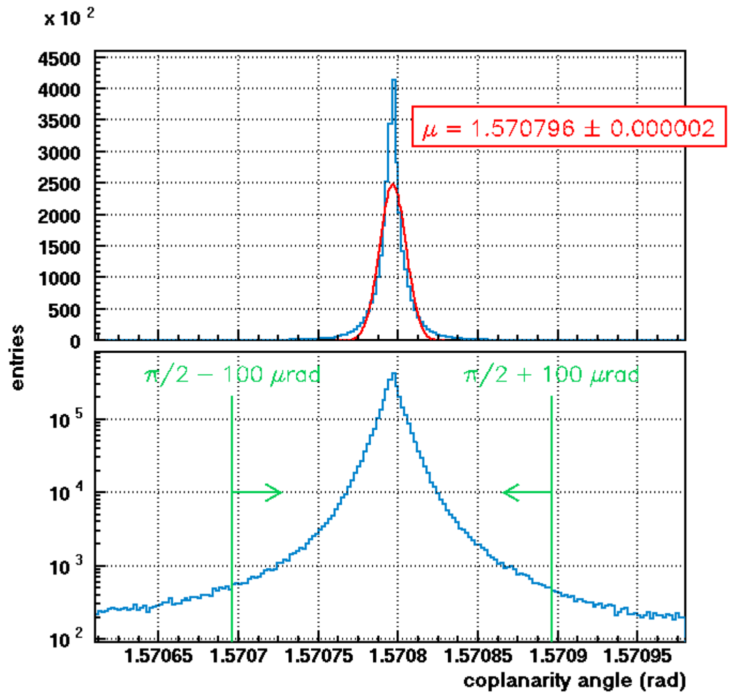

FIGURE 4.11. Coplanarity angle distribution in linear *(top)* and logarithmic *(bottom)* scale. The coplanarity cut range is shown in green.

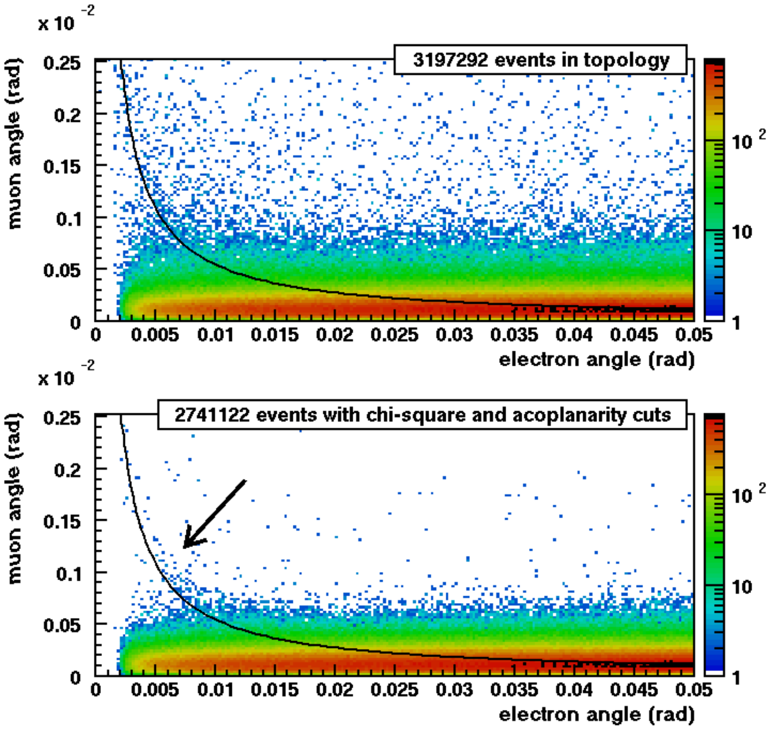

FIGURE 4.12. (θ_μ, θ_e) phase-space with all the events in the second level DST files *(top)* and after the first level background rejection *(bottom)*. The black curve represents the theoretical prediction for 187 GeV input muons.

- electron angles in a several tens of mrad range and without the $\theta_\mu(\theta_e)$ elastic correlation;
- coplanarity angle within the selection range;
- a continuous total energy spectrum that extends up to ~ 15 GeV.

This band mainly consists of non-elastic output states that include a high-energy muon and an electron; the latter can be either a δ-ray or a high-energy electron (or positron) from a pair – see section 2.2. These output electrons can be generated in the carbon targets, in the silicon tiles or in the air.
Most of the background band can be excluded by means of spatial considerations. As shown in figure 4.13, only the electrons that are produced inside the carbon targets can be elastic candidates, while the events that originate elsewhere and in which the muon experiences little-to-no deviation have to be rejected.

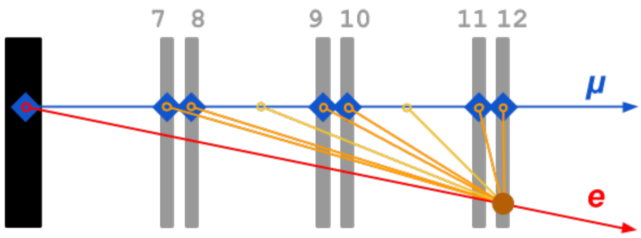

FIGURE 4.13. Kinematics of the non-elastic muon-electron output states. The red track represents an electron emerging from the carbon target, while the orange (yellow) tracks represent electrons produced in the silicon (air).

This rejection is performed by imposing a stricter multiplicity selection to the output silicon layers: in the target 1 (2) case, only the events with $M_{7y} = M_{8x} = 2$ ($M_{13y} = M_{14v} = 2$) are selected. The $(7y, 8x)$ $((13y, 14v))$ hit is used to determine the electron output track, which is then projected to the $9y$ and $12x$ ($15y$ and $16x$) planes; a hit point on the latter is searched within a region whose center is set by the track projection and whose limits are evaluated by considering the electron MCS (figure 4.14).
The overall MCS contribution has been evaluated taking into account

- the silicon layers (subsection 2.3.1);
- the carbon targets (~ 4 mm, i.e. $\sim 0.0207039X_0$);
- the $(15y, 16x)$ module tungsten tile (subsection 2.3.1) in the $15y$ layer case.

The air contribution has been found to be negligible. Each term has been evaluated with equation 2.8 using $\beta pc \sim E$ and the energy values reported in table 4.3. Adding the terms in quadrature results in a systematic underestimation of the overall MCS contribution [2]. Therefore, for the sake of conservativeness, the

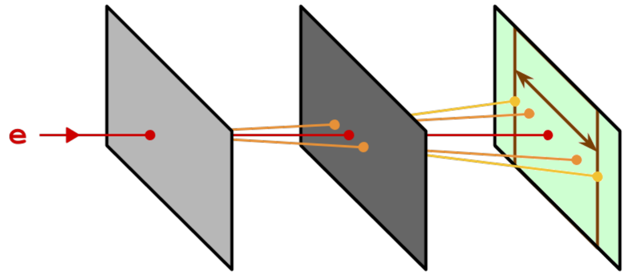

FIGURE 4.14. MCS contributions to the electron track along x. The orange (yellow) contribution is given by the upstream (downstream) bulk layer. The overall contribution at the green plane z is represented by the brown lines.

simple sum of the terms has been used. The width of the final selection regions ranges from ~ 200 µm (for $\gtrsim 10$ GeV electrons) to ~ 1 cm (for lowest-energy electrons and for the electrons that are out of the calorimeter acceptance).

calorimeter energy	**energy in the MCS evaluation**
< 0.5 GeV	0.2 GeV
$(0.5, 1)$ GeV	0.5 GeV
$(1, 2)$ GeV	1 GeV
$(2, 5)$ GeV	2 GeV
$(5, 10)$ GeV	5 GeV
> 10 GeV	10 GeV
at saturation	10 GeV

TABLE 4.3. Energy threshold values for the electron MCS evaluation. If the electron is out of the calorimeter acceptance the lowest threshold is assigned, which corresponds to the widest hit search region.

This selection allows to reject most of the background events in the low-θ_μ band (section 4.7). However, as already mentioned, the double-hit requirement in the $7y$ and $8x$ (or $13y$ and $14v$) layers introduces a lower limit to the $\theta_\mu + \theta_e$ angle. In particular:

- in the target 1 case, the setup 1 distance between the carbon tile and the first output tracking module results in a ~ 6 mrad limit; the setup 2 longer lever arm reduces this limit to ~ 3 mrad.
- In the target 2 case, a ~ 6 mrad limit is computed.

As a consequence of these limits, the different data samples are not homogeneous in the signal region and hence have to be considered separately when evaluating the elastic scattering cross section.

4.7 Scattering kinematics

Table 4.4 shows the number of elastic candidates identified in each configuration. The overall candidates are 134 ppm of the initial data sample and this fraction is < 150 ppm in all the configurations. Three observations can be made:

- as already mentioned, target 2 candidates are less than the target 1 candidates found in the same data sample, because of the stricter input conditions.
- Increasing the output lever arm in setup 2 (subsection 2.3.4) resulted in an improvement of the small-angle acceptance; indeed, the fraction of elastic candidates increased from ~ 70 ppm to ~ 140 ppm.
- Most of the elastic candidates ($\sim 68\%$) have been identified in the latest and most favorable configuration; therefore, any preliminary approach to the evaluation of the elastic scattering cross section should be limited to this dataset.

setup	calorimeter	target	elastic candidates	in lv. 1 DST files
1	STEFI	1	8813	82.8 ppm
		2	6655	62.5 ppm
	GENNI	1	5988	62.3 ppm
		2	2054	44.6 ppm
2a		1	17833	149.5 ppm
2b			32810	142.1 ppm
total			74153	134.1 ppm

Table 4.4. Summary of the elastic candidate statistics.

As it will be shown in the following subsections, most of the background is excluded from the final elastic candidate dataset, and both the angle-angle and the angle-energy kinematic curves are clearly observed. Furthermore, the calorimeter data allow to separate the elastic events from the background left in the signal region. The 2018 apparatus has therefore proven to be suitable for the $\mu^{\pm}e^{-}$ elastic scattering measurement.

4.7.1 Angle-angle phase-space

Figure 4.15 shows the final elastic candidates in the (θ_e, θ_μ) phase-space. Many important conclusions can be drawn:

- despite the major background rejection, a small fraction of non-elastic events is still present (yellow arrow); this population consists of electrons

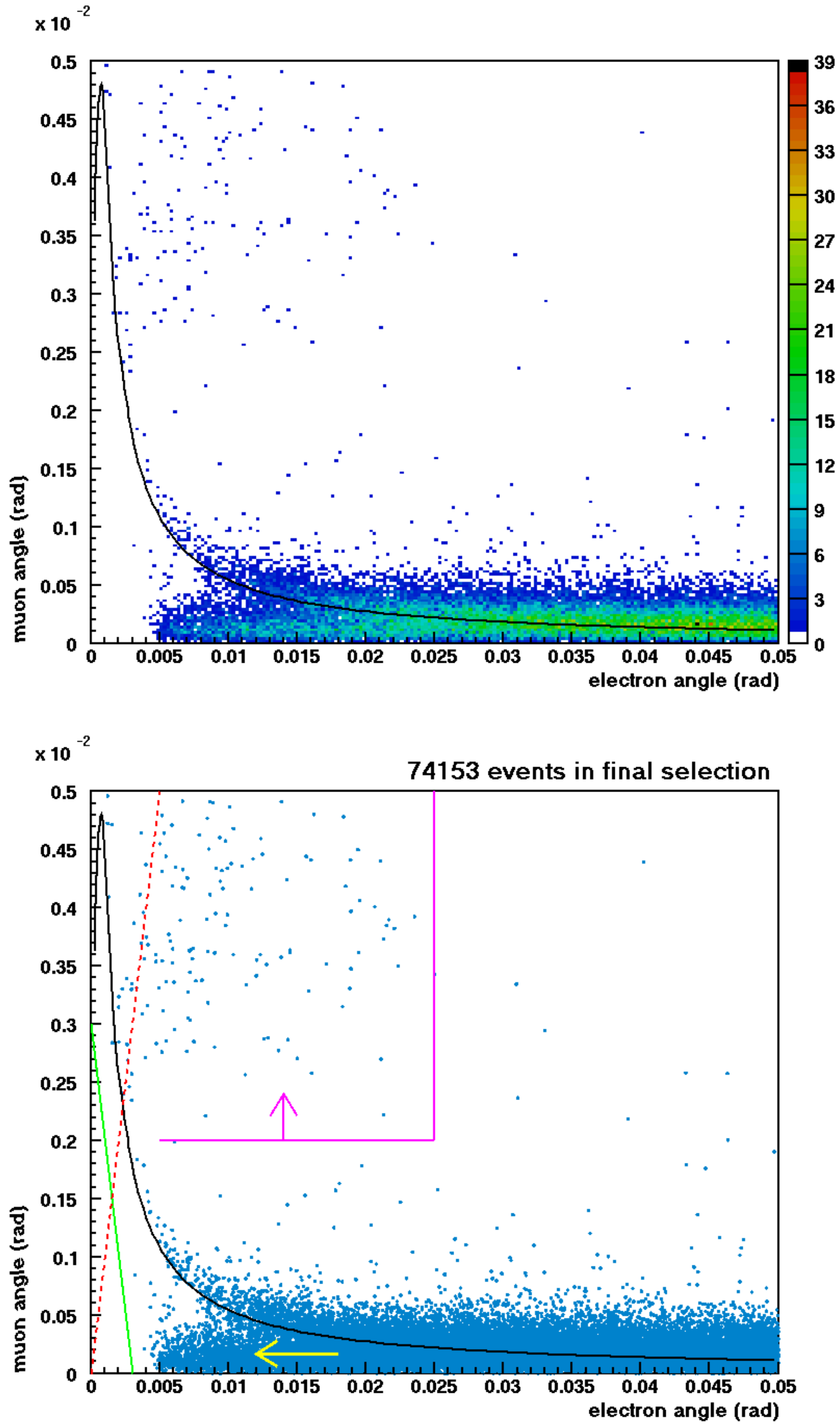

FIGURE 4.15. (θ_e, θ_μ) phase-space with the elastic candidates; colorscale *(top)* and event-by-event *(bottom)* scatter plot. The red dashed line represents the bisector. The green line represents the expected ~ 3 mrad small-angle acceptance limit.

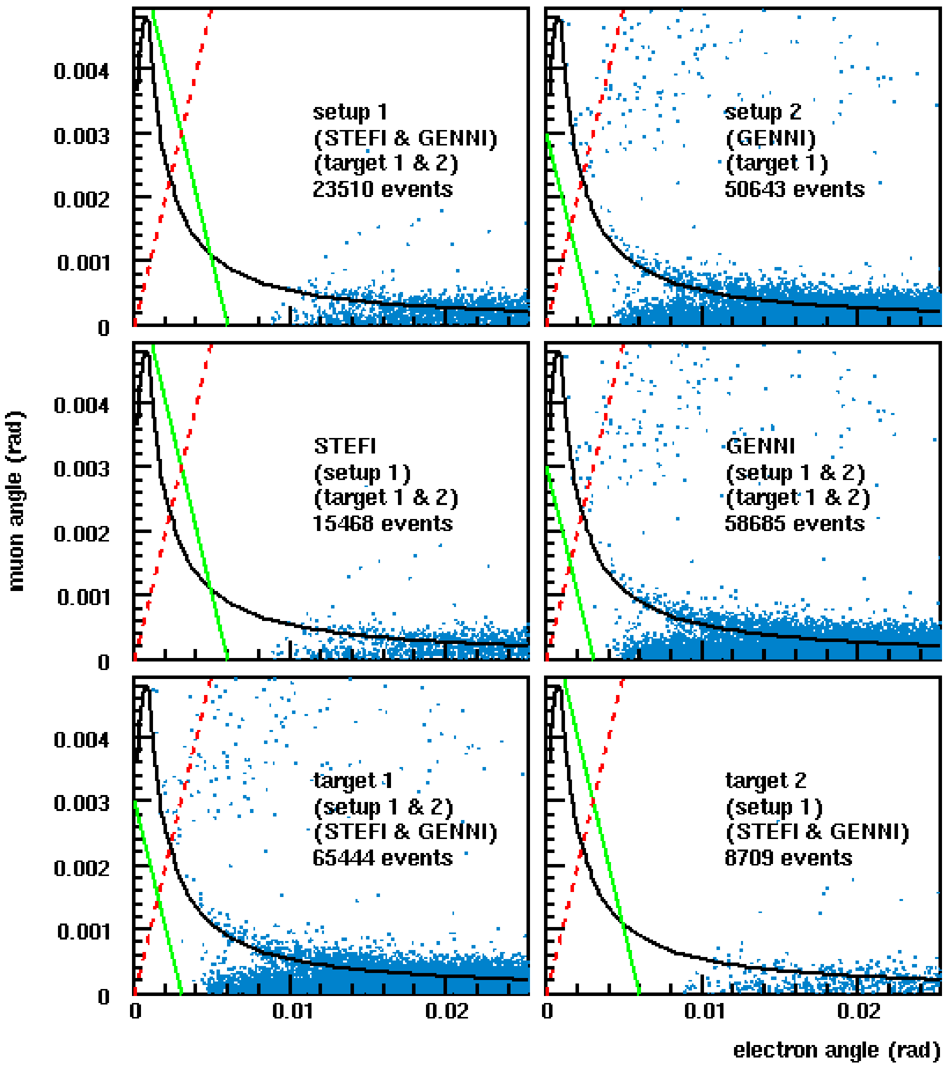

FIGURE 4.16. (θ_e, θ_μ) phase-space in the different apparatus configurations. In the setup 1 cases the shorter output lever arm results in a higher angular acceptance limit, which cuts the signal region of the $\theta_\mu(\theta_e)$ curve off. The large-angles population is only present in the setup 2 configurations.

that originate inside the carbon targets and hence present the same track pattern as the elastic ones. However, since in the low-θ_e region such background events typically have lower energy, the calorimeter information can be exploited to exclude them (subsection 4.7.2).

- A comparison with the distributions in figure 4.12 shows the small-angle acceptance reduction; indeed, while in the former the phase-space population with $\theta_\mu \sim 0$ mrad extends down to $\theta_e \sim 2$ mrad, no events populate the $\theta_e + \theta_\mu \lesssim 4$ mrad region in figure 4.15, which is slightly worse than the expected limit (green line). As shown in figure 4.16 the setup 1 limit is ~ 8 mrad (a ~ 6 mrad limit was expected): in this case, the whole elastic signal region is cut off, therefore no cross section evaluation can be performed.

- The measured $\theta_\mu(\theta_e)$ curve is slightly higher than the theoretical prediction; however, the latter has been drawn under the assumption of 187 GeV incident muons, which might represent an overestimation of the effective input energy.

- There are ~ 200 events out of the kinematic curve in the region in which $\theta_e \lesssim 25$ mrad and $\theta_\mu \gtrsim 2$ mrad (purple lines).

While the low-θ_μ background events match the simulations predictions [91], the events mentioned in the last item are unexpected and are currently under study (subsection 4.7.4). Some of these events might result from the electron-muon misidentification (subsection 4.4), but the latter cannot be responsible for those with $\theta_e \gtrsim 5$ mrad, which would be moved above the theoretical curve maximum by a θ_μ-θ_e swap.
It is clear from the comparison of the (θ_e, θ_μ) phase-space reconstructed in the different apparatus configurations that the large-angles population is only present in the setup 2 case. The calorimeter information might prove to be useful in the classification of these events – subsection 4.7.2.

4.7.2 Angles and energy

$\sim 54\%$ ($\sim 65\%$) of the events in the first level DST files produced a signal in the STEFI (GENNI) calorimeter. The energy spectra are shown in figure 4.17. As already mentioned, if one of the calorimeter channels saturates, the information on the total energy is incomplete; in this case, since the single-channel saturation energy is approximately the same for all the channels (section 3.5), the result of equations 3.12 and 3.13 populates an unphysical peak (black boxes in figure 4.17) in the spectrum. However, such events can be identified and excluded: in the physics analysis, it has been chosen to flag the calorimeter-saturating events with a 100 GeV energy value, which is several tens of GeV above the spectra end points. A dedicated study has been performed on these events (subsection 4.7.3).

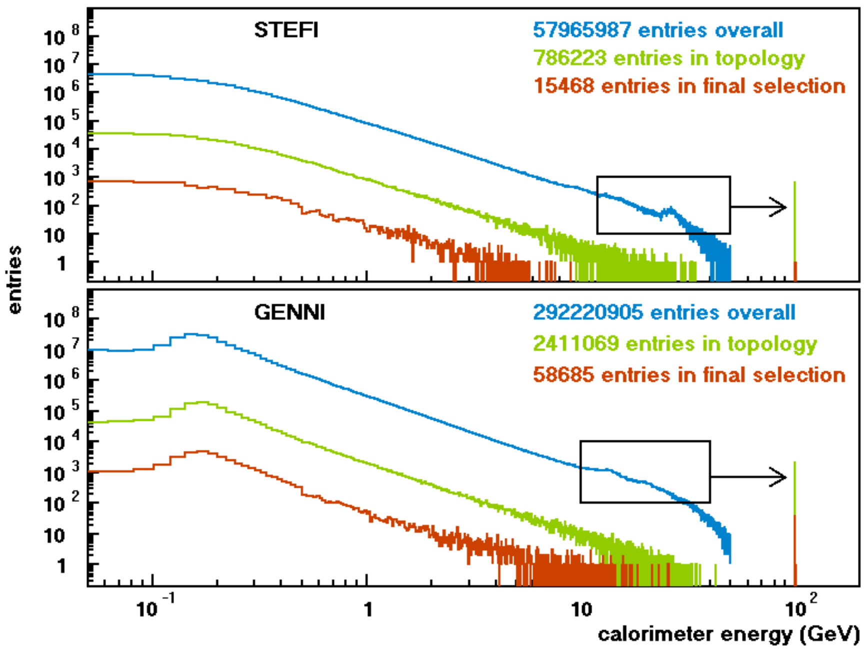

FIGURE 4.17. STEFI *(top)* and GENNI *(bottom)* energy spectra of the first level DST files (blue), of the second level DST files (green) and of the elastic candidates (red). The channel-saturating total energy (black boxes) is forced to 100 GeV in the second level dataset.

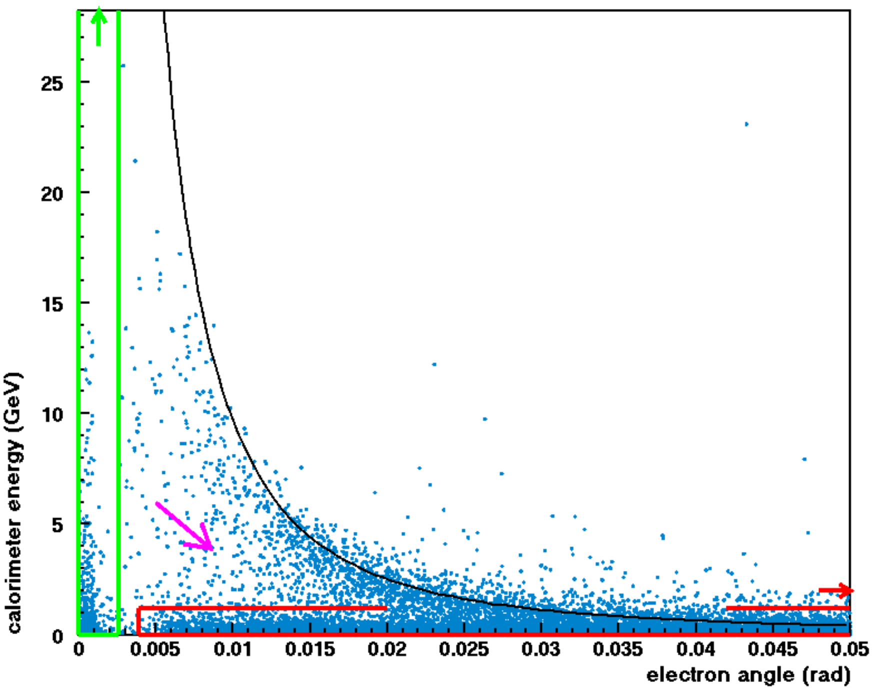

FIGURE 4.18. $(\theta_e, E_{\text{calo}})$ phase-space with the elastic candidates.

Since the contribution of the muons to the overall energy measured by the calorimeter is small ($\lesssim 200$ MeV), the total value E_{calo} corresponds approximately to the electron energy E_e^{f} and therefore $E_e^{\text{f}}(\theta_e) \sim E_{\text{calo}}(\theta_e)$. Looking at the $(\theta_e, E_{\text{calo}})$ phase-space in figure 4.18 many observations can be made:

- leaving aside the calorimeter-saturating events, the highest energy of the elastic candidates is 26 GeV.
- The measured elastic curve is slightly lower than the theoretical prediction (black curve); this might indicate an overestimation of the input muon energy, which has already been addressed in subsection 4.7.1 when studying the $\theta_e(\theta_\mu)$ curve.
- The low-energy ($\lesssim 1$ GeV), $\theta_e \gtrsim 4$ mrad population (red box) mainly corresponds to the low-θ_μ background band identified in subsection 4.7.1; this might allow to define a criterion for the elastic and background event separation in the signal region.
- There are ~ 800 events with $\theta_e \lesssim 2.5$ mrad (green box); since the low-θ_e region shown in the (θ_e, θ_μ) plots (figures 4.15 and 4.16) is empty, these events have $\theta_\mu > 5$ mrad, i.e. they are out of the elastic phase-space.
- There are many events in the region between the elastic curve and the low-energy background band for $\theta_e \lesssim 20$ mrad (purple arrow).

Background rejection methods for the treatment of the last three items are being developed. Subsection 4.7.4 provides a description of the current status of this analysis.
Figure 4.19 shows a comparison between the different configurations results. All the setup 1 distributions (setup 1, STEFI and target 2 plots) show a cutoff above ~ 10 GeV, which is not due to the calorimeter energy range but instead to the small-angle acceptance limit; indeed, the latter is too high for the signal region to be accessed in the setup 1, STEFI and target 2 cases (figure 4.16).
The two scattering angles and the calorimeter information are put together in the three-dimensional $(\theta_e, \theta_\mu, E_{\text{calo}})$ phase-space, which is shown in figure 4.20. Only the events with > 0.5 GeV energy are included. However, as it will be shown in subsection 4.7.4, this cut excludes many elastic events whose energy has not been measured. Table 4.5 shows the statistics reduction introduced by the energy selections.

4.7.3 Calorimeter-saturating events

Table 4.5 shows that there are 41 events in which the signal of at least one calorimeter channel is saturated. Given the fact that the saturation only occurs when a huge amount of energy is lost in the detector, this condition indicates the presence of a several tens of GeV electron among the output particles. Although

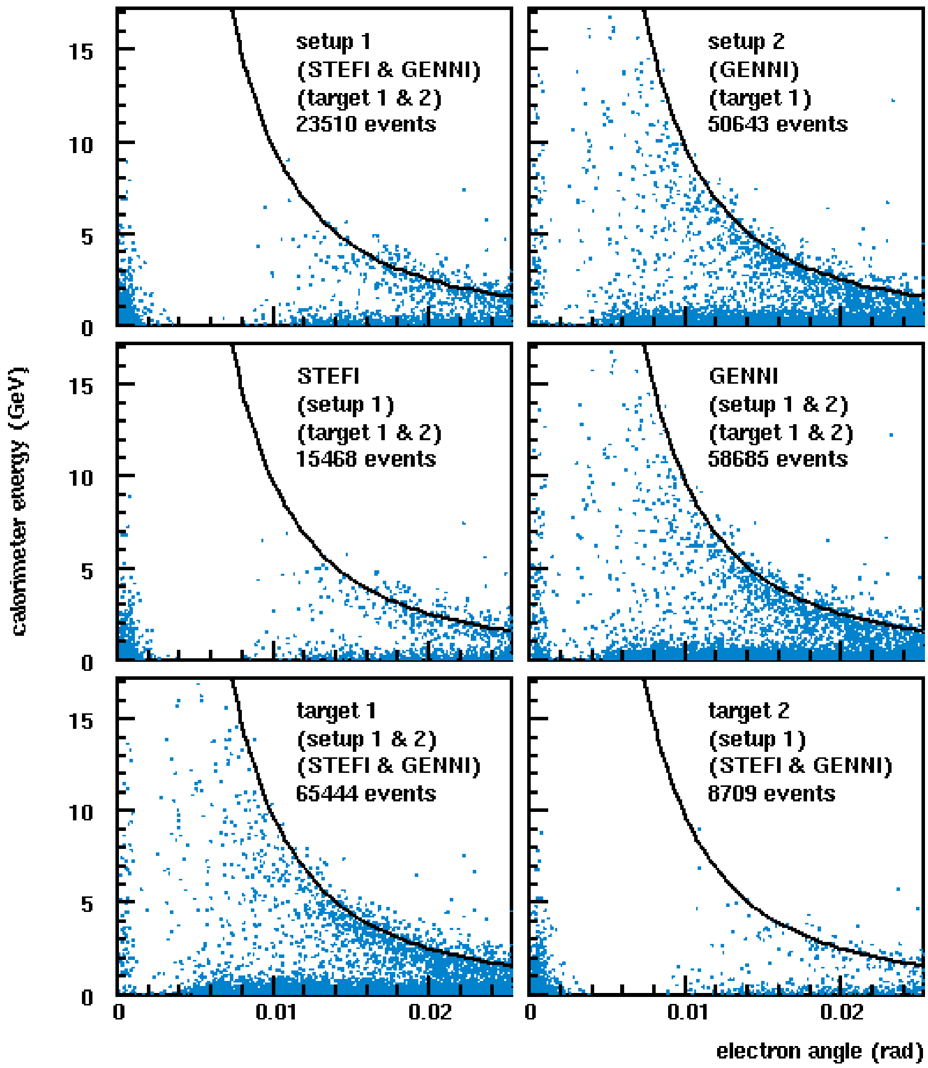

FIGURE 4.19. $(\theta_e, E_{\text{calo}})$ phase-space in the different apparatus configurations.

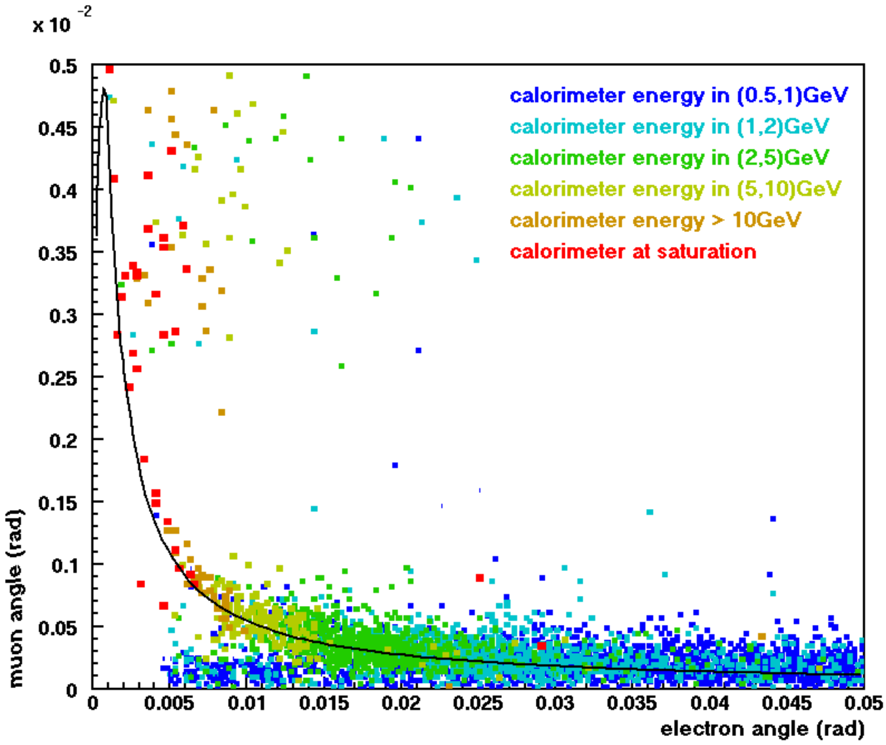

FIGURE 4.20. $(\theta_e, \theta_\mu, E_{\text{calo}})$ phase-space with the > 0.5 GeV elastic candidates. The energy information is represented with the colorscale.

energy threshold [GeV]	events	% of the elastic candidates
0	74153	100
0.5	6450	8.698
1	2938	3.962
2	1335	1.8
5	346	0.467
10	109	0.147
at saturation	41	0.055

TABLE 4.5. Elastic candidate statistics as a function of the energy threshold.

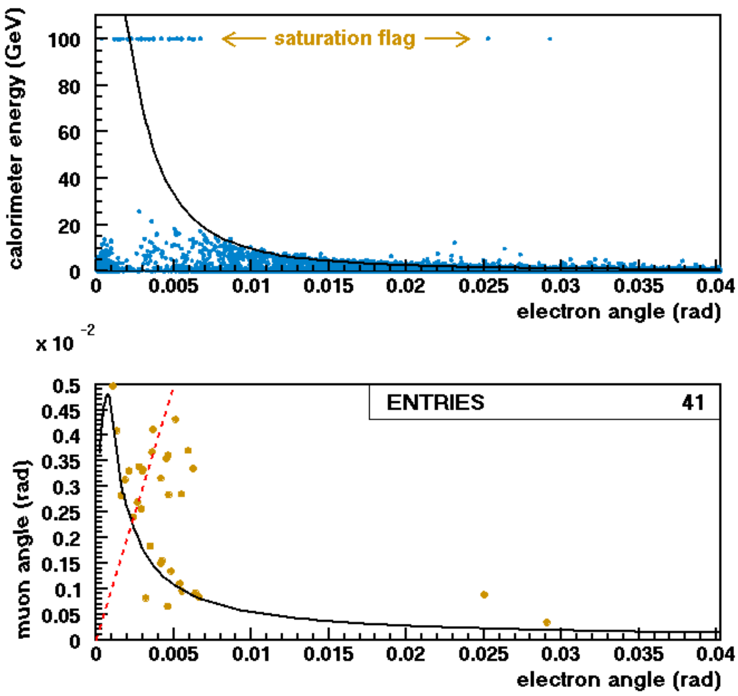

FIGURE 4.21. $(\theta_e, E_{\text{calo}})$ *(top)* and (θ_e, θ_μ) *(bottom)* phase-spaces with the calorimeter-saturating events

the precise measurement of the energy is not available, the tracking system information can be used: the event position in the (θ_e, θ_μ) phase-space is therefore accessible.
As already mentioned, the calorimeter-saturating events have been marked with an energy value of 100 GeV. Figure 4.21 shows that most of these events have $\theta_e \lesssim 7$ mrad, which corresponds to the theoretical phase-space region occupied by the $\gtrsim 20$ GeV elastic electrons, and overlap with the $\theta_\mu(\theta_e)$ curve.

4.7.4 Background populations

As already mentioned, several efforts are currently being made on the setup 2 data to exclude the background events left among the elastic candidates. The most important contribution to the overall phase-space background is given by the low-θ_μ band, whose exclusion requires a lower limit on the electron energy; the 1 GeV threshold level has been set (red box in figure 4.22 top). However, this selection criterion is not enough: as shown in figure 4.22 center, this condition alone leads to many false negatives, since it excludes all the elastic events in which the electron was out of the calorimeter acceptance and therefore its energy has not been measured.

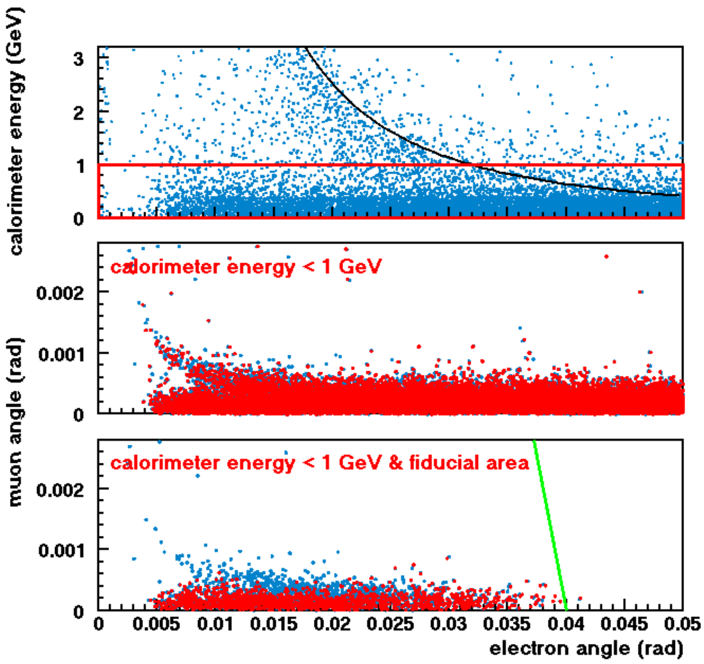

FIGURE 4.22. Low-θ_{μ} background rejection. The < 1 GeV band *(top)* has been excluded. This procedure leads to many false negatives *(center)* unless the statistics under study is limited to the events within the calorimeter acceptance *(bottom)*.

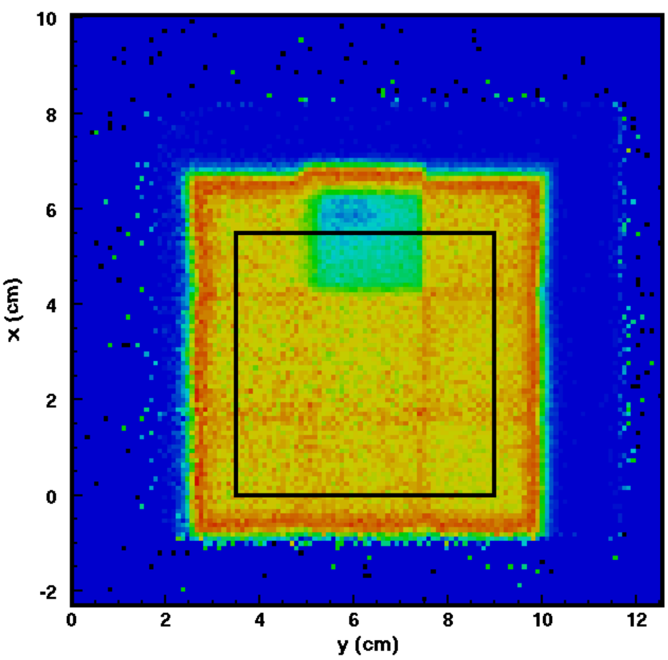

FIGURE 4.23. GENNI MIP signal map; one of the channels (channel 8 – scheme in figure 2.25) has proven to be inefficient. The chosen fiducial area is depicted in black.

This limitation can be overcome by selecting only the elastic candidates in which the electron crosses the calorimeter active volume (figure 4.23): indeed, in this case the separation between the elastic curve and the low-θ_μ background band can be performed (figure 4.22 bottom). Nevertheless, such a restriction introduces a $\lesssim$ 9 cm/220 cm $\sim$ 0.04 rad upper limit to the angular acceptance (green line), thus limiting the apparatus sensitivity in the normalization region. This addresses the need for a large-area calorimeter in the 2021 setup.

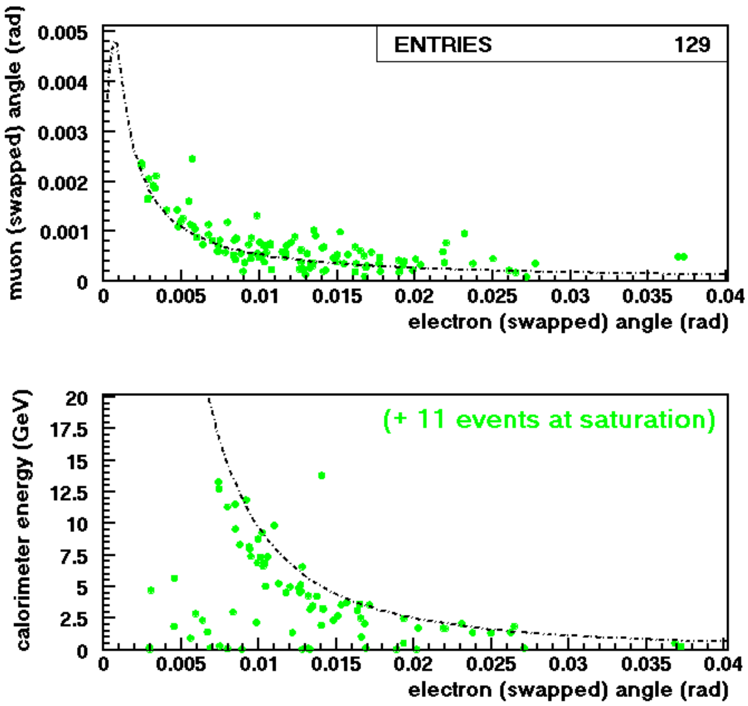

FIGURE 4.24. $(\theta_e^{\text{swap}}, E_{\text{calo}})$ and $(\theta_e^{\text{swap}}, \theta_\mu^{\text{swap}})$ phase-spaces after applying equation 4.8 to the elastic events whose output particles have been swapped. The black dashed curves represent the $\theta_\mu^{\text{swap}}(\theta_e^{\text{swap}})$ and $E_{\text{calo}}(\theta_e^{\text{swap}})$ theoretical predictions.

In the setup 2 dataset there are 129 events with $\theta_e < 2.5$ mrad, an energy up to several GeV and $\theta_\mu > 5$ mrad (green box in figure 4.18). Applying the transformation

$$\theta_e \rightleftharpoons \theta_\mu \tag{4.8}$$

on this population results in the phase-spaces in figure 4.24. It is clear that most of these events are not part of the background: they are low-E_e^{f} ($\lesssim$ 15 GeV) elastic events whose output particles have been swapped by the μ-e PID method; such events can therefore be included in the elastic kinematics analysis once equation 4.8 has been applied.

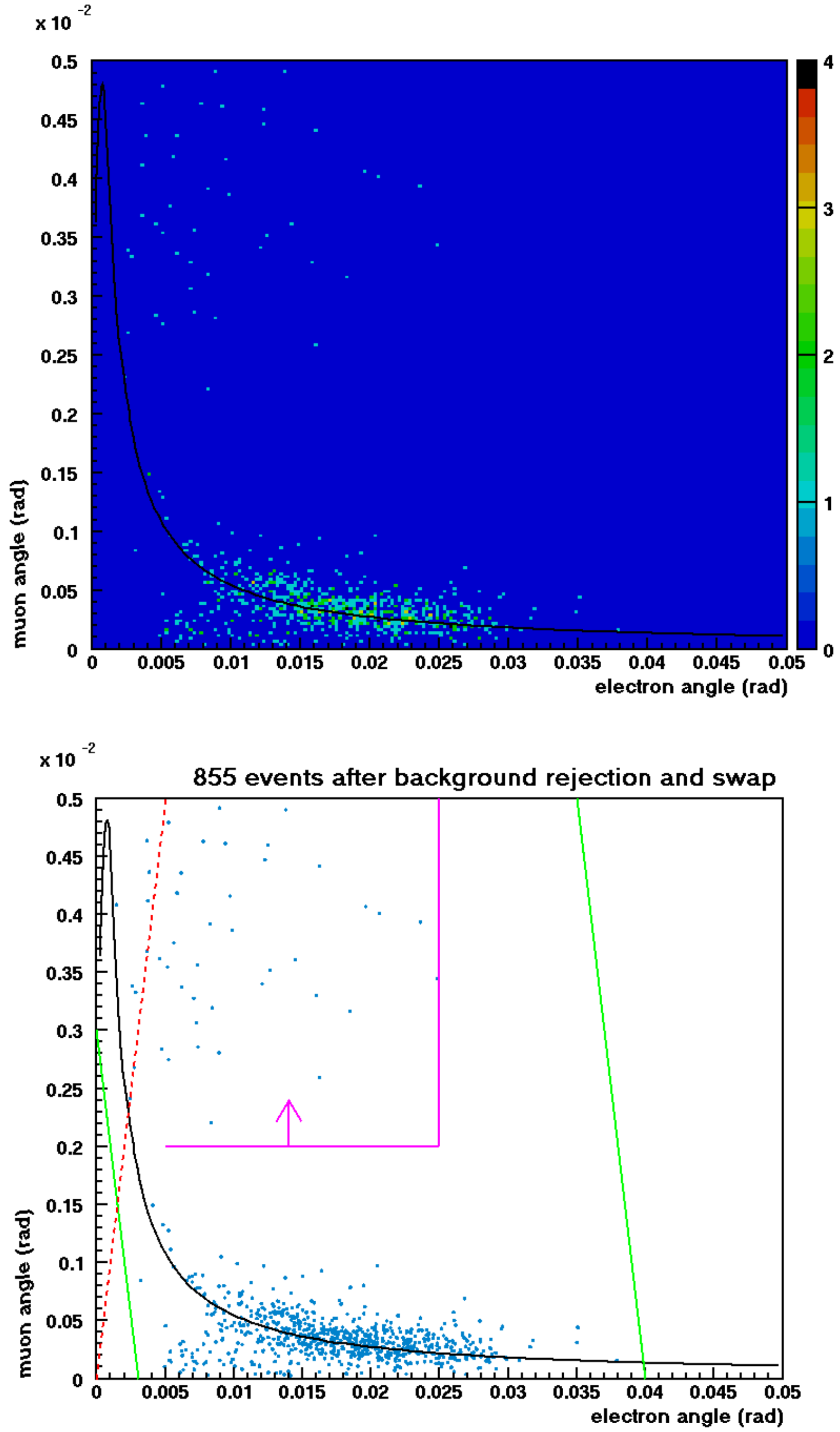

FIGURE 4.25. (θ_e, θ_μ) phase-space after the preliminary low-θ_μ background rejection and μ-e swap procedures; colorscale *(top)* and event-by-event *(bottom)* scatter plot. Both the upper and lower angular acceptance limits are shown (green lines).

Looking at figure 4.24, two considerations can be drawn:

- albeit rarely, the μ-e swap can occur in the low-energy part of the elastic phase-space.
- This identification method does not cover the region $\theta_e \lesssim 2.5$ mrad in which many wrong μ-e attributions are expected.

Figure 4.25 shows the (θ_e, θ_μ) phase-space with the fiducial cut on the GENNI active area (figure 4.23), with the $E_{\text{calo}} > 1$ GeV condition and with the μ-e swap correction (equation 4.8): albeit preliminary, this result shows that most of the low-θ_μ background events have been rejected. Further investigations are needed in order to develop an exclusion procedure for the high-θ_μ background population (purple lines).

Conclusions and outlook

The 3.6σ discrepancy between the theoretical prediction and the E821 (BNL) measurement of the muon magnetic anomaly might be a hint of the existence of New Physics beyond the Standard Model. Two new generation experiments, E989 (Fermilab) and E34 (J-PARC), are currently under development and are expected to push the value of the discrepancy above the 5σ level. Meanwhile, the MUonE experiment is developing a novel approach to measure the hadronic leading-order contribution to the Standard Model prediction of the anomaly, i.e. the main source of its uncertainty, with unprecedented precision. Unlike the traditional evaluation, which relies on the hadronic e^+e^- annihilation and τ decay data, the MUonE approach exploits the high-energy $\mu^{\pm}e^-$ elastic scattering cross-section, which is free of resonances.
The 2018 MUonE feasibility test highlighted the potential and the limitations of studying the scattering kinematics with

- the high-energy, high-intensity muons of the CERN M2 beamline;
- sixteen $\sim 10 \times 10$ cm^2, single-side silicon microstrip sensors with 242 μm readout pitch and ~ 35 μm intrinsic spatial resolution;
- two $\sim 10 \times 10$ cm^2, 8 mm thick graphite targets;
- a homogeneous scintillating calorimeter with a $\sim 10 \times 10$ cm^2 transverse section;
- the INSULAb DAQ, which allows an acquisition rate of ~ 900 Hz;
- a tracking system alignment algorithm based on the histogram method;
- a software μ-e PID method based on kinematics considerations.

The silicon detectors were arranged in three stations:

- the input station consisted of 6 tracking layers.
- The upstream target output station consisted of 6 layers.
- The downstream target output station consisted of 4 layers.

Each station was ~ 50 cm long. After ~ 3 months of data taking the downstream target was removed in order to study the performance of a single-target setup with a ~ 1.2 m long output lever arm. Each station featured a 45° stereo layer for the multiple-hit disambiguation. The hardware performance has proven to be highly stable in the whole ~ 7.5 month long run.
The alignment algorithm has proven to be a powerful tool for the detection and correction of the tracking system misalignments and the local hit reconstruction issues. Furthermore, this method is versatile: several applications to different experimental environments have already been performed or are under development.
During the 2018 data taking, ~ 552833856 single input particle events have been collected, out of which the pattern reconstruction algorithm allowed to select 74153 elastic candidates (134 ppm). The elastic region of the $(\theta_e, \theta_\mu, E_e^{\mathrm{f}})$ phase-space is contaminated with non-elastic electron background; in order to perform the scattering kinematics analysis, several methods for the non-elastic background rejection have been developed. The correlations between the kinematic variables θ_e, θ_μ and E_e^{f} predicted by the special relativity and by the simulations have been observed. The conclusion of this analysis work is that the 2018 experimental setup is suitable for the $\mu^\pm e^-$ elastic scattering measurement. Nevertheless, the feasibility test results address many hardware limitations that have to be overcome in the future runs:

- the distance between the target and the first output tracking module has to be long enough to guarantee that the signal region of the elastic phase-space is within the angular acceptance; however, given the fact that the possible experimental areas have limited dimensions, a trade-off between the setup compactness and the double-hit disambiguation power has to be made. Albeit better in terms of small-angle acceptance and angular resolution, smaller-pitch sensors have a smaller active area or a larger number of channels.

- Different tracking system lever arms lead to different acceptance limits; therefore, for the datasets collected with different modules to be homogeneous, the relative z positions of the target and of the tracking planes have to be the same for each station.

- The stereo layers can be avoided: although they represent a useful tool for the multiple-hit disambiguation, their orientation limits the overall tracking system acceptance and therefore results in a loss of statistics. Furthermore, as shown in this analysis work, the physical hits and the ghosts can be distinguished via the pattern recognition algorithm.

- The low-θ_μ background band can be rejected via an energy selection, which can be performed only on the events in which the output electron crosses the calorimeter active volume; a large enough calorimeter should therefore be used. Furthermore, a large-area detector increases the angular acceptance upper limit, thus ensuring the apparatus sensitivity in the normalization region.

Several efforts are currently being made in the 2018 data analysis

- in generalizing the pattern reconstruction output topology conditions;
- in treating the μ-e PID ambiguities;
- in refining the background rejection algorithms.

The hardware and software upgrades proceed in parallel to the development of the theoretical and analysis tools that will be needed for the determination of the $\mu^{\pm}e^{-}$ elastic scattering cross section, and hence of the hadronic leading-order contribution to the muon magnetic anomaly, from the 2021 data. Until then, the 2018 data will be further studied; moreover, they might be used to perform a preliminary evaluation of a_{μ}^{HLO}.

APPENDIX **A**

The calorimeters characterization

The 2018 INSULAb beamtest at the CERN T9 beamline was focused on the characterization of the MUonE calorimeters. The STEFI and GENNI equalization and calibration coefficients have been found and their energy resolution has been evaluated – the results are discussed in section 3.5. The beamtest setup and the experimental methods are summarized in this appendix.

A.1 The T9 beamline

The CERN East Hall T9 beamline (figure A.1) delivers a beam of secondary particles in the $(0.3, 10)$ GeV/c momentum range [131]. The beam consists of [131]

- pions and kaons produced when the 24 GeV/c protons extracted from the PS hit a target;
- tertiary muons and electrons;
- protons from the primary beam.

Figure A.2 shows the beam intensity and composition as a function of the momentum. Two Cherenkov counters with tunable gas mixture and pressure allow to perform the PID (section A.2).
The T9 beam is ~ 3 cm wide (figure A.3) and has a ~ 7 mrad (~ 3 mrad) divergence in the x (y) direction (figure A.4). Such a large beam proves to be ideal for the characterization of STEFI and GENNI, which have a $\sim 10 \times 10$ cm^2 transverse section. Furthermore, the few-GeV/c momentum range allows to calibrate the calorimeters at the typical elastic electron energy values.

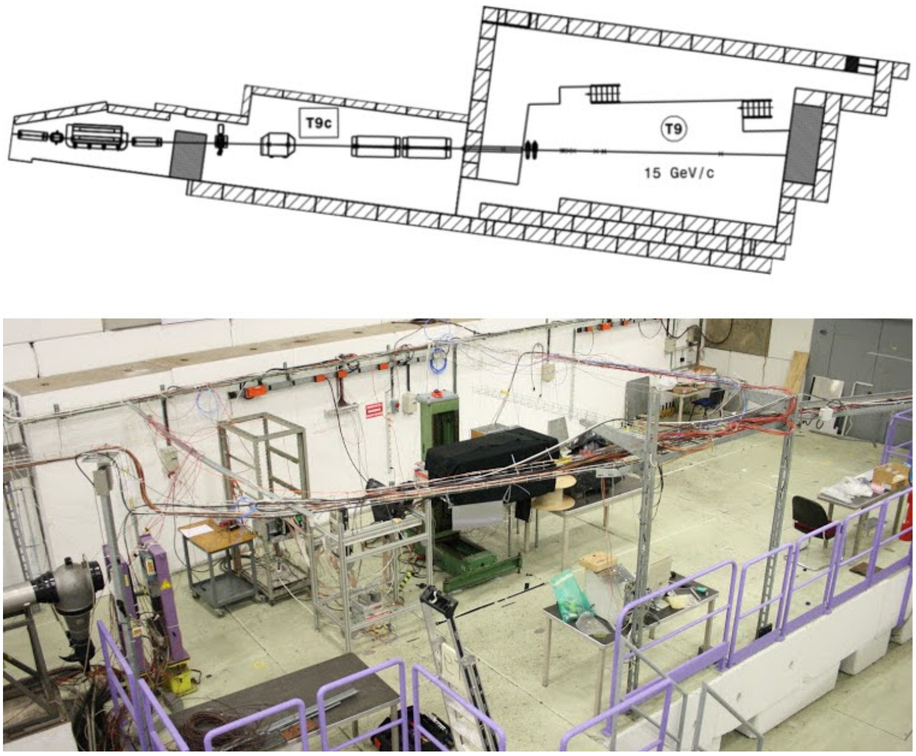

FIGURE A.1. *(top)* Scheme of the T9 beamline – edited from [83]. *(bottom)* The T9 experimental area with the INSULAb beamtest setup.

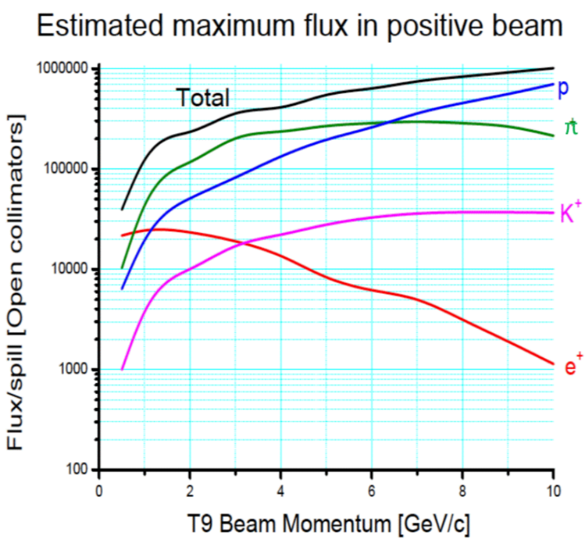

FIGURE A.2. T9 beam intensity and composition as a function of the particle momentum [131].

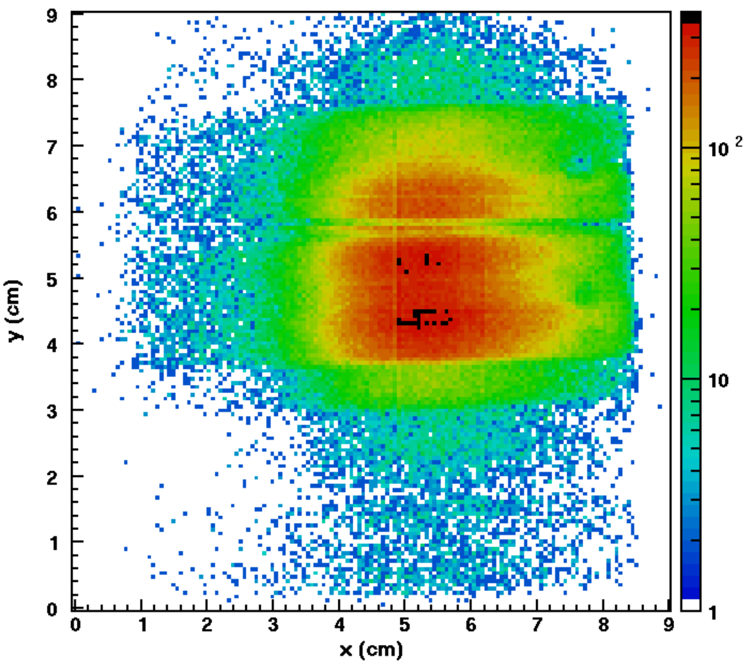

FIGURE A.3. T9 beam spot.

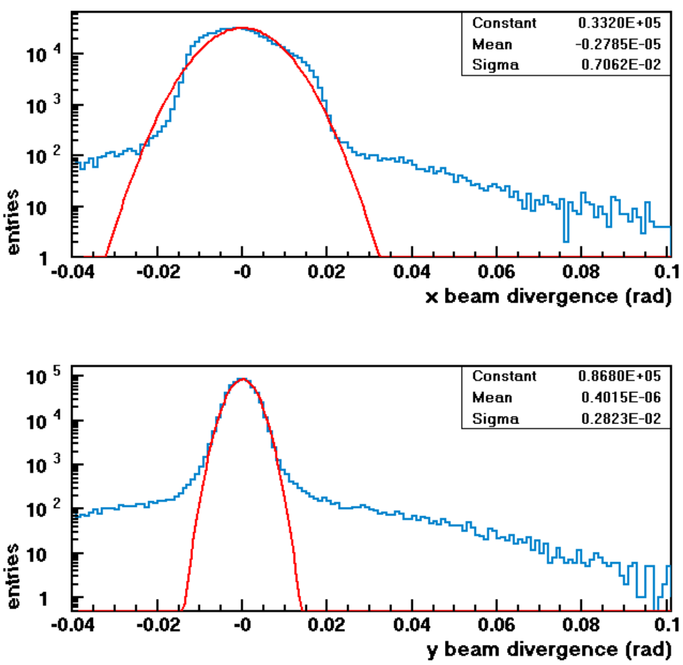

FIGURE A.4. T9 beam divergence.

A.2 The setup

The beamtest setup is shown in figure A.5. The first element of the setup is the Cherenkov counters pair (figure A.6 left) [83]:

- each detector is composed of a cylindrical (∅ ∼ 20 cm) gaseous volume coupled to a PMT.
- The upstream (downstream) counter is 5 m (2.5 m) long.
- Each counter has an independent gas circuit.

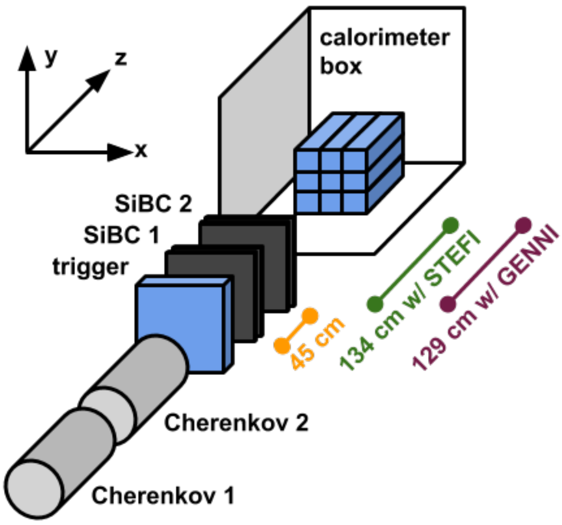

FIGURE A.5. Scheme of the INSULAb T9 beamtest setup.

The choice of the gas mixture and of the pressure allows to set a velocity threshold for the Cherenkov emission [131]. Since the beam momentum $p = m\gamma v$ is fixed, different particles have different velocity and therefore they can be distinguished from each other by means of their Cherenkov emission in the counters [131]. In particular, once the threshold values have been set properly, the two counters can be used to separate

- the electrons, which always emit Cherenkov light;
- the muons, which emit Cherenkov light only in the highest-pressure detector;
- the pions (and the heavier hadrons), which do not emit Cherenkov light in the counters.

In practice, since $m_\pi = 139.57018(35)$ MeV$/c^2 \sim 1.32 m_\mu$ [2], the identification of the threshold for the π-μ disambiguation proves to be difficult; nevertheless, only

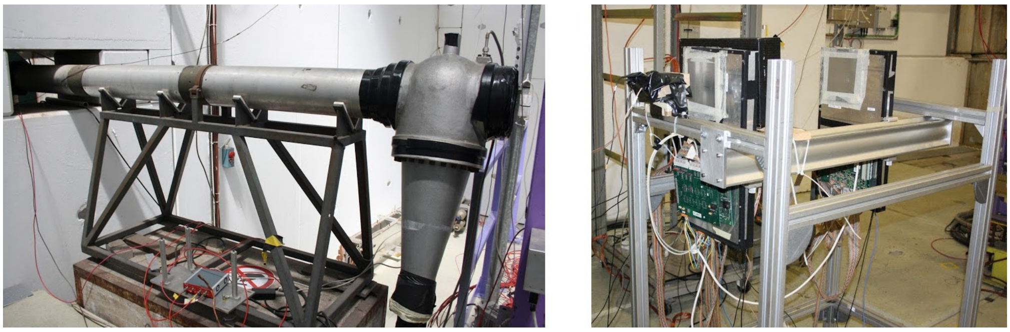

FIGURE A.6. INSULAb T9 beamtest detectors: the Cherenkov counters *(left)* and the tracking system *(right)*.

the electron separation is needed for the calorimeters characterization, therefore the same threshold has been set for both the counters during the beamtest.
Two Silicon Beam Chambers (figure A.6 right), which consist of the same sensors and ASICs as the MUonE tracking detectors (subsection 2.3.1), allow to track the input particles. The minimization of the MCS contribution to the few-GeV/c electron tracks requires a compact setup: leaving aside the upstream Cherenkov counters, the apparatus is less than 2 m long.

A.3 Channel equalization method

As discussed in section 3.5, the first step in the calorimeter characterization consists in the equalization of the channels, which is performed using the MIP signals. The identification of the MIP events is performed via

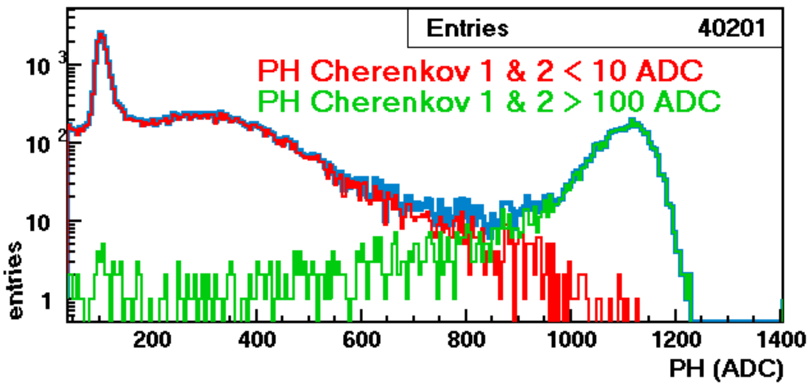

FIGURE A.7. GENNI spectrum with the Cherenkov-based PID: the electron (muon and hadron) spectrum is shown in red (green). The muons populate the MIP peak at ~ 100 ADC.

- a selection on the hit time, in order to exclude the baseline fluctuation events (section 3.5);
- an upper limit on the Cherenkov counters, which allows to separate the muons and pions from the electrons (figure A.7).

Furthermore, given the fact that the i-th channel MIP peak energy depends on the length of the particle path inside the active volume, only the MIPs whose path inside the i-th crystal has approximately the same length have to be considered. Therefore:

- only the tracks with a small input angle, i.e. $\pm 3\sigma$ with respect to the divergence peak center (figure A.4), are selected.
- Only the tracks that hit the i-th crystal front side within a fiducial area are selected.

The i-th fiducial area is defined using its MIP signal map, i.e. the xy distribution of the MIP events (PH(i) < 200 ADC) detected by the i-th crystal (figure A.8). In the GENNI case, the calorimeter was installed with no transverse tilts around x and y and all the crystals were illuminated by the input beam; therefore, the fiducial areas reduce to $\sim 1.5 \times 1.5$ cm^2 squares at the crystal front side center.

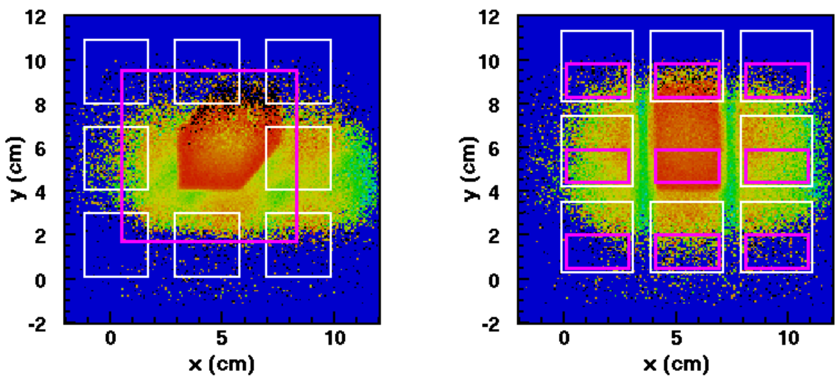

FIGURE A.8. STEFI central channel signal map without *(left)* and with *(right)* the box tilt around y. The white boxes represent the positions of the neighbouring channels. The purple boxes represent the fiducial selections used for the calibration with the electrons *(left)* and for the channels equalization with the MIPs *(right)*.

On the other hand, in order to define the STEFI fiducial areas two limitations have to be overcome:

- the STEFI mechanical support tilts the crystals around both x and y (figure A.8 left), which eliminates the acceptance limits introduced by the dead regions between the channels but complicates the MIP analysis. The tilt around y has been counterbalanced by rotating the STEFI box properly (figure A.8 right), while the effect of the tilt around x has to be treated offline.

- Part of the channel 7, 8 and 9 active areas was out of the beam (figure A.9).

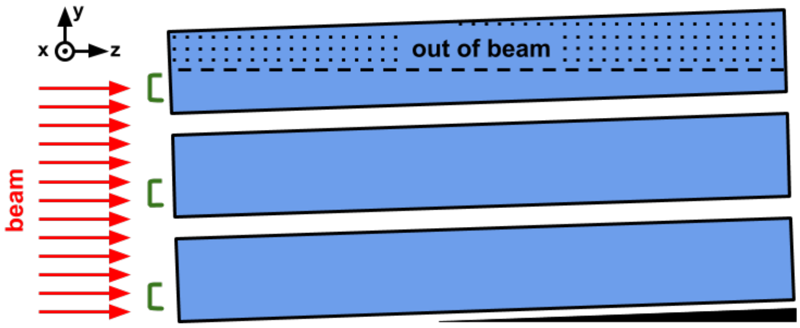

FIGURE A.9. STEFI position with respect to the beam: since the top side of channels 7, 8 and 9 is not illuminated, only the bottom side of all the channels (green brackets) is included in the MIP event selection.

These items limit the fiducial selection possibilities: the $\sim 1.5 \times 3$ cm^2 regions shown in figures A.8 right (pink boxes) and A.9 (green brackets) have been chosen.
These selections allow to obtain the single-channel MIP peaks (figure A.10 left), whose MPVs differ from each other of tens of ADC. The MPVs are determined by fitting the peaks with the Moyal approximation of the Landau function [132, 133]

$$f(x) = L_1 \exp\left\{-\frac{1}{2}\left[\left(\frac{x-L_2}{L_3/4.018}\right) + \exp\left(-\frac{x-L_2}{L_3/4.018}\right)\right]\right\} \tag{A.1}$$

where L_1 is the distribution amplitude, L_2 is its MPV and L_3 is its width. Once the reference channel has been chosen (the central one for both the calorimeters), the MPV value that results from the STEFI i-th channel peak fit defines the Q_i value that appears in equation 3.11, while in the GENNI case the transformation shown in equation 3.17 is needed (subsection 3.6.2). An example of equalization result is shown in figure A.10 right.

A.4 Calibration method

Once the equalization procedure has been completed, it is possible to sum the calorimeter channels (equation 3.12) and perform the ADC-to-energy calibration using the data taken with different input momenta and, in the STEFI case, having restored the tilt around y. The following event selection conditions are applied:

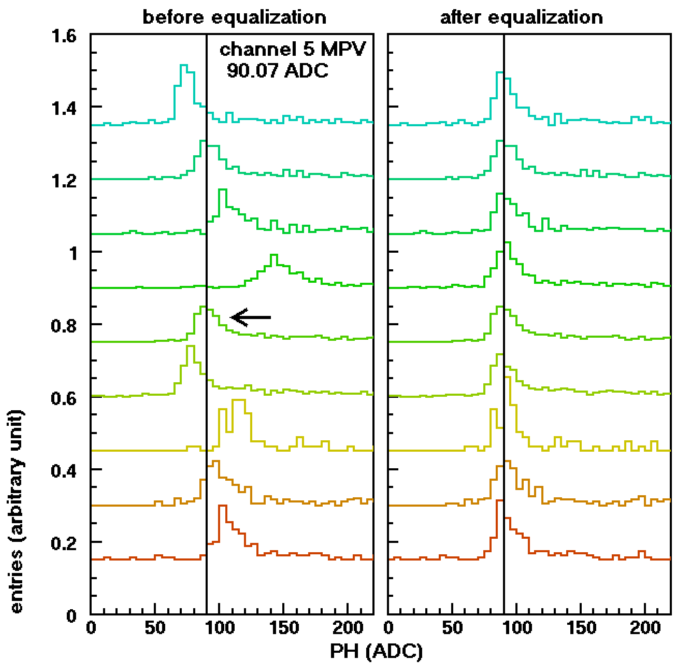

FIGURE A.10. GENNI single-channel MIP peaks before *(left)* and after *(right)* the equalization. The black arrow indicates the reference (channel 5) peak.

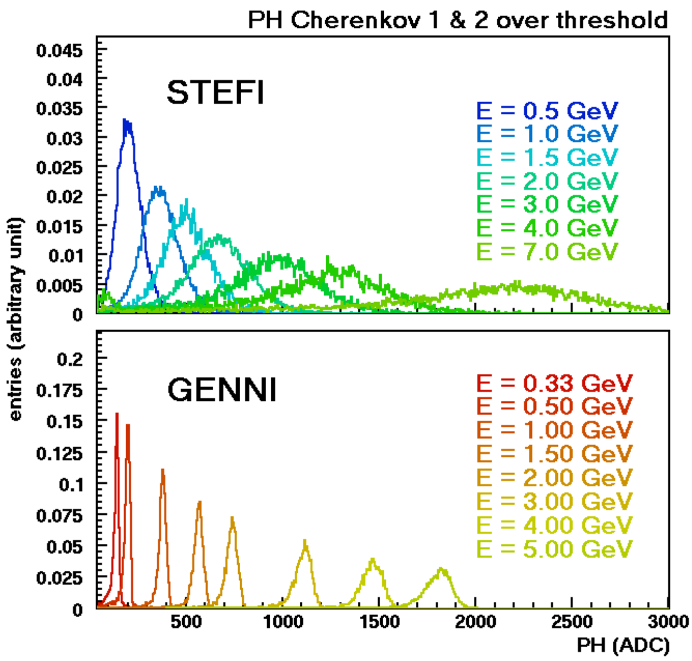

FIGURE A.11. STEFI *(top)* and GENNI *(bottom)* electron peak at different energies.

- only the events with an in-range hit time of at least one channel are considered.
- The electron events are selected with the Cherenkov counters.
- Fiducial cuts exclude the events that cross the overall active volume near the outer boundaries; as shown in figure A.8 left (purple box), the tilted configuration allows to include the inner dead regions in the selection.

Figure A.11 shows the momentum scan results. Gaussian fits allow to find the electron peak mean values, which constitute the abscissas in figure 3.18. Furthermore, the energy resolution that appears in equation 3.14 is defined by

$$\mathrm{res}_{\mathrm{calo}}(E_{\mathrm{calo}}) = \frac{\sigma_{\mathrm{fit}}(E_{\mathrm{calo}})\ [\mathrm{ADC}]}{\mathrm{PH}_{\mathrm{calo}}} \tag{A.2}$$

where $\sigma_{\mathrm{fit}}(E_{\mathrm{calo}})$ is the Gaussian sigma in ADC of the electron peak corresponding to E_{calo}.

List of acronyms

ADC	Analog to Digital Converter
AGILE	Astro-rivelatore Gamma a Immagini LEggero
AGS	Alternating Gradient Synchrotron
ALEPH	Apparatus for LEP pHysics
ASCII	American Standard Code for Information Interchange
ASIC	Application-Specific Integrated Circuit
BES-III	BEijing Spectrometer-III
BGO	Bismuth Germanium Oxide
BMS	Beam Momentum Station
BNL	Brookhaven National Lab
CAEN	Costruzioni Apparecchiature Elettroniche Nucleari
CEDAR	ChErenkov Differential counters with Achromatic Ring focus
CERN	Conseil Européen pour la Recherche Nucléaire
CL	Confidence Level
CM	Common Mode
CMD	Cryogenic Magnet Detector
CMS	Compact Muon Solenoid
COG	Center Of Gravity
COMPASS	COmmon Muon and Proton Apparatus for Structure and Spectroscopy
DAΦNE	Double Annular Φ Factory for Nice Experiments
DAQ	Data AcQuisition
DC	Direct Current
DELPHI	DEtector with Lepton, Photon and Hadron Identification
DOF	Degrees Of Freedom
DR	Delivery Ring
DST	Data Summary Tape
EDM	Electric Dipole Moment
ERNI	Enhanced Routing Network Interconnect
EW	ElectroWeak
FLOPS	FLoating-point Operations Per Second

FODO	FOcusing-DefOcusing
GECO	GEneral COntrol
GPIB	General Purpose Interface Bus
GUI	Graphical User Interface
HHO	Hadronic Higher Order
HLO	Hadronic Leading-Order
HNLO	Hadronic Next-to-Leading-Order
HNNLO	Hadronic Next-to-Next-to-Leading-Order
ISR	Initial State Radiation
J-PARC	Japan-Proton Accelerator Research Complex
KLOE	K-LOng Experiment
LBL	Light-By-Light
LEP	Large Electron-Positron collider
LO	Leading-order
LVDS	Low-Voltage Differential Signal
MAPMT	Multi-Anode PhotoMultiplier Tube
MCS	Multiple Coulomb Scattering
MIP	Minimum Ionising Particle
MPV	Most Probable Value
MLF	Materials and Life sciences Facility
MSR	Muon Storage Ring
NMR	Nuclear Magnetic Resonance
OPAL	Omni-Purpose Apparatus at LEP
PADME	Positron Annihilation into Dark Matter Experiment
PBC	Physics Beyond Colliders
PC	Personal Computer
PCB	Printed Circuit Board
PH	Pulse Height
PID	Particle IDentification
PMT	PhotoMultiplier Tube
PS	Proton Synchrotron
QCD	Quantum ChromoDynamics
QED	Quantum ElectroDynamics
RAM	Random Access Memory
RMS	Root Mean Square
RPD	Recoil Proton Detector
SiPM	Silicon PhotoMultiplier
SiBC	Silicon Beam Chamber
SM	Standard Model
SND	Spherical Neutral Detector
SPS	Super Proton Synchrotron

Tcl/Tk	Tool command language/Toolkit
TPC	Time Projection Chamber
VME	Versa Module Europa bus
VNC	Virtual Network Computing
VP	Vacuum Polarization
VRB	VME Readout Board
WLS	WaveLength Shifter

List of Figures

List of Tables

Bibliography

1. D. Hanneke, S. Fogwell & G. Gabrielse. New measurement of the electron magnetic moment and the fine structure constant. *Physical Review Letters* **100,** 120801 (2008).
2. C. Patrignani *et al.* Review of Particle Physics. *Chinese Physics C* **40,** 100001 (2016).
3. R. Feynman. *The Feynman Lectures on Physics: Volume 2* (Addison-Wesley, 1963).
4. K. Melnikov & A. Vainshtein. *Theory of the Muon Anomalous Magnetic Moment* (Springer, 2007).
5. F. H. Combley. $(g-2)$ factors for muon and electron and the consequences for QED. *Reports on Progress in Physics* **42,** 1889–1935 (1979).
6. J. D. Bjorken & S. D. Drell. *Relativistic Quantum Mechanics* (McGraw-Hill, 1964).
7. W. Greiner & D. A. Bromley. *Quantum Mechanics: An introduction* (Springer, 2011).
8. F. Combley, F. J. M. Farley & E. Picasso. The CERN muon $(g - 2)$ experiments. *Physics Reports* **68,** 93–119 (1981).
9. J. Schwinger. On quantum-electrodynamics and the magnetic moment of the electron. *Physical Review* **73,** 416–417 (1948).
10. M. Passera. The Standard Model prediction of the muon anomalous magnetic moment. *Journal of Physics G* **31,** R75–R94 (2005).
11. J. P. Miller, E. De Rafael, B. L. Roberts & D. Stöckinger. Muon $(g - 2)$: Experiment and theory. *Annual Review of Nuclear and Particle Science* **62,** 237–264 (2012).
12. M. Passera. Electron, muon and tau magnetic moments: A theoretical update. *Nuclear Physics B Proceedings Supplements* **169,** 213–225 (2007).
13. R. H. Parker *et al.* Measurement of the fine-structure constant as a test of the Standard Model. *Science* **360,** 191–195 (2018).
14. J. Uretsky. Do muons point to new physics? *Physics World* **14,** 24 (2001).

15. C. Bouchiat & L. Michel. La résonance dans la diffusion méson π-méson π et le moment magnétique anormal du méson μ. *Journal de Physique et Le Radium* **22,** 121 (1961).
16. A. Bevan *et al. The Physics of the B Factories* (Springer, 2015).
17. R. Alemany, M. Davier & A. Höcker. Improved determination of the hadronic contribution to the muon $g-2$ and to $\alpha(M_Z^2)$ using new data from hadronic τ decays. *European Physical Journal C* **2,** 123–135 (1998).
18. M. Davier. Updated estimate of the muon magnetic moment using revised results from e^+e^- annihilation. *Nuclear Physics B Proceedings Supplements* **131,** 192–200 (2004).
19. M. Davier *et al.* The discrepancy between τ and e^+e^- spectral functions revisited and the consequences for the muon magnetic anomaly. *European Physical Journal C* **66,** 127–136 (2010).
20. A. Pich. Precision tau physics. *Progress in Particle and Nuclear Physics* **75,** 41–85 (2014).
21. M. Davier, A. Hoecker, B. Malaescu & Z. Zhang. Reevaluation of the hadronic contributions to the muon $g-2$ and to $\alpha(M_Z^2)$. *European Physical Journal C* **71,** 1515 (2011).
22. M. Passera, W. J. Marciano & A. Sirlin. The muon $g-2$ discrepancy: Errors or new physics? *AIP Conference Proceedings* **1078,** 378–381 (2008).
23. T. Blum, M. Hayakawa & T. Izubuchi. Hadronic corrections to the muon anomalous magnetic moment from lattice QCD. *Proceedings of Science* (2012).
24. G. Abbiendi *et al.* Measuring the leading hadronic contribution to the muon $g-2$ via μe scattering. *European Physical Journal C* **77,** 139 (2017).
25. R. R. Akhmetshin *et al.* Measurement of $\sigma(e^+e^- \to \pi^+\pi^-)$ cross-section with CMD-2 around ρ-meson. *Physics Letters B* **527,** 161–172 (2002).
26. R. R. Akhmetshin *et al.* Update: A reanalysis of hadronic cross section measurements at CMD-2. *Physics Letters B* **578,** 285–289 (2004).
27. A. Aloisio *et al.* Measurement of $\sigma(e^+e^- \to \pi^+\pi^-\gamma)$ and extraction of $\sigma(e^+e^- \to \pi^+\pi^-)$ below 1 GeV with the KLOE detector. *Physics Letters B* **606,** 12–24 (2005).
28. F. Ambrosino *et al.* Measurement of $\sigma(e^+e^- \to \pi^+\pi^-\gamma(\gamma))$ and the dipion contribution to the muon anomaly with the KLOE detector. *Physics Letters B* **670,** 285–291 (2009).
29. F. Ambrosino *et al.* Measurement of $\sigma(e^+e^- \to \pi^+\pi^-)$ from threshold to 0.85 GeV^2 using initial state radiation with the KLOE detector. *Physics Letters B* **700,** 102–110 (2011).

30. D. Babusci *et al.* Precision measurement of $\sigma(e^+e^- \to \pi^+\pi^-\gamma)/\sigma(e^+e^- \to \mu^+\mu^-\gamma)$ and determination of the $\pi^+\pi^-$ contribution to the muon anomaly with the KLOE detector. *Physics Letters B* **720,** 336–343 (2013).
31. A. Anastasi *et al.* Combination of KLOE $\sigma(e^+e^- \to \pi^+\pi^-)$ measurements and determination of $a_\mu^{\pi^+\pi^-}$ in the energy range $0.10 < s < 0.95$ GeV^2. *Journal of High Energy Physics* **2018,** 173 (2018).
32. J. P. Lees *et al.* Precise measurement of the $e^+e^- \to \pi^+\pi^-(\gamma)$ cross section with the initial-state radiation method at BABAR. *Physical Review D* **86,** 032013 (2012).
33. D. Bernard. Low-energy hadronic cross sections measurements at BABAR and $g-2$ of the muon. *Nuclear and Particle Physics Proceedings* **282-284,** 132–138 (2017).
34. G. Vasseur. Measurement of hadronic cross sections with BABAR. *Nuclear and Particle Physics Proceedings* **294-296,** 164–169 (2018).
35. A. A. Korol *et al.* Measurement of the hadronic cross sections with the CMD-3 and SND detectors at the VEPP-2000 collider. *EPJ Web of Conferences* **182,** 02068 (2018).
36. S. Schumann. Hadronic cross section measurement at BES-III. *International Journal of Modern Physics: Conference Series* **35,** 1460408 (2014).
37. M. Ablikim *et al.* Measurement of the $e^+e^- \to \pi^+\pi^-$ cross section between 600 and 900 MeV using initial state radiation. *Physics Letters B* **753,** 629–638 (2016).
38. `indico.mitp.uni-mainz.de/event/86/contributions/2703`.
39. `lnf.infn.it/kloe/index2.html`.
40. `slac.stanford.edu/xorg/BFLB`.
41. R. Barate *et al.* Measurement of the spectral functions of vector current hadronic tau decays. *Zeitschrift für Physik C* **76,** 15–33 (1997).
42. M. Davier. Measurement of branching fractions and spectral functions in τ decays. *Nuclear Physics B Proceedings Supplements* **144,** 45–58 (2005).
43. M. Davier *et al.* Reevaluation of the hadronic contribution to the muon magnetic anomaly using new $e^+e^- \to \pi^+\pi^-$ cross section data from BABAR. *European Physical Journal C* **66,** 1–9 (2010).
44. A. Kurz, T. Liu, P. Marquard & M. Steinhauser. Hadronic contribution to the muon anomalous magnetic moment to next-to-next-to-leading order. *Physics Letters B* **734,** 144–147 (2014).
45. A. Guevara. Hadronic light-by-light contribution to the muon $g-2$. *Journal of Physics Conference Series* **761,** 012009 (2016).
46. G. Colangelo *et al.* Remarks on higher-order hadronic corrections to the muon $g-2$. *Physics Letters B* **735,** 90–91 (2014).

47. J. Holzbauer. The Muon $g-2$ Experiment Overview and Status as of June 2016. *Journal of Physics Conference Series* **770,** 012038 (2016).

48. M. Davier, A. Hoecker, B. Malaescu & Z. Zhang. Reevaluation of the hadronic vacuum polarisation contributions to the Standard Model predictions of the muon $g-2$ and $\alpha(M_Z^2)$ using newest hadronic cross-section data. *European Physical Journal C* **77,** 827 (2017).

49. `belle.kek.jp/press/photos`.

50. G. A. González-Springberg & J. Vidal. Tau magnetic moment. *Journal of Physics Conference Series* **912,** 012001 (2017).

51. T. Coffin *et al.* Magnetic moment of the free muon. *Physical Review* **109,** 973–979 (1958).

52. G. W. Bennett *et al.* Improved limit on the muon electric dipole moment. *Physical Review D* **80,** 052008 (2009).

53. G. W. Bennett *et al.* Final report of the E821 muon anomalous magnetic moment measurement at BNL. *Physical Review D* **73,** 072003 (2006).

54. M. Otani. Status of the Muon $g-2$/EDM Experiment at J-PARC (E34). *JPS Conference Proceedings* **8,** 025008 (2015).

55. T. Gorringe. Fermilab muon $g-2$ experiment. *EPJ Web of Conferences* **179,** 01004 (2018).

56. R. L. Garwin, L. M. Lederman & M. Weinrich. Observations of the failure of conservation of parity and charge conjugation in meson decays: The magnetic moment of the free muon. *Physical Review* **105,** 1415–1417 (1957).

57. S. B. Nurushev, M. F. Runtso & M. N. Strikhanov. *Introduction to Polarization Physics* (Springer, 2012).

58. `musr.ca/intro/musr/cap/pidk.htm`.

59. `home.cern/news/news/accelerators/synchrocyclotron-prepares-visitors`.

60. J. Bailey *et al.* Final report on the CERN muon storage ring including the anomalous magnetic moment and the electric dipole moment of the muon, and a direct test of relativistic time dilation. *Nuclear Physics B* **150,** 1–75 (1979).

61. `muon-g-2.fnal.gov`.

62. L. A. Ahrens *et al.* High intensity performance of the Brookhaven AGS. *Proceedings of the IEEE Particle Accelerator Conference* **1,** 614–616 (1999).

63. G. W. Bennett *et al.* Measurement of the negative muon anomalous magnetic moment to 0.7 ppm. *Physical Review Letters* **92,** 161802 (2004).

64. D. Flay. Precision magnetic field calibration for the Muon $g-2$ Experiment at Fermilab. *Proceedings of Science* (2016).

65. F. Jegerlehner. *The Anomalous Magnetic Moment of the Muon* (Springer, 2017).

66. F. J. M. Farley. A new ring structure for muon $(g-2)$ measurements. *Nuclear Instruments and Methods in Physics Research A* **523,** 251–255 (2004).

67. A. J. Silenko. Potential for a new muon $g-2$ experiment. *Physics Letters B* **695,** 55–58 (2011).

68. D. W. Hertzog. Next Generation Muon $g-2$ Experiments. *EPJ Web of Conferences* **118,** 01015 (2016).

69. D. Stratakis *et al.* Commissioning and first results of the Fermilab Muon Campus. *Physical Review Accelerators and Beams* **22,** 011001 (2019).

70. `g-2.kek.jp`.

71. C. M. Carloni Calame, M. Passera, L. Trentadue & G. Venanzoni. A new approach to evaluate the leading hadronic corrections to the muon $g-2$. *Physics Letters B* **746,** 325–329 (2015).

72. R. Bufalo. On the Bhabha scattering for $z = 2$ Lifshitz QED. *International Journal of Modern Physics A* **30,** 1550086 (2015).

73. A. A. Pivovarov. Running electromagnetic-coupling constant: Low-energy normalization and the value at M_Z. *Physics of Atomic Nuclei* **65,** 1319–1340 (2002).

74. P. Achard *et al.* Measurement of the running of the electromagnetic coupling at large momentum-transfer at LEP. *Physics Letters B* **623,** 26–36 (2005).

75. `pbc.web.cern.ch`.

76. `indico.cern.ch/event/523655`.

77. `indico.cern.ch/event/644287`.

78. `indico.cern.ch/event/706741`.

79. `indico.cern.ch/event/755856`.

80. M. Diehl & G. Schnell. *Physics Beyond Colliders QCD Working Group Report* Technical report. 2018.

81. G. Lanfranchi *et al. Report of the BSM Working Group of the Physics Beyond Colliders at CERN* Technical report. 2018.

82. P. Abbon *et al.* The COMPASS setup for physics with hadron beams. *Nuclear Instruments and Methods in Physics Research A* **779,** 69–115 (2015).

83. `sba.web.cern.ch/sba/BeamsAndAreas/beam_lines.html`.

84. P. Abbon *et al.* The COMPASS experiment at CERN. *Nuclear Instruments and Methods in Physics Research A* **577,** 455–518 (2007).
85. `wwwcompass.cern.ch`.
86. F. Nerling. Highlights from the COMPASS experiment at CERN. Hadron spectroscopy and excitations. *EPJ Web of Conferences* **126,** 04033 (2016).
87. G. Reicherz *et al.* Future plannings for the COMPASS polarized target. *Proceedings of Science* (2018).
88. M. Quaresma. Polarised Drell-Yan process in COMPASS. *Proceedings of Science* (2016).
89. M. Fael & M. Passera. *Muon-electron scattering at NNLO: the hadronic corrections* To be published. 2019.
90. A. Principe. *Reference formulae for μ-e scattering* Private communication. 2019.
91. M. Bonanomi. *Study and validation of an innovative experiment to measure the hadronic contributions to the running of α_{em}* Master thesis (Università degli Studi di Milano-Bicocca, 2018).
92. `agenda.infn.it/event/16786`.
93. G. Abbiendi. Measurement of the leading hadronic contribution to the muon $g-2$ via space-like data. *Proceedings of Science* (2017).
94. G. Barbiellini *et al.* The AGILE silicon tracker: Testbeam results of the prototype silicon detector. *Nuclear Instruments and Methods in Physics Research A* **490,** 146–158 (2002).
95. M. Prest *et al.* The AGILE silicon tracker: An innovative γ-ray instrument for space. *Nuclear Instruments and Methods in Physics Research A* **501,** 280–287 (2003).
96. G. Fedel. *Il tracciatore al silicio-tungsteno di AGILE: uno strumento innovativo per l'astronomia gamma* Thesis (Università degli Studi di Trieste, 2000).
97. D. Lietti. *VISION: a Versatile and Innovative SIlicOn tracking system* PhD thesis (Università degli Studi dell'Insubria & CERN, 2015).
98. M. Tavani *et al.* The AGILE mission and its scientific instrument. *Proceedings of SPIE* **6266,** 626603 (2006).
99. R. Turchetta. Spatial resolution of silicon microstrip detectors. *Nuclear Instruments and Methods in Physics Research A* **335,** 44–58 (1993).
100. IDEAS. *The TA1 specifications* Technical report. 1997.
101. IDEAS. *The TAA1 specifications* Technical report. 2000.
102. E. Vallazza *et al.* The AGILE gamma ray satellite: The construction and performance of the silicon tracker. *IEEE Nuclear Science Symposium Conference Record* **1,** 176–180 (2004).

103. R. Mankel. Pattern recognition and event reconstruction in particle physics experiments. *Reports on Progress in Physics* **67,** 553–622 (2004).

104. G. Ballerini, A. Pugliese & M. Soldani. *INSULAb telescope characterization* Private communication. 2017.

105. S. Hasan. *Experimental techniques for deflection and radiation studies with bent crystals* PhD thesis (Università degli Studi dell'Insubria & CERN, 2011).

106. A. Berra *et al.* A SiPM based readout system for lead tungstate crystals. *Nuclear Instruments and Methods in Physics Research A* **732,** 380–383 (2013).

107. R. Y. Zhu *et al.* A study on the properties of lead tungstate crystals. *Nuclear Instruments and Methods in Physics Research A* **376,** 319–334 (1996).

108. `pdf.datasheetcatalog.com/datasheet/hamamatsu/H6780-03.pdf`.

109. M. Raggi *et al.* Performance of the PADME Calorimeter prototype at the DAΦNE BTF. *Nuclear Instruments and Methods in Physics Research A* **862,** 31–35 (2017).

110. P. Gianotti. The PADME Detector. *EPJ Web of Conferences* **170,** 01007 (2018).

111. `hallcweb.jlab.org/DocDB/0008/000809/001/PhotonisCatalog.pdf`.

112. `ecrin.com/datasheets/GEFIP/618-3.pdf`.

113. `caen.it/products/v1720`.

114. `indico.cern.ch/event/731649/contributions/3237202`.

115. `keysight.com/en/pd-836437-pn-E3647A/60w-dual-output-power-supply-two-35v-8a-or-60v-05a`.

116. `keysight.com/en/pd-836433-pn-E3631A/80w-triple-output-power-supply-6v-5a-25v-1a`.

117. `uk.rs-online.com/web/p/bench-power-supplies/2287625`.

118. `uk.rs-online.com/web/p/bench-power-supplies/7531441`.

119. `caen.it/products/dt5533e`.

120. `caen.it/products/geco2020`.

121. `wwwcompass.cern.ch/compass/proposal/2021`.

122. D. Bolognini. *The MICE Electron Muon Ranger: a fundamental step towards a neutrino factory* PhD thesis (Università degli Studi dell'Insubria & CERN, 2012).

123. V. Blobel. Software alignment for tracking detectors. *Nuclear Instruments and Methods in Physics Research A* **566,** 5–13 (2006).

124. V. Blobel. Alignment algorithms. *Proceedings of the first LHC Detector Alignment Workshop,* 5–12 (2006).

125. C. Fabjan & F. Gianotti. Calorimetry for particle physics. *Reviews of Modern Physics* **75,** 1243–1246 (2003).

126. root.cern.ch/download/minuit.pdf.

127. userswww.pd.infn.it/~lunardon/didattica/docsper2/TavoleChi2.pdf.

128. G. James *et al. Modern Engineering Mathematics* (Pearson Prentice Hall, 2007).

129. mathworld.wolfram.com/DirectionCosine.html.

130. A. P. French. *Special Relativity* (Taylor & Francis, 1968).

131. indico.cern.ch/event/573666/contributions/2368853.

132. cds.cern.ch/record/618664/files/0305310.pdf.

133. indico.mitp.uni-mainz.de/event/81/contributions/2488.

Acknowledgements

It has been an amazing journey, exploring the spacetime, taking hits at nearly the speed of light, yelling and crying, begging the Nature for a whisper. Either with the technicalities or simply by making my day you helped me forge my path through this mayhem, therefore you deserve a place in my Hall of Fame: as a concrete tribute to the priceless role you had in this work, I named a little piece of it, one of the most beautiful scattering events, after you. So thank you, for my 134 parts per million are you!

È stato un viaggio meraviglioso, s'è esplorato lo spaziotempo, si son prese mazzate quasi alla velocità della luce, s'è urlato e s'è pianto, s'è supplicata la Natura per un sussurro. Che fosse dal punto di vista tecnico o semplicemente con un po' di supporto morale, voi mi avete aiutato ad aprirmi la strada attraverso questa giungla, guadagnandovi così un meritato posto nella mia Sala d'Onore: in nome dell'inestimabile contributo che avete dato a questo lavoro ne ho dedicata una piccola parte, uno degli eventi di scattering più significativi, a ciascuno di voi. Vi ringrazio, dunque, giacché le mie 134 parti per milione siete voi!

Alessia Selmi

$\theta_e = 0.01410$ rad $\theta_\mu = 0.00050$ rad $E = 4.812$ GeV

all my students and colleagues

$\theta_e = 0.01070$ rad $\theta_\mu = 0.00066$ rad $E = 7.951$ GeV

all the INSULAb stuff

$\theta_e = 0.01527$ rad $\theta_\mu = 0.00029$ rad $E = 3.472$ GeV

all the Youtube and Netflix wonders

$\theta_e = 0.01532$ rad $\theta_\mu = 0.00043$ rad $E = 4.927$ GeV

all those charged dudes that didn't make it to the end

$\theta_e = 0.01841$ rad $\theta_\mu = 0.00025$ rad $E = 3.179$ GeV

Andrea Gerosa
θ_e = 0.01817 rad θ_μ = 0.00033 rad E = 2.778 GeV
Anna Cosentino
θ_e = 0.02690 rad θ_μ = 0.00005 rad E = 1.955 GeV
Antonella Pugliese
θ_e = 0.01030 rad θ_μ = 0.00073 rad E = 7.855 GeV
Antonella Casnati
θ_e = 0.01368 rad θ_μ = 0.00063 rad E = 4.531 GeV
Antonio Principe
θ_e = 0.01954 rad θ_μ = 0.00036 rad E = 2.147 GeV
Bubih
θ_e = 0.01051 rad θ_μ = 0.00073 rad E = 6.753 GeV
Carla Livio
θ_e = 0.01490 rad θ_μ = 0.00050 rad E = 4.058 GeV
Castagna Orsetto, Palla and Sebino
θ_e = 0.01914 rad θ_μ = 0.00011 rad E = 2.905 GeV
Chiara Novati
θ_e = 0.00782 rad θ_μ = 0.00075 rad E = 13.366 GeV
Clara Matteuzzi
θ_e = 0.00149 rad θ_μ = 0.00408 rad E = 100.000 GeV
Claudia Brizzolari
θ_e = 0.01863 rad θ_μ = 0.00029 rad E = 3.115 GeV
Davide Patamia
θ_e = 0.02009 rad θ_μ = 0.00030 rad E = 2.238 GeV
Edoardo Marchi
θ_e = 0.01303 rad θ_μ = 0.00034 rad E = 6.286 GeV
Erik Vallazza
θ_e = 0.02113 rad θ_μ = 0.00019 rad E = 1.886 GeV
Fabio Anulli
θ_e = 0.02125 rad θ_μ = 0.00044 rad E = 2.021 GeV
Federico Vitali
θ_e = 0.01987 rad θ_μ = 0.00032 rad E = 2.677 GeV
Federico Ronchetti
θ_e = 0.01458 rad θ_μ = 0.00060 rad E = 3.948 GeV
Gabriele Bianchi
θ_e = 0.02483 rad θ_μ = 0.00022 rad E = 1.307 GeV

Gaia Pozzoli

θ_e = 0.01315 rad θ_μ = 0.00057 rad E = 4.525 GeV

Giancarlo Soldani

θ_e = 0.01570 rad θ_μ = 0.00036 rad E = 3.295 GeV

Gianfranco Casnati

θ_e = 0.01826 rad θ_μ = 0.00013 rad E = 1.884 GeV

Gianmarco Tolomei

θ_e = 0.01680 rad θ_μ = 0.00041 rad E = 3.320 GeV

Giovanni Ballerini

θ_e = 0.01937 rad θ_μ = 0.00022 rad E = 1.943 GeV

Giovanni Baj

θ_e = 0.00464 rad θ_μ = 0.00285 rad E = 100.000 GeV

Greta Salvetti

θ_e = 0.01458 rad θ_μ = 0.00049 rad E = 4.246 GeV

Loredana Mattalia

θ_e = 0.00891 rad θ_μ = 0.00078 rad E = 10.305 GeV

Luca Bomben

θ_e = 0.02177 rad θ_μ = 0.00013 rad E = 2.652 GeV

Luca Gennaro Foggetta

θ_e = 0.01089 rad θ_μ = 0.00038 rad E = 6.777 GeV

Maria Conti

θ_e = 0.01035 rad θ_μ = 0.00064 rad E = 6.322 GeV

Matteo Bonanomi

θ_e = 0.00950 rad θ_μ = 0.00081 rad E = 7.002 GeV

Michela Prest

θ_e = 0.02287 rad θ_μ = 0.00013 rad E = 2.115 GeV

Roberta Merlo

θ_e = 0.01292 rad θ_μ = 0.00050 rad E = 4.850 GeV

Roberto Canali

θ_e = 0.01403 rad θ_μ = 0.00038 rad E = 5.183 GeV

Roberto Bernasconi

θ_e = 0.01034 rad θ_μ = 0.00071 rad E = 6.656 GeV

Stefano Capelli

θ_e = 0.01720 rad θ_μ = 0.00041 rad E = 1.676 GeV

the almighty Fortran 77 and PAW

θ_e = 0.00897 rad θ_μ = 0.00048 rad E = 10.224 GeV

the AXIAL, ENUBET, FAMU, KLEVER and LEMMA teams

θ_e = 0.01644 rad θ_μ = 0.00030 rad E = 3.780 GeV

the songs of the Nineties

θ_e = 0.02769 rad θ_μ = 0.00025 rad E = 1.076 GeV

the stealh koala (have you found it?)

θ_e = 0.02578 rad θ_μ = 0.00057 rad E = 1.432 GeV

Valeria Tarasco

θ_e = 0.02558 rad θ_μ = 0.00030 rad E = 1.111 GeV

Valeria Belloni

θ_e = 0.01843 rad θ_μ = 0.00010 rad E = 1.123 GeV

Valerio Mascagna

θ_e = 0.01583 rad θ_μ = 0.00055 rad E = 3.133 GeV